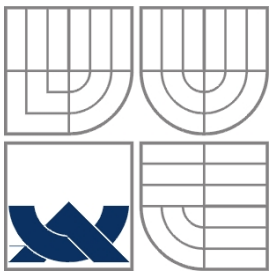

VYSOKÉ UČENÍ TECHNICKÉ V BRNĚ
BRNO UNIVERSITY OF TECHNOLOGY

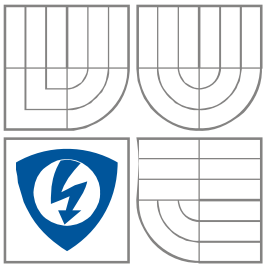

FAKULTA ELEKTROTECHNIKY A KOMUNIKAČNÍCH TECHNOLOGIÍ
ÚSTAV VÝKONOVÉ ELEKTROTECHNIKY A ELEKTRONIKY
FACULTY OF ELECTRICAL ENGINEERING AND COMMUNICATION
DEPARTMENT OF POWER ELECTRICAL AND ELECTRONIC ENGINEERING

TRACTION AXIAL – FLUX MOTOR – GENERATOR FOR HYBRID ELECTRIC BUS APPLICATION

MOTOR – GENERÁTOR S AXIÁLNÍM TOKEM PRO HYBRIDNÍ AUTOBUS

DOCTORAL THESIS
DOKTORSKÁ PRÁCE

AUTOR PRÁCE Ing. ERIK ODVÁŘKA
AUTHOR

VEDOUCÍ PRÁCE doc. Ing. ČESTMÍR ONDRŮŠEK, CSc.
SUPERVISOR

BRNO, 2010

Abstrakt

Tato dizertační práce se zabývá návrhem původního motor-generátoru s axiálním tokem a buzením permanetními magnety, zkonstruovaným specificky pro hybridní elektrický autobus. Návrhové zadání pro tento stroj přineslo požadavky, které vedly k této unikátní topologii tak, aby byl dosažen výkon, účinnost a rozměry stroje.

Tato partikulární topologie motor-generátoru s axiálním tokem je výsledkem literární rešerše, kterou následoval výběr koncepce stroje s představeným návrhem jako výsledkem těchto procesů.

Přístup k návrhu stroje s axiálním tokem sledoval „multi-fyzikální“ koncepci, která pracuje s návrhem elektromagnetickým, tepelným, mechanickým, včetně návrhu řízení, v jedné iteraci. Tím je v konečném návrhu zajištěna rovnováha mezi těmito inženýrskými disciplínami. Pro samotný návrh stroje byla vyvinuta sada výpočtových a analytických nástrojů, které byly podloženy metodou konečných prvků tak, aby samotný návrh stroje byl přesnější a spolehlivější.

Modelování somtného elektrického stroje a celého pohonu poskytlo představu o výkonnosti a účinnosti celého subsytému v rozmanitých operačních podmínkách. Rovněž poukázal na optimizační potenciál pro návrh řízení subsystému ve smyslu maximalizace účinnosti celého pohonu.

Bylo postaveno několik prototypů tohoto stroje, které prošly intensivním testováním jak na úrovni sybsytému, tak systému. Samotné výsledky testů jsou diskutovány a porovnány s analytickými výpočty parametrů stroje.

Poznatky získané z prvního prototypu stroje pak sloužily k představení možností, jak zjednodušit výrobu a montáž stroje v příští generaci.

Tato práce zaznamenává jednotlivé kroky během všech fází vývoje elektrického stroje s axiálním tokem, počínaje výběrem konceptu stroje, konče sumarizací zkušeností získaných z první generace prototypu tohoto stroje.

Klíčová slova: Hybridní elektrický pohon, Původní návrh motor-generátoru s axiálním tokem a buzením permanentními magnety, elektromagnetický návrh, tepelný návrh, návrh řízení, účinnost, měření

Abstract

This thesis deals with a design of a novel Axial-Flux Permanent Magnet Motor-Generator for a hybrid electric bus application. Thus, the design specification represents a set of requirements, which leads toward a concept of a unique topology meeting performance, efficiency and dimensional targets.

The particular topology of the Axial Flux Permanent Magnet Motor-Generator discussed in this work is an outcome of deep literature survey, followed by the concept selection stage with the layout of the machine as an outcome of these processes.

The design approach behind this so-called Spoke Axial Flux Machine follows an idea of "multiphysics" iterations, including electromagnetic, thermal, mechanical, and controls design. Such a process behind the eventually proposed design ensured a right balance in between all of these engineering disciplines. A set of bespoke design and analysis tools was developed for that reason, and was backed up by extensive use of Finite-Element Analysis and Computational Fluid Dynamics. Therefore, the actual machine design gained higher level of confidence and fidelity.

Modelling of the machine and its drive provided understanding of performance and efficiency of the whole subsystem at various operational conditions. Moreover, it has illustrated an optimization potential for the controls design, so that efficiency of the machine and power electronics might be maximized.

Several prototypes of this machine have been built and passed though extensive testing both on the subsystem and system level. Actual test results are discussed, and compared to analytical predictions in terms of the machine's parameters.

As a lesson learned from the first prototype of this machine, a set of redesign proposals aiming for simplification of manufacturing and assembly processes, are introduced.

This work records steps behind all phases of development of the Axial Flux Machine from a basic idea as an outcome of concept selection stage, up to testing and wrap-up of experience gained from the first generation of the machine.

Keywords: Hybrid Electric Drive, Novel Axial-Flux Permanent Magnet Generator, Electromagnetic Design, Thermal Design, Controls Design, Efficiency, Testing

Bibliografická citace

ODVÁŘKA, E. Motor-generátor s axiálním tokem pro hybridní autobus. Brno: Vysoké učení technické v Brně, Fakulta elektrotechniky a komunikačních technologií, 2010. 123 s. Vedoucí dizertační práce doc. Ing. Čestmír Ondrůšek, CSc.

Prohlášení autora o původnosti práce

Prohlašuji, že dizertační práci na téma *Traction Axial-Flux Motor-Generator for Hybrid Electric Bus Application* jsem vypracoval samostatně pod vedením školitele a s využitím odborné literatury a dalších informačních zdrojů, které jsou všechny citovány v práci a uvedeny v seznamu literatury.

Jako autor uvedené dizertační práce dále prohlašuji, že v souvislosti s vytvořením této dizertační práce jsem neporušil autorská práva třetích osob, zejména jsem nezasáhl nedovoleným způsobem do cizích autorských práv osobnostních a jsem si plně vědom následků porušení ustanovení § 11 a následujících autorského zákona č. 121/2000 Sb., včetně možných trestněprávních důsledků vyplývajících z ustanovení § 152 trestního zákona č. 140/1961 Sb.

V Brně dne 15. 8. 2010 Podpis autora.....

Acknowledgement

The research work on this motor-generator is a part of the major industrial technology initiative focusing on hybridization of powertrains, specifically for commercial vehicles. The proposal of this thesis thus combined a strong driving force of industry aiming to turn a research project into a product, with intellectual background of a university.

First of all, I am very grateful to Doc. Ing. Čestmír Ondrůšek, CSc. for admitting me to the PhD study programme. I have received from him much valuable advice throughout not only the postgraduate period, but entire studies at the Department of Power Electrical and Electronics Engineering of Brno University of Technology. I am thankful for number of fruitful discussions we held throughout this period, related not only to the electrical engineering, but also to miscellaneous topics important to the society as a whole.

It would be possible neither to initiate, nor to complete this project without my assignment with Cummins Generator Technologies Stamford, UK, where I was given the opportunity to join the Research & Technology team under leadership of Dr. Neil L. Brown. I am extremely glad for the level of encouragement and support I was given during the two-year period I spent there in excellent electromagnetic design group led by Dr. Salem Mebarki.

After completing the research project dealing with this particular motor-generator, I was offered an other unique opportunity in terms of working on the system level of the hybrid powertrain at Cummins Inc., Columbus, Indiana. I would like to thank Dr. Nazar Al-Khayat, the director of Hybrid Engineering in Cummins Inc., for his strong leadership and support. He in fact enabled me to accomplish my PhD study programme.

I was always able to count on an incredible level of encouragement and support from my parents Dagmar and Radomír Odvářkovi, and my sister Martina. Thus, I would like to dedicate this thesis to my family.

Erik Odvářka

Columbus, Indiana, USA

August 2010

Contents

1. Introduction

Hybrid Electric Vehicle (HEV) is one of the more frequently used words of late. What is the driving force behind such a major change of vehicles' powertrain architecture including not only small cars but line-haul trucks as well?

1.1. Why Hybrid Electric Vehicles?

The human race is probably faced with one of its biggest challenges ever. Available resources of fossil fuels are narrowing down, and are frequently located in countries with non-cooperative government. Moreover, massive import of raw materials participates in the negative surplus of trade balance in many well-developed countries, and amplifies economical unbalance with negative impact to the world economy. The other frequent topic is reduction of emissions, such as solid particles, NOx and SOx in conjunction with carbon-dioxide footprint as one of the main sources of global warming activity. Transportation in general seems to have excessive requirements by means of consumption of available resources and in the same time, negative effect on the environment by means of pollution.

According to figures shown in [1], transportation accounts for 51% of CO_2 emissions per average American household. The following Fig. 1-1 illustrates on an example of a passenger car, how the CO_2 annual footprint might be reduced by lower fuel consumption (MPG stands for Miles-per-US Gallon), considering average mileage of 15 000 US miles per year with 55% of city driving and 45% of highway driving [1].

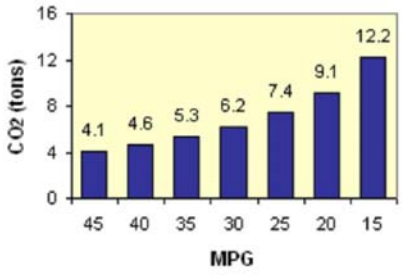

Fig. 1-1 Dependency of CO2 emissions on fuel consumption [1] according to data from April 2008

Some remarkable achievements presents Clean Cities initiative, when operation of 82000 HEV's fleet, including Pick-Up & Delivery trucks, buses and refuse disposal trucks, in 87 American metropolitan areas saved in 2007 only, a stunning 16 millions US gallons of fuel [2]. One may relate these savings to the environmental impact.

There are various possible ways of hybridizing a vehicle and making it more fuel efficient and environmentally-friendly in the same time by:

- Reducing idle/low output operation of Internal Combustion Engine (ICE)
- Electrification of engine's accessory load
- Recapturing waste energy (and using it)

- Reducing the size and power of ICE

Reduction of ICE idling operation is called a mild hybridization, with the engine frequently having the alternator and the starter motor replaced by Integrated Starter-Generator (ISG).

An ICE and vehicle requires several accessory drives for its operation. An engine designed for a bus application typically involves gear or belt driven hydraulic pump, air compressor, Freon compressor, water pump and cooling fan. Accessory drives in a bus application may require up to 70kW in peak power demand. However, these accessory drives are coupled with specific gear ratios to the engine's crankshaft, disabling effective control of these devices in terms of power consumption. Electrification of accessory drives in general may lead to significant fuel consumption improvements [3].

Further room for improvement gives recapturing of waste energy, either mechanical energy through regenerative braking or thermal energy using the Waste-Heat Recovery (WHR) concept. Thermal energy from Exhaust Gas Recirculation (EGR) and main exhaust gas stream are recaptured in a boiler and superheated in order to propel high-speed gas turbine-generator providing eventually extra electrical energy [4] to the electrical machines involved in HEV powertrains. These technologies, of regenerative braking and WHR might be found in various HEV topologies including parallel, combined or series. Options for waste energy recovery in conjunction with energy storage system and electrical machines available to deliver an extra traction power, allows to downsize ICE of HEVs, which is sized to rather average power demand instead of peak power demand of a vehicle.

The work applies to the design of a novel axial-flux permanent-magnet traction motor generator (MG2) dedicated for HEV application. The following pages describe the design of MG2 considering concept selection process and design stages, including electromagnetic in conjunction with thermal and control strategy design, considering mechanical constraints, manufacturing and testing. MG2 design must meet high requirements by means of efficiency, power density, and ability to work under changing operational conditions in terms of variable voltage supply level, coolant parameters or ambient temperature. Critical is at the same time cost, durability and ease of maintenance.

1.2. Electrical Machines and Drives in Hybrid Electric Vehicles

Electrical machines for hybrid electric vehicles have to fulfill specific design criteria related to their application. Many of these are contradicting each other and it is up to the teams of designers, manufacturing engineers or experts in finance, marketing and product planning to resolve these issues and to come up with the best compromise fully satisfying customer's needs.

Hybrid electric vehicles aim for reduction of fuel consumption which is suggesting the need for increase of system efficiency or reduction of losses both on system and component levels. This requires on a level of electric drive not only deep understanding of their sources separately in the electrical machine and power electronics, but also an interaction between machine, power electronic and its control plays an important role. As a good example, reduction of converter switching frequency may help to decrease switching losses in power electronics components on one side, but

increase stray losses in the electrical machine on the other side and vice versa [5]. Alongside with this, loss minimization process requires employing of more advanced materials and components in the design of electrical drive.

Power electronics components in current/voltage ratings applicable for HEV drives are most likely to be silicon-based diodes and IGBT transistors. The current development trends are focused on increase of the maximum junction temperature (typically from 125degC up to 150degC) in order to make cooling easier [6] and to eliminate reliability issues. IGBTs frequently suffer namely from intermittent operation causing wire bond lift due to solder fatigue. Unlike silicon-based IGBTs with development focused more-less on packaging and reliability issues [7], prospective silicon-carbide (SiC) technology [8] aims to significantly reduce losses, to increase operating temperature (theoretically up to 500degC) and further benefit out of more robust mechanical properties [9]. Closest by means of the level of development to mass production are SiC diodes with switching behavior similar to Schottky diodes but voltage ratings up to 2.5kV of reverse breakdown voltage. Mass introduction of SiC components, either diodes or even switches in a later stage will open up possibilities for significant increase of power electronics efficiency and power density as well.

Electrical machines involve an evolutionary process of massive implementation of Permanent Magnets as a source of excitation [10] or adopting more advanced materials for design of actual magnetic circuit. This involves electrical steels with higher level of magnetic saturation [11] and at the same time, aiming for reduction of specific iron loss, especially at higher remagnetizing frequencies [12]. Some of the more exotic material, such as CoFe or soft magnetic alloys still struggle to compete with conventional electrical steel for cost reasons. However, the design process still has to come up with optimal compromise between the level of saturation of the magnetic circuit, iron losses and total mass of the machine. Iron losses are an important player in the system efficiency due to the drive cycle applied to electrical machines in HEV application, which may be characterized as intermittent. This involves operation in both motoring/braking mode and idling as well, when only the engine propels the vehicle and spinning electric machine has got only negative impact on fuel consumption due to the iron losses [13].

Application of advanced permanent magnet materials, typically NdFeB, allows to reach magnetic loading in the airgap even up to 1T [14] without generation of extra copper losses due to the excitation and therefore, difficulties with heat dissipation from the rotor side. This helps, in conjunction with improved liquid cooling system, to further increase torque density of the most recent designs for automotive application up to 4.4 Nm/kg [15] in continuous operation. The most recent research in the field of magnet materials promises to achieve up to 1.519 T of remanent flux density for NdFeB material [16].

Significant improvement is visible in the field of insulation systems as well. Recent designs of traction machines allows operation either in H or C insulation class [17], what leads to an option of higher electrical and thermal loading of the machine and related further rise of torque density.

Selection process of cooling method for electrical machines in HEV follows demands for compact design and therefore, adopts liquid cooling due to maximization of typical current densities in the stator winding [18]. The fluid typically circulates in a cooling jacket shrunk fitted onto a stator core, enabling to minimize thermal resistance

of the heat conduction path from stator winding toward the cooling jacket. Cooling of electrical machines in HEV is frequently incorporated either to a cooling circuit of the ICE or uses pressurized oil from transmission, typically Automatic Transmission Fluid (ATF), in the case of electrical machines being integrated into this component [19]. However, one may point out the main disadvantage of integrated cooling of machines with ICE, which works at relatively high operating point of the engine's coolant limiting thermal gradient from the winding to the coolant. Design of the electrical machine must then consider the worst case scenario in terms of the coolant reaching temperature up to 105deg C, which is the temperature limit for ICE operation. However, the entire vehicle as a system benefits out of lower component count by means of sharing radiator, water pump and piping by ICE and electrical machine, and wider options for thermal management on a system level.

The frequently mentioned need for compact design of electrical machines in HEV application comes mainly from limitations due to the layout of vehicles and available space in the vehicle's chassis. Design constraints by means of dimensions varies based upon specific configuration of HEV, but generally speaking, parallel hybrids require electrical machine with short axial length due to the sandwiched nature of powertrain. An elegant solution is installation of axial-flux machines into engine's bellhousing with replacement of a flywheel by rotor plates so that total inertia of the engine matches the required value [20]. Radial machines suffer in a case of limited axial length due to inconvenient proportion between length of endwindings and active length of the magnetic circuit. This drawback might be partially suppressed by adopting radial machines with concentrated fractional windings [13]. The constraint of outer diameter appears to be important in second frequent option for integration of electrical machines in HEVs, particularly into transmission [21]. This suggests a solution having epicyclic gears of the transmission nested into the rotor of the electrical machine, thus providing compact subsystem packaging. Regardless the way of integration of electrical machines into the vehicle's powertrain, compact design with maximized power density and reduced mass minimizes necessary changes of vehicle's overall design.

Although DC machines were adopted in early stages in HEV drives, they do not take a place in recent solutions because of well known commutation issues. Brushless-DC version was applied in initial attempts of HEV development in limited scale only [22]. Induction machines are involved in a number of electric drives in HEVs [19, 23] taking advantage in matured technology, established production and robust construction. However, induction machines tend to loose in competition with Permanent-Magnet machines in terms of power density because of lower level of magnetic loading in the airgap and less convenient distribution of heat loss sources in the machine. A significant proportion of heat loss is allocated on the rotor side and considering totally enclosed design typical for electrical machines in HEV, relatively low heat transfer coefficient from the stator through an airgap to the stator appears to be a limiting factor. Moreover, permanent-magnet based excitation principally does not generate any power loss by itself except possible eddy current losses in magnet material, unlike wound-field synchronous machines or induction machines requiring excitation current in the field winding or rotor bars respectively. Efficiency of permanent magnet machines may suffer in terms of iron losses due to permanent excitation However, permanent magnet machines as traction motors operate close to the maximum speed in field weakening mode, effectively reducing level of iron losses. Therefore, Permanent-Magnet machines should be the leader among the considered group of electrical machines topologies in terms of efficiency as well [24].

Traction motors by their nature operate above specific base speed in the constant output power region. This requires ability of field weakening, which is not straightforward for permanent-magnet machines in terms of controlling excitation field. Such machines allow indirect field weakening due to armature reaction field imposed to the magnetic circuit of the machine through negative d-axis current, considering Park's transformation and currents recalculated in the dq0 reference frame. However, d-axis current does not contribute to the torque production unless the machine behaves as an inverse-salient with inductance in q-axis being higher than the one in d-axis [18]. This fact limits possible application of Surface–Mounted Permanent Magnet synchronous machines because of the equality of inductances both in d- and q- axis. Therefore, traction drives based on Synchronous-Permanent Magnet machines frequently employ topologies with Inset or Embedded Permanent Magnets fulfilling criterion of inverse-saliency. Variant with Embedded-Permanent Magnets provides a number of versions, in particular with magnets split into "V" pattern or inserted into multiple layers of magnets to the rotor, ultimately tailoring the saliency ratio. The machine eventually meets requirements by means of width of region with constant output power versus the region characterized rather by constant torque operation. Radial Embedded-Permanent Magnet, machines, particularly with the "V" shape pattern might be considered as a benchmarking technology in terms of HEV application according to comparative studies carried under governance of the US Department of Energy [25].

Other members of the synchronous machines family are Switched Reluctance Motors (SRM), well known for their simple and robust construction. However, these machines have certain drawbacks, generally speaking high torque ripple, level of acoustic noise or higher number of power electronics components and their switching frequency than in three-phase inverters, in particular for 8/6 pole configuration or higher, topologies [26]. More prospective for HEV application seems to be derivatives, including Hybrid Switched Reluctance Motors [27], combining Permanent Magnet and electromagnetic excitation aiming mainly for suppression of mentioned drawbacks. However, SRMs are still being applied in low-cost drives, such as in domestic appliances [28].

Although Axial-Flux machines are currently mostly produced for special applications, such as Variable-Speed Integrated Genset (VSIG) [29] providing fuel savings due to the matching of the generator set speed to the operational point of ICE maximizing system efficiency, this topology may find its place in HEV powertrain constrained in terms of axial length. There are numerous possible designs of axial flux machines [30], but comparative studies have shown that toroidally-wound Axial Flux machines – TORUS [31], either slotted or non-slotted provide maximal torque density. However, non-slotted version seems to be less feasible for inverter-fed drives due to naturally lower inductances in comparison to the slotted counterpart. This might be a disadvantage in field weakening operation, when the machine benefits from large voltage drop due to the X_d reactance. Moreover, electrical drive may benefit out of higher inductances due to lessen demand for power electronic switching frequency because of current ripple issue. In terms of thermal design, TORUS machine allows sandwich construction of the stator core with a cooling jacket located in between half segments of stator lamination. There is an option for single rotor configuration with shine-through magnet polarization direction [32], but this would require installation of two cooling jackets because of the stator cores being kept apart. Moreover, winding configuration would be narrowed down into sunflower topology.

Design of Axial-Flux permanent-magnet machines in terms of field weakening capability frequently employ a technique of combining permanent magnets and iron poles mounted on the rotor plate. Either by having a bottom part of magnet replaced by iron pole [33] or having a permanent magnet located in between iron poles. Because of one magnetic pole of the machine is composed out of iron pole and permanent magnet material, the design must avoid existence of significant leakage flux. A different layout proposes two rows of alternating magnets and iron poles with angular misalignment in between rows by 180deg electrical [34]. However, these topologies are characterized as salient, with $L_d>L_q$, because the iron poles are placed in d-axis, which effectively reduces reactance for d-axis armature reaction fluxpath. Although these topologies allow field weakening, the torque production in this operational mode is further reduced because of production of negative reluctance torque.

In order to mimic inverse-salient machines, permanent magnets must be placed into the rotor structure analogically to the embedded, inset or spoke radial flux machines [35], so that $L_q>L_d$. Although literature sources principally suggests these solutions [30, 36], there is no complete design proposal, which would be conducted at least into the prototype stage. The main issue is how to insert magnets into the rotor structure, which must be sufficiently mechanically rigid in order to sustain both centrifugal and unbalanced axial forces due to the machine's operation.

However, there is an option of combining permanent-magnet and wound-field excitation in so-called Hybrid Excitation Synchronous Machines. This may lead toward better utilization of excitation by means of avoiding indirect field weakening. Homopolar and Bipolar Excitation Machines hardly meet the peak efficiency of 90%, which is not competitive in comparison with only Permanent-Magnet excited machines [37]. Other available solutions are consequent pole Permanent Magnet hybrid excitation machine with alternating iron poles and magnets on the rotor and a DC excitation coil in the middle of stator or any version of the hybrid-excitation claw pole machine based on automotive alternator. Hybrid Excited machines are available in Axial-Flux layout as well [38]. The main drawbacks of Hybrid Excitation Machines are more complicated electromagnetic design, manufacturability, higher component count and additional controlled variables in terms of control design.

Overall performance of an electrical machine in terms of efficiency varies with applied control strategy. Permanent Magnet Synchronous Machines adopt frequently $I_d=0$, Maximum Torque-per-Ampere (MTPA), Maximum Efficiency or the less likely Unity Power Factor control strategies [39, 40, 41, 42]. The $I_d=0$ control strategy considers magnet torque only. Hence, it is most feasible for surface-mounted PM machines. In case of inverse-salient machines, MTPA benefits from employing reluctance torque combined with magnet torque. As the abbreviation MTPA suggests, this control strategy minimizes copper loss at the same time. Maximum efficiency control strategy aims for total loss reduction, in particular iron and copper loss using loss minimization conditions [43]. MTPA is in a way a simplified Maximum efficiency control strategy with loss minimization condition assigned for zero speed, and therefore, ignoring the iron loss component. Theoretically, maximum efficiency strategy should be the optimal choice because it maximizes overall efficiency of the electric drive once power electronics losses are included.

However, the previously mentioned control strategies are not applicable in the entire torque-speed operational zone of the drive. The Back-EMF in conjunction with a voltage drop on reactances would make the machine from certain speed uncontrollable

and the machine must enter the field weakening operational mode since then [35]. Therefore, we might divide the operation of inverse-salient machines into a torque regime, when MTPA or maximum efficiency control strategies are applicable and into the voltage-constrained operation, when transition into the field-weakening mode is necessary.

As the transition into field weakening occurs once input voltage is insufficient, there is no clear distinction for switching in between control modes for a system with floating DC bus voltage. Unlike in [13] with a DC/DC converter boosting and stabilizing the DC bus voltage, the adopted configuration of the electric drive assumes the inverter is directly fed from the battery pack. The terminal voltage of battery pack swings with the load current and depends on the state of charge as well. Therefore, it does not seem to be effective to switch into field weakening at a fixed boundary in terms of Torque-vs-Speed load points, but rather track availability of MTPA or Maximum Efficiency Control Strategy based upon the instantaneous DC bus voltage [44].

The electrical drive as a subsystem of HEV could be handled as a “black box” which is in a motoring operation asking for certain input electrical power in terms of the battery current and DC bus voltage. The output parameters are a shaft speed and a torque alongside with power loss, which needs to be dissipated. The set of parameters describing the “black box” completes the inlet and outlet coolant temperature and its flow rate. A convenient way of representing the electrical drive in HEV simulation is through an efficiency map [45]. However, the efficiency map might be generated only under certain assumptions such as given DC bus voltage, fixed winding resistance or chosen control strategy for the drive and is unable to capture variations of operational conditions and drive’s variables. Efficiency maps still play an important role at least in assessment of the power split in between electrical machine and ICE in order to make sure, that these devices work at optimal operational point. A different modelling approach is based on analytical models instead of efficiency maps [46]. Analytical models allow real time simulation of an electrical drive, which might even be coupled with the overall simulation of HEV. Hence, the main limitation of efficiency maps in terms of fixed operational conditions is overcome. Accuracy of electric drive modelling in terms of efficiency relies on determination of equivalent circuit parameters in dq0 reference frame, including iron loss representation. True assessment of copper and iron losses alongside with mechanical, windage and additional losses such as in the cooling jacket is a necessity for accurate calculation of efficiency at any operational point.

1.3. Traction Motor Generator MG2

A part of the combined hybrid powertrain is the motor-generator MG2. Combined powertrain, as depicted on Fig. 1-2, involves Internal Combustion Engine (ICE) as a dominant source of power with Motor-Generator 1 (MG1) directly coupled to the crankshaft. MG1 fulfils mainly a role of generator keeping state of charge of the battery pack within pre-defined operational range. Besides the generating mode, MG1 is replacement of the starter mode and allows operation of the engine in start-stop mode. This allows further reduction of fuel consumption by up to 10% through eliminating the idling operation of the ICE. Moreover, MG1 may get engaged in active torque cancellation too.

One may distinguish several different operational modes for MG2 in the hybrid powertrain. MG2 is the only source of power in fully electric mode, when the clutch in between MG1 and MG2 is disengaged and only MG2 drives the vehicle draining energy out of the battery pack. Fully electric mode of the vehicle seems to be convenient in conditions characterized by drivecycles with intermittent operation, such as in urban areas. Then the ICE may be completely turned-off, unless the vehicle exceeds defined speed and MG2 is unable to maintain desired driveability of the vehicle.

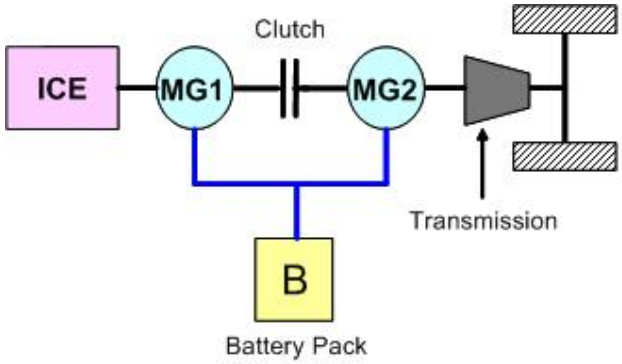

Fig. 1-2 Layout of the combined hybrid powertrain.

MG2 provides traction power once the clutch is engaged as well. MG2 is capable of fulfilling torque-boost mode, increasing level of available torque at low-speed operation of the powertrain. Moving into speed range close to the base speed, MG2 enters torque assist mode, primarily helping with reduction of ICE's emissions.

Instead of wasting kinetic energy of the vehicle by friction brakes or retarder, MG2 is available for recapturing such energy during regenerative braking, when recovered energy is stored in the battery pack. A scatter plot presented in Fig. 1-3 gives indication of operational points of MG2 under Manhattan drivecycle.

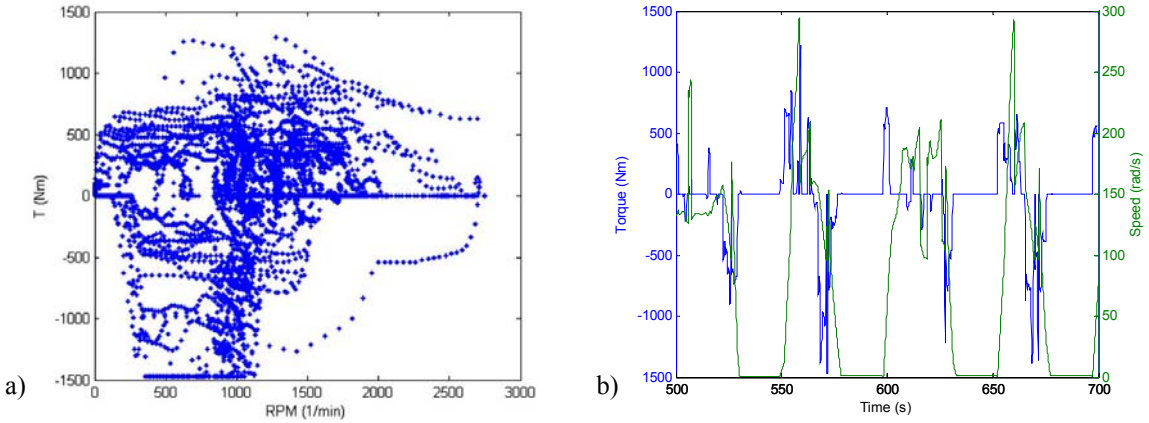

Fig. 1-3 a) Scatter plot of MG2 operational under Manhattan drive cycle b) profile torque vs time and speed vs time as a segment of the same drivecycle.

Manhattan drive cycle represents operation of the hybrid vehicle in urban area. Based upon a particular application of the vehicle, the drivecycle may vary accordingly with an impact on definition of the power node of MG2.

2. MG2 design specification

MG2 as an electrical drive is designed for two-quadrant operation for positive sense of rotational direction following the engine, and both positive and negative polarities of developed torque. However, electrical drive in hybrid electric vehicle follows specific design requirements, given by nature of power source for the drive, operational conditions or adopted cooling architecture.

2.1. Definition of the power node

The torque mode of operation is defined from zero up to base speed of 1300 rpm, where MG2 must develop 734.6 Nm of continuous torque and twice as high maximum torque. The operational zone from base up to maximum speed of 2800rpm is characterized by constant output power. That means, MG2 operates in field weakening mode at rated power of 100kW and twice as much of overload power. Any speed over 2800 rpm is considered as overspeed, when MG2 is not required to develop any power, but only to ensure safe field weakening, so that MG2 will not become uncontrollable.

MG2 is three-phase, inverter-fed machine. The inverter's DC bus is directly connected to the battery pack terminals, and therefore, is not considered as a stiff voltage source. Battery voltage may swing from 500VDC at minimum state-of-charge (SOC) up to 800VDC at full SOC. To ensure safe operation in field weakening, MG2 design considers the DC bus voltage level corresponding to minimum SOC as a design requirement. These design considerations are summarized in Tab. 2-1.

Tab. 2-1. Design requirements for MG2**.**

Nominal power Pn @n_b (kW)	100
Peak power Pmax @n_b (kW)	200
Power density (kW/dm^3)	10
Nominal Speed n_b (rpm)	1300
Maximum Speed n_{max} (rpm)	2800
Over-Speed limit (rpm)	3200
Outer diameter restriction	To fit into SAE0 housing
Maximum axial length (mm)	200
Nominal Voltage V_{nom} (V_{rms})	204
Back-EMF @nb (V_{rms})	141
Maximum Current I_{max} (A_{rms})	240
Winding configuration:	Toroidal, full pitch
Nominal winding temperature (degC)	160
Coolant composition	50% glycol, 50% water
Coolant inlet temperature T_{in} (degC)	105
Nominal Coolant Flow Rate q (dm^3/min)	15

The selected semiconductors on the inverter side limit the maximum Back-EMF by the maximum reverse voltage of IGBT transistors and diodes. From failure mode stand point of view, lose of control over IGBT firing may lead to uncontrollable generation mode. Therefore, the peak line-to-line EMF can not exceed the reverse blocking voltage of power electronics component even at the maximum overspeed. Transistors' rating limits the maximum current as well, in this case to 480 Arms of phase current.

MG2 is water-cooled machine in order to maximize heat rejection capability of the machine. The stator assumes sandwich design with two symmetrical stator corepacks clamped by an aluminium cooling jacket in the middle. A coolant flows circumferentially though a groove in the middle of the jacket. The entire stator core is wound by full-pitch toroidal winding ensuring that the heat rejection path from a coil to the cooling jacket has got effectively low thermal resistance. Following Fig. 2-1 shows two segments of a cooling jacket with a duct created by locking and sealing these segments together.

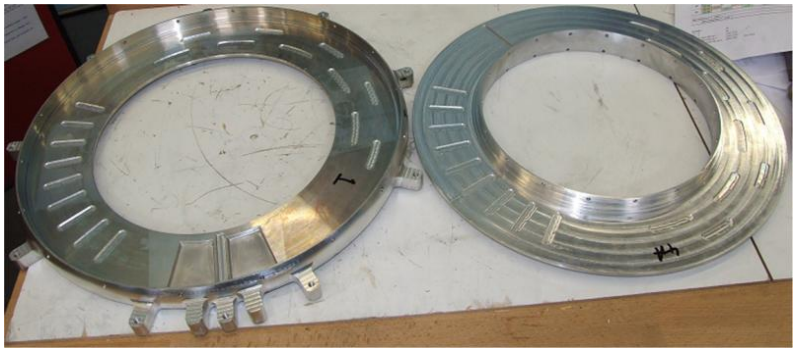

Fig. 2-1 Segments of the cooling jacket eventually creating the duct in the middle after assembly

The cooling layout of the hybrid vehicle assumes common cooling loop for the engine and electrical machines. The nominal coolant temperature for a diesel engine usually oscillates close to 90degC. However, the coolant temperature may rise up to 105degC, which is a limiting temperature activating the protection valve in the cooling loop. The coolant composition is combination of 50% water and the same proportion of glycol. In terms of the flow rate limit, the cooling jacket is mechanically designed up to the flow rate of 15 l/min.

2.2. Design restrictions due to layout of vehicle's powertrain

The hybrid powertrain is in this particular case engine-oriented. The driving idea behind it is to bring a competitive advantage of a compact and modular package containing electrical machines, which would be directly mounted on the engine's housing and crankshaft. An OEM customer would have then an option of choosing a hybridized engine as a replacement of a standard ICE with keeping transmission and the rest of the power train towards wheels in its place within the vehicle.

Fig. 2-2 shows simplified cross-sectional view of the powertrain in testing configuration, when automatic or automated manual transmission are replaced by a driveshaft and, a dynamometer representing a load of the vehicle.

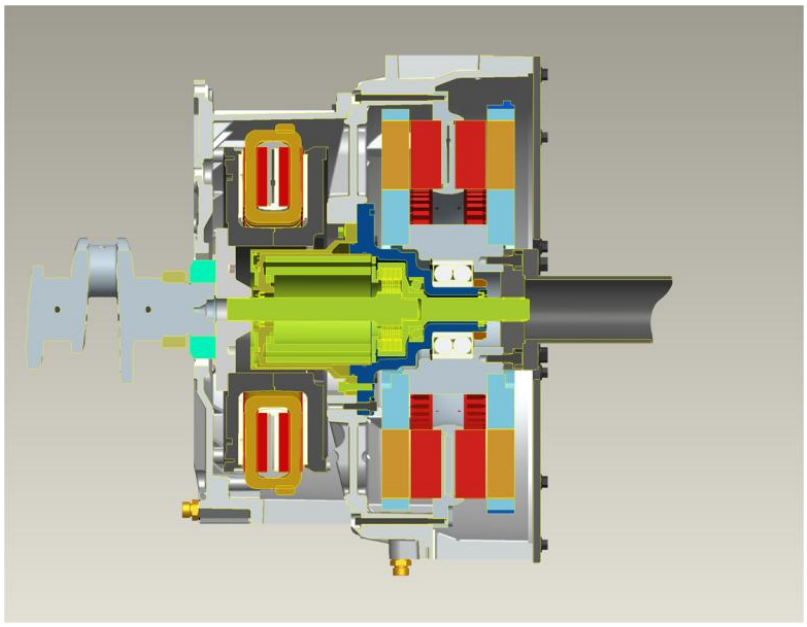

Fig. 2-2 Cross-sectional view of combined hybrid powertrain – setup for the test cell installation. MG1 occupies the left hand side, whereas MG2 the right hand side housing

MG1 is directly mounted to the crankpalm and due to its inertia, replaces the engine's flywheel. MG1's housing is designed according to SAE 1 standard dimensions, and is directly fitted onto engine's bellhousing of the same size. Stator of MG2 is mounted by lugs of the water jacket into midhousing, which is cascaded on the MG1's housing. The mid housing creates in the same time an interface for MG2 and the spline shaft, which transmits torque from the engine, once clutch is engaged. The selected wet clutch is of radial arrangement, when the actual clutch assembly decomposes of several cascaded radial clutches. The clutch is electromagnetically actuated, which allows effective control over operational modes of the vehicle in terms of switching in between pure electric or parallel arrangement.

The spline shaft rotates in the supporting back plate due to single row ball bearing. However, bearing holding the rotor subassembly of MG2 needs to cope with unbalanced axial forces and tilting forces due to possible misalignments of the machine, making the set of airgaps non-uniform. Therefore, the selected bearing is of double row angular contact arrangement, which is able to cope with axial forces, if appropriately selected. The implication of unbalanced axial forces and tilting on bearing selection process will be discussed further.

The rotor hub of MG2 is directly mounted to the driveshaft in the test bed arrangement, or to the input shaft of the transmission in a case of a vehicle.

2.3. Scope of the thesis

The main goal of this thesis is to come up with a consistent "multiphysics" approach in terms of integrated electromagnetic, thermal and control design within constraints given by the mechanical analysis. An important part is also modelling of the drive so that the model might be directly incorporated into overall simulation of a HEV. Testing of MG2 is going to validate design of the machine, including its mathematical

models. Main subjects to be discussed and resolved in the thesis may be divided into several thematic sections.

2.3.1. Electromagnetic design of Spoke Axial Flux Machine

Design of presented machine topology is more complicated due to presence of inherently saturated parts. Feasible design tool seems to be method of equivalent reluctance circuit. Bridges are then represented by reluctance parallel to the magnet. Since reluctance as a lumped parameter in a circuit depends on relative permeability of iron, the exact values should be obtained using Finite-Element Analysis (FEA). Sizing of the machine requires good choice of aspect ratio between inner and outer diameter of the corepack and finding the nominal torque density according to the cooling capability. Level of magnetic loading, especially on the stator side, must be selected so that both teeth (especially at the ID when their thickness is lowest) and stator backiron does not get saturated even at maximum loading. The first design iteration should include sizing of permanent magnets in terms of their axial and tangential length so that the magnet mass is minimized for the required level of magnetic flux density in the airgap. The airgap size is determined to be at least 2mm for safe operation of the machine, considering manufacturing tolerances, and tilting or axial shifting of rotor plates. Inductances in a view of normalized flux linkage must be tuned so that the machine is able to field weaken whenever it is required, and voltage drops at reactances are not excessive which would limit controllability at operational speed below the base speed. Therefore, the basic control design needs to be an integral part of electromagnetic design spreadsheet. The following validation focuses on steady state temperature rise at any operational point, where the continuous operation is required. The same is necessary for overload condition once duty cycle and on-time/off time are defined.

2.3.2. Verification of the electromagnetic design by FEA

Analytical computational methods might be losing accuracy after applying to a machine with non-linear magnetic circuit. Therefore, FEA is a convenient tool for verification of machine's performance and determination of equivalent circuit parameters in dq0 reference frame. Moreover, FEA helps in verification of sizing the parts sensitive to saturation. Apart from the bridges holding the magnets, there are several other leakage flux paths. The first turn of laminations at the inner carrier ring must remain unslotted for manufacturing reasons, which introduces 0.5mm thick extra leakage flux path. There is potentially little stray flux at back side of a rotor plate and through the outer carrier ring. No-load transient nonlinear analysis may be applied to obtain EMF and cogging torque. The following analysis focuses on verification of torque production using transient nonlinear FEA. The torque production analysis includes split of the total torque into magnet and reluctance torque as well. In terms of estimation of inductances, effectively only applicable setup is with magnets kept active in order to keep bridges saturated. Methods applicable for machines with quasi-linear magnetic circuit, such as calculation due to armature reaction flux only, would fail especially in calculation of d-axis inductance. Moreover, results of FEA provide feedback to analytical calculations and are convenient for increase of their accuracy.

2.3.3. Identification and estimation of losses in the machine

The main sources of losses are copper, iron, stray and mechanical. As the estimation of copper losses is straightforward, modelling methods for iron losses, in

particular the hysteresis component, are mainly empirical. A good example would be Steinmetz equation. As the machine operates in a variable-speed drive with maximum remagnetizing frequency of stator steel above 400Hz, it is necessary to map up profile of iron losses over entire Torque-vs-Speed map. Extra iron losses might be induced because of the airgap flux density waveform contains higher harmonics. Therefore, an option might be to map up time-variant flux density waveforms for each particular part of stator iron and calculate total iron losses using results of Epstein test at variable remagnetizing frequencies. This method may include impact of higher harmonics of flux density in iron as well. Rotor iron losses should be principally low due to its laminated structure. However, extra losses may appear due to distortion of airgap flux density by stator slotting. Additional losses include mainly eddy current losses in the aluminium cooling jacket dependent on armature current. Eddy current losses may appear in permanent magnets, stainless steel pins holding the stator corepack in the cooling jacket or in both inner and outer carrier rings. However, the overall impact on efficiency is not expected to be significant. The armature current has a certain level of harmonic distortion because of Pulse-Width Modulation, causing additional losses in the stator iron. Mechanical losses depend mainly on bearing selection. Presumably, windage and friction will not play an important role because of totally enclosed character of the machine and smooth surface of rotor plates.

2.3.4. Unbalanced axial forces due to tilting or axial shift of rotor plates

In terms of integration into the vehicle, the designed traction motor is located in between a clutch and a transmission. The stator is mounted to the interface housing holding the angular contact double-ball bearing, which carries the rotor plates, as well. There are a couple of options causing difference in between airgaps on both sides of stator and therefore, unbalanced axial forces on rotor plates. The allowance in the bearing in axial direction causes inequality of airgaps so that one is wider and the other narrower than 2mm according to the design target. However, both airgaps are still uniform. That means an airgap over a particular rotor plate has got a constant thickness. The second case may appear because of angular allowance in bearings so that the rotor plates are not coaxial with the stator anymore. The rotor plates are eventually exposed to non-uniform airgaps. Considering the circumference of the rotor at outer diameter, at a certain angle, the airgap has got minimum thickness unlike at another point displaced by 180deg with maximum airgap. Therefore, the rotor plate tends to bend axially even more because of the point at circumference with thinnest airgap is faced to highest axial force per infinitesimal area. This is in fact positive feedback which may cause mechanical failure of the machine.

2.3.5. Thermal modeling of Axial-Flux Machines

The cooling strategy for the designed machine relies on the aluminium cooling jacket placed in between two segments of stator corepack. The jacket is shaped up internally so that there is a 5mm thin duct in the middle having a shape of extruded annulus. The inner surface of the duct has got grooves making the coolant flow in the duct turbulent. Analytical calculation of the heat transfer coefficient using the coolant parameters, mass flow rate and dimensions of the duct in the jacket significantly simplifies and speeds-up the design process. The calculation of the heat transfer coefficient are based on Dittus-Boelter correlation for Nusselt number Nu. Reynolds

number Re assumes turbulent flow in the cooling duct. The thermal correlations require validation by Computational Fluid Dynamics analysis carried out externally.

Equivalent transient lumped-parameter thermal networks are convenient modelling tools for electrical machines. There are clear analogies between electrical and equivalent thermal circuits. The thermal circuit for Spoke-Axial Flux machine considers the stator only because of allocation of power losses in the machine and currently unknown thermal behaviour of the entire powertrain in the integrated state. The equivalent transient model allows to investigate temperature rise at any operational point or to simulate heat runs of the machine.

Thermal correlations of heat transfer coefficient for the cooling jacket in conjunction with the equivalent transient thermal circuit helps to optimize flow rate by tracking dependency of temperature rise on the flow rate. The modelling effort on the thermal side will also consider sensitivity of winding temperature to critical parameters such as quality of contact between the stator core and the cooling jacket.

2.3.6. Control strategies for MG2, efficiency of electrical drive and impact of machines‘ parameters variation

Control design must be permanently in a loop with electromagnetic design to ensure efficient operation of the drive in the entire Torque-vs-Speed range. The clear goal is to maximize efficiency of the drive. But this requires analysis showing how every particular control strategy (Id=0, MTPA, Maximum efficiency, Field weakening) impacts the efficiency. Thus it is convenient to present efficiency maps of the drive for various operational conditions for all considered control strategies. It is not required to design actual controllers, but more likely to investigate steady state efficiency at any operational point.

Power electronics is an integral part of the drive and its behaviour in terms of loss is included in the simulation of drive efficiency. The work presumes given PE components and Discontinuous PWM scheme.

According to the specification, the machine may operate at temperatures as low as -40deg C and can reach up to 160degC in terms of the winding temperature having impact on normalized magnet flux linkage and the winding resistance. Moreover, the DC voltage has significant swing and inductances may vary with level of electrical loading of the machine. These variations of parameters create uncertainties in modelling of the drive efficiency and need to be addressed.

2.3.7. Design improvements for the next generation prototype

The first prototype of MG2 is a proof of concept of a novel machine topology. There is definitely a room for further improvements in terms of power density, reduction of magnet mass or possible ideas leading toward easier and cheaper manufacturing. A good example would be Spoke-AFPM machine with casted aluminium backplate saving significant portion of leakage flux and therefore, raising the ratio between power and the magnet mass.

3. Concept generation

The outcome of concept selection process is the most feasible topology of an electrical machine for defined application. A side benefit of concept selection process is better understanding and prioritization of customer's needs, reflected into design criterions. Among the other criterions, the top priorities were identified as:

- Short axial length <200mm
- MG2 must fit into SAE0 housing in terms of its diameter
- High power density
- Peak efficiency above 95%
- Ability to operate in field-weakening mode from 1300 up to 2800 rpm with consideration of minimal DC link voltage of 500VDC

Design of electrical machines doesn't lead to one particular solution, which might be unitarily considered as the greatest. It is rather balanced trade-off in between many variables involved in design of the machine. The prioritization process helps to narrow down focus of the designer so that the most critical design objectives are met eventually.

3.1. Initial assessment of considered machine topologies

The initial selection of electrical machines for hybrid drives includes variety of different topologies. According to outcomes of literature survey, induction machines alongside with synchronous machines take frequently place in HEV powertrains. Both of these, in sense of operational principle, different families of machines may be laid out in axial or radial plane. Out of radial synchronous machines, surface-mounted-, inset- and embedded-permanent magnet topologies, and switched reluctance machines are considered as competitive for traction purposes. Synchronous permanent magnet axial flux machines are subject of ongoing research, and need to be included due to their advantageous axial length. Fig. 3-1 shows cross-sectional views of considered radial-type machines, followed by Fig. 3-2 depicting 3D models of permanent-magnet axial flux machines.

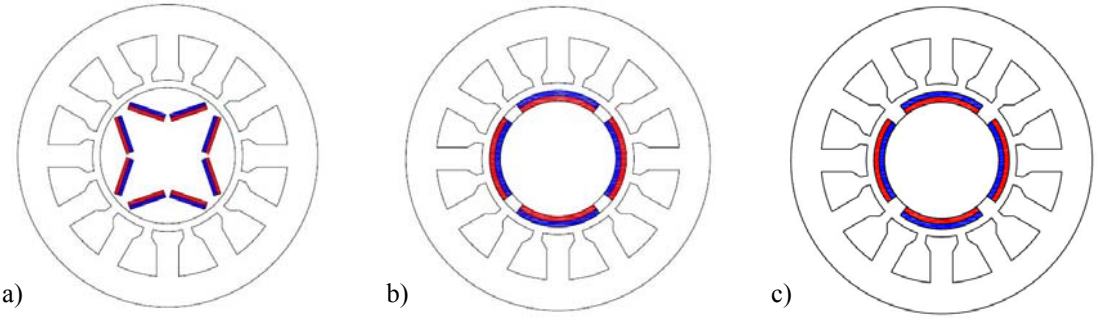

a) b) c)

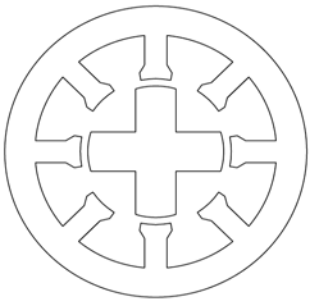

d)

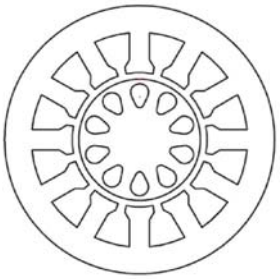

e)

Fig. 3-1 Cross-sectional views of radial-flux machines: a) Embedded-PM machine, b) Inset PM machine, c) Surface-mounted PM machine, d) Switched-reluctance machine, and e) Induction machine

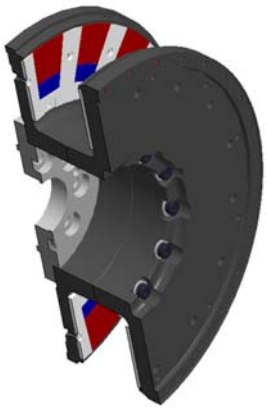

a)

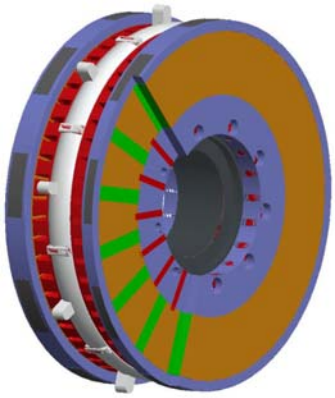

b)

Fig. 3-2 Cross-sectional views of axial flux permanent magnet machines: a) with Iron Poles, and b) PMs embedded in spoke arrangement

Both concepts of axial flux machines involve two-rotor topology with toroidally-wound stator in the middle. Such layout simplifies layout of the cooling system by employing only one cooling jacket in the middle of the sandwiched stator structure. The toroidal winding couples electomagnetically both halves of the stator corepack.

The axial flux PM machine with iron poles is derivative of surface-mounted PM machine in terms of magnetic filed distribution, as illustrates Fig. 3-3.

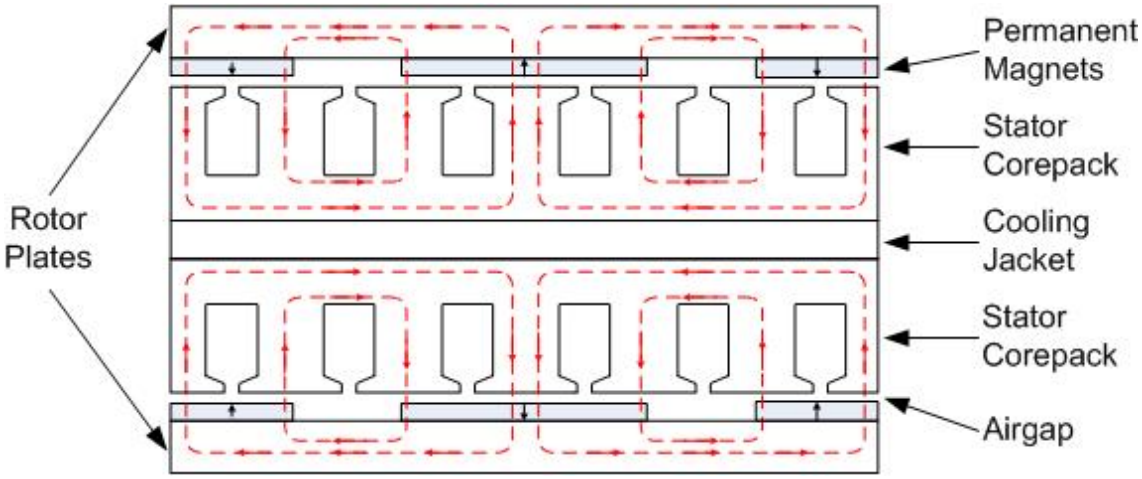

Fig. 3-3 Distribution of magnetic field within axial-flux machine with iron poles

The iron poles are placed radially at a lower diameter below permanent magnets, and are functional only during field weakening operation, when negative d-axis current is enforced to the stator winding.

The drawback of this topology is in inherently decreased power density since certain proportion of the each winding turn in a slot is not faced to a field of PMs and therefore, do not participate in torque production. The spoke-PM machine should therefore fit into a smaller envelope for given ratings since it is naturally feasible for field weakening, and does not have to employ any additional flux weakening feature.

The initial assessment of features of considered machines shows Pugh Concept Selection matrix on Fig. 3-4. Each individual machine topology is compared against so-called datum that means a machine, which is a baseline for the comparative process. A surface-mounted PM machine has been selected as a datum due its relative matured technology and well understood properties. The actual comparison is carried out in a relative manner. The positive (+) sign indicates improvement against the datum, whereas negative (-) sign stands for worsening of the assessed parameter. Eventually, a group of machines with relatively highest scoring of positive signs passes through the Pugh Concept Selection for further, more accurate comparison, at least by initial sizing and performance calculations. This selection method is relative, based on existing experience with this particular class of machines in terms of their rating.

Criteria/Concept	Datum						
	Surface-mnt. Synchronous PM	Switched-Reluctance	Embedded-V Synchronous PM	Inset Synchronous PM	Axial-Flux Synchronous PM with IP	Axial-Flux Synchronous Spoke PM	Induction Machine
Axial length	S	S	+	+	+	+	-
Outer diameter	S	S	+	+	-	-	-
Efficiency	S	-	S	S	S	S	-
Power density	S	S	+	+	+	+	-
Field weakening	S	S	+	+	+	+	+
Total Σ +	0	0	4	4	3	3	1
Total Σ –	0	1	0	0	1	1	4
Total Σ S	5	4	1	1	1	1	0

Fig. 3-4 Pugh concept selection matrix for traction motor generator. (+) indicates improvement, (-) worsening and (S) the same status of a particular parameter in a comparison to the datum.

The Pugh matrix on Fig. 3-4 shows that group of four synchronous machines – radial with inset or embedded permanent magnets, and axial with iron poles and permanent magnets or with spoke magnets only, are proceeded further for more detailed analysis. The Pugh concept selection matrix indicates that permanent-magnet excitation should lead toward more compact size and high efficiency.

3.2. Evaluation of feasible concepts

The initial sizing included candidates marked as „green“ in the pugh matrix for more detailed evaluation. The group of machines proceeding further includes Embedded- and Inset PM radial machines alongside with Axial-flux PM machines with iron poles and with permanent magnets in the spoke arrangement. The initial sizing based on equivalent reluctance circuits for all topologies, estimates size, performance and efficiency according to standard sizing procedures [47] with adequate alterations needed for conversion from radial to axial plane. In terms of cooling capability of water jackets, recommended values of heat transfer coefficient at fixed coolant flow rate according to [47] were considered. The following Tab. 3-1 summarizes outcomes of basic sizing for above-mentioned machines.

Tab. 3-1 Initial sizing of concept machine topologies for traction motor generator

	Embedded-V Synchronous PM	Inset Synchronous PM	Axial-Flux Synchronous PM with IP	Axial-Flux Synchronous Spoke PM
Rated power (kW)	100			
Base speed (rpm)	1300			
Maximum Speed (rpm)	2800			
Field Weakening Capability	Yes			
Peak Efficiency (%)	95.8	95.3	96.2	96.1
Power desity (kW/dm^3)	16.03	12.62	9.06	10.03
Outer Diameter Fits into SAE 0	Yes	Yes	No	Yes
Axial Length below 200 mm	No	No	Yes	Yes

All considered machine topologies might achieve specification in terms of required torque-vs-speed envelope, including field-weakening. Very similar results were achieved in terms of efficiency, when the actual difference can be considered within error margins within scope of initial sizing. However, axial-flux machines bring advantage in terms of axial length reduction. This appears to be beneficial for ICE oriented hybrid systems, when electrical machines are integrated toward the source of prime-power. However, radial type arrangements take advantage in transmission-integrated hybrid powertrain, when epicyclic gears might be nested into the rotor of the machine, and therefore, the radial machine can be well-proportionally sized with bore diameter similar to length of active corepack.

Both concepts of axial flux machines fit within the desired axial length of 200mm. However, lower power density and therefore, higher outer diameter disqualifies the configuration with iron poles. The higher outer diameter may amplify mechanical design and integration issues since axial forces loading the rotor structure are proportional to the airgap surface area. Moreover, any misalignment in terms of the rotor plates will not be exactly co-axial with the stator, in other words tilted, may lead to increased danger of collision in between rotor and stator, especially if both airgaps are not exactly reaching the same thickness.

3.3. Concept of spoke axial-flux permanent magnet machine

The major difference against the configuration with iron poles is in the layout and structure of rotor plates. Instead of using solid rotor plates with magnets mounted on the surface of the plate, and secured by the retention system, Spoke concepts represent completely different approach. The rotor structure is created out of strip of electrical steel, which is punched during its winding process so that radially distributed pockets for magnets are created, as depicts Fig. 3-5.

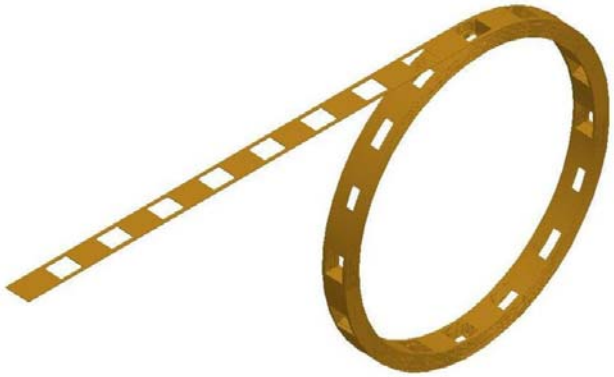

Fig. 3-5 Process of winding up the rotor core out of strip of electrical steel

Such manufacturing process leads to a magnetic circuit of Spoke-PM axial flux machine depicted in terms of distribution of flux lines on Fig. 3-6.

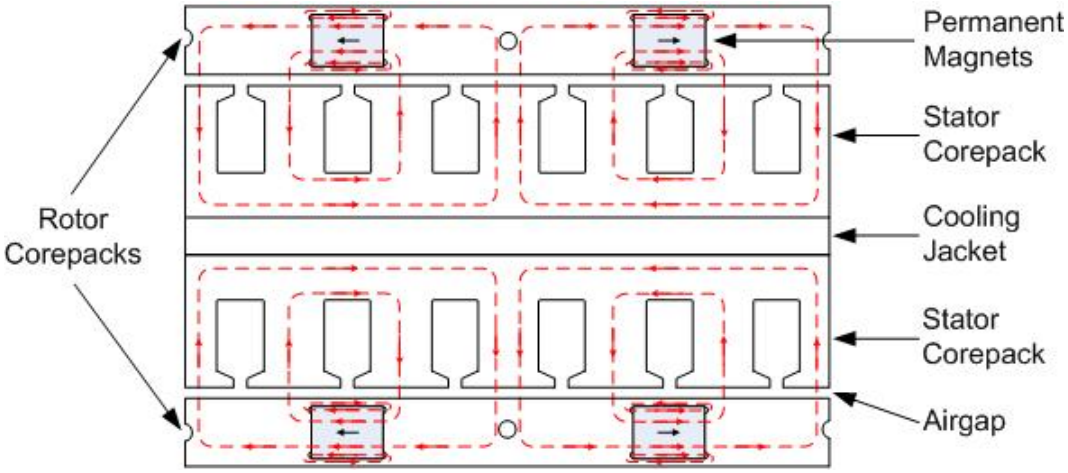

Fig. 3-6 Distribution of magnetic field within axial-flux machine with iron poles

Magnets are inserted into pockets in alternating manner in terms of their polarization so that flux focusing effect is achieved. The electrical steel in between magnets create an iron pole through magnetic flux reaches the airgap, and the stator eventually. The direct axis according to dq0 reference frame takes place in the axis of the iron pole. Having said this, the d-axis armature flux faces significant reluctance of a permanent magnet, which leads to inductance in d-axis being smaller than in q-axis. Therefore, spoke-axial flux machine behaves inherently like a traction motor, producing reluctance torque alongside with magnet torque during field weakening operation.

Main drawbacks of this topology are in complicated mechanical arrangement. Holes are drilled into a corepack so that pins can be inserted there in order to stiffen mechanically its structure. The strip-wind structure by itself is wound on a inner stainless steel ring, and similarly is retained by outer stainless steel ring counteracting centrifugal forces.

From electromagnetic stand point of view, bridges holding axially magnets in the rotor pockets represent significant leakage flux path for a magnet. This may worsen the magnet utilization factor and therefore, lead toward wastage of expensive NdFeB magnet material. However, detailed study supporting these assumptions follows this discussion.

4. Electromagnetic design

The following chapter deals with electromagnetic design of the Spoke-Axial Flux Machine, starting by initial design considerations, and leading towards consolidated design following multiphycsics approach. The outcomes of the electromagnetic design does not lead only to actual construction of prototype and related system integration work, but provide necessary inputs for detailed thermal modelling of the machine, and modelling of the entire electric drive from control stand point of view as well.

4.1. Initial design considerations

Sizing of an electrical machine is an iterative process respecting certain design flow. The initial design inputs, specifically electric (current density *J*), magnetic (flux density B in the airgap and electrical steel both in a rotor and a stator) and thermal (the maximum allowed winding temperature $T_{w,\max}$) loading set up the initial conditions for a design iteration. The specific loading has been selected with respect to recommended and already achieved values for synchronous PM machines:

- Peak airgap flux density: $B_g = 0.9T$
- Maximum magnetic loading of stator teeth: $B_T = 1.8T$
- Maximum magnetic loading of stator backiron: $B_S = 1.6T$
- Nominal stator current density $J < 10\frac{A}{mm^2}$
- Maximum winding temperature $T_w = 160^o C$
- Operational temperature of permanent magnets at $T_{PM} = 70^o C$

These values are the initial sizing inputs, alongside with required power/torque rating of the machine. Fig. 4-1 depicts a flowchart diagram summarizing consequential steps in actual analytical design.

Specific torque production of a machine defines Torque-per-Rotor-Volume (TRV) constant, reaching up to $75kNm/m^3$ for air-cooled aerospace machines, and from $130kNm/m^3$ up to $220kNm/m^3$ for large machines with direct water cooling of stator winding [18]. The TRV ratio is directly proportional to linear current density A and magnetic flux density in the airgap B_g:

$$TRV = \frac{\pi}{\sqrt{2}} k_w A \cdot B_g \cdot \sin(\alpha) \tag{4-1}$$

where k_w is winding constant and $\sin(\alpha)$ indicates displacement angle between rotor flux and armature reaction flux waveforms. Assuming Id=0 operation, those waveforms are displaced by 90deg, therefore maximizing torque production.

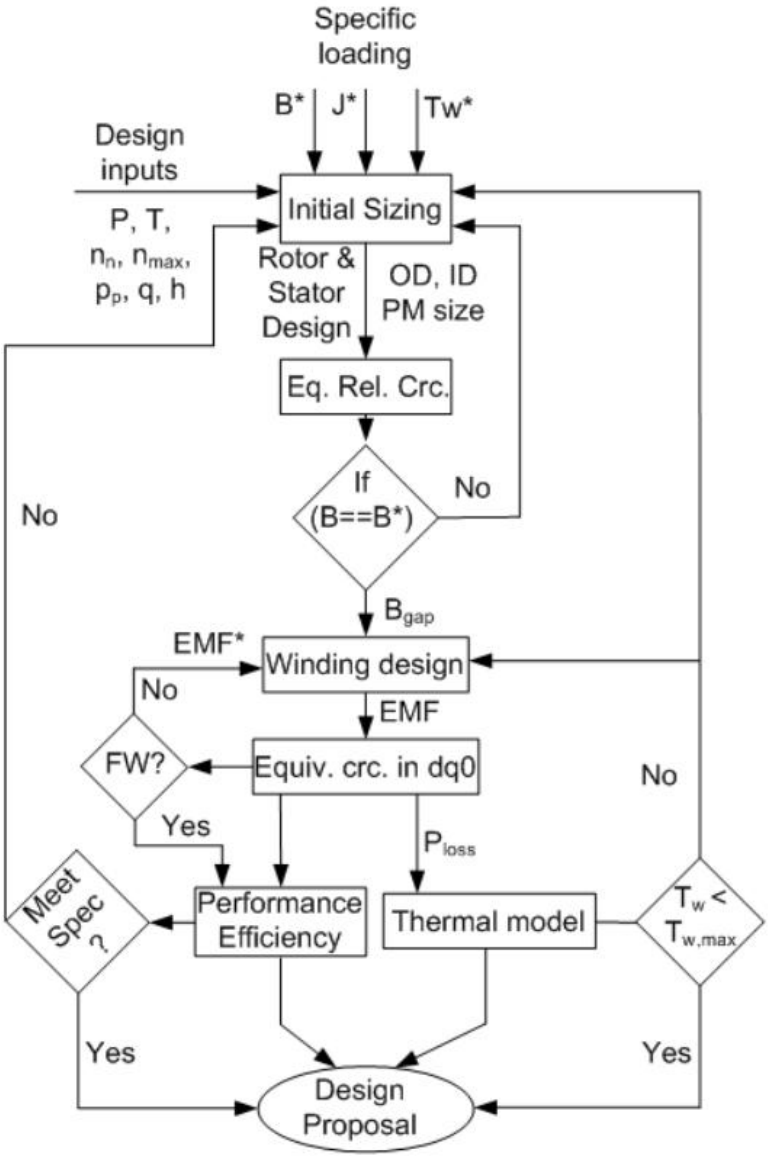

Fig. 4-1 Flowchart of analytical design procedure

Specific magnetic loading in terms of airgap flux density reaches typically for embedded-permanent machines up to $B_g \le 1T$ [48]. Considering winding factor for toroidal winding with one slot per pole per phase to be $k_w = 0.95$, the initial linear current density is set up to $A = 50A/mm$.

The initial outer and inner diameter may be estimated indirectly out of expected efficiency of the machine (95%) at base speed/rated torque, and rated power (100kW) giving amount of heat to be rejected throughout the cooling jacket. Considering the temperature gradient from stator winding to coolant ΔT, the heat transfer coefficient h is given as:

$$h = \frac{P_{loss}}{A_{th} \cdot_{\Delta} T} \tag{4-2}$$

This allows working out the initial minimal required heat dissipation area A_{th} on the stator side facing the cooling jacket and therefore, inner and outer diameter of the active magnetic circuit. Given power loss per stator half of $P_{loss,h} = 2.5kW$, temperature gradient from stator winding to coolant of $55^{o}C$ and conservative assessment of heat transfer coefficient from stator core to the cooling jacket at $1500Wm^{-2}K^{-1}$, the stator heat rejection area should reach at least $0.03m^{2}$.

Selection of aspect ratio in between active outer and inner diameter of the machine has direct impact on achievable torque density [49]. It has been shown [50] that optimal aspect ratio maximizing the power density is $\sqrt{3}$.

Sizing of axial flux machine is sensitive to selection of number of poles. Since the toroidal winding configuration limits from manufacturing stand point of view the number of slot per pole per phase to one, number of poles needs to consider proportionality of slot width versus tooth width, especially at inner diameter, where local saturation may occur. For a given constraints in terms of inner and outer diameter of the machine, 16-, 18- and 20 pole combinations will be further investigated.

One of critical design parameters is airgap thickness given not only by electromagnetic requirements, but primarily by manufacturing aspects, tolerance stack-up on subcomponent groups, and a way of integrating the machine into vehicle's powertrain. Therefore, initial selection of airgap for purpose of electromagnetic design should consider allowances in bearing in terms of axial shifts and angular misalignment alongside with expected tolerances on components. The airgap faces compose out of strip-wound stator and rotor corepacks. Both of these components are manufactured with tolerance of $\pm$0.2mm, giving potential airgap reduction of up to $\pm$0.4mm in a worst-case scenario. The considered double angular contact bearing allows according to specification angular displacement angle of $\pm$0.0566deg and pure axial shift of $\pm$0.328mm. Therefore, only bearing operation may lead in combined case of axial shift and angular displacement to the airgap reduction at the outer diameter by $\pm$0.59mm. These considerations of manufacturing, tolerancing and bearing selection leads toward required mechanical airgap clearance of 2mm. However, airgap size may be subject of reduction for next generation of prototype once manufacturing process is more established.

The described process of selecting initial conditions for design iterations aims to narrow down a number of available design options, and therefore, save time and resources required for actual design process. However, actual design process will lead toward values obtained with higher level of accuracy through precise analytical and numerical calculations.

4.2. Electromagnetic Analysis of Spoke Axial Flux machine

According to the flowchart diagram at Fig. 4-1, actual electromagnetic analysis follows the initial sizing. Magnetic circuit of Spoke-Axial Flux machine may be characterized as non-linear because of presence of bridges holding permanent magnets in the rotor structure. Therefore, it is not applicable to estimate required MMF of permanent magnets throughout a simple flux tube following distribution of fluxlines within the magnetic circuit, as it would be feasible for instance for Surface-mounted PM

machine. A convenient method is to apply a reluctance network to analysis of the magnetic circuit, and obtain distribution of magnetic field density within the machine by iterative solution with selected convergence criterion. Because of the non-linear nature of the machine, it is appropriate to assess level of stray flux across various potential leakage fluxpaths using Finite-Element Analysis, and include this into the iterative solution.

4.2.1. Equivalent reluctance circuit

A solution of magnetic circuit may take an advantage out of analogy in between magnetic and electric circuit. A voltage source is represented by source of MMF, current is equivalent to magnetic flux, and resistance to magnetic reluctance. Following distribution of magnetic fluxlines within the magnetic circuit according to Fig. 3-6, a network of equivalent MMF sources and reluctances may be sketched over layout of the magnetic circuit as depicts Fig. 4-2 a) below:

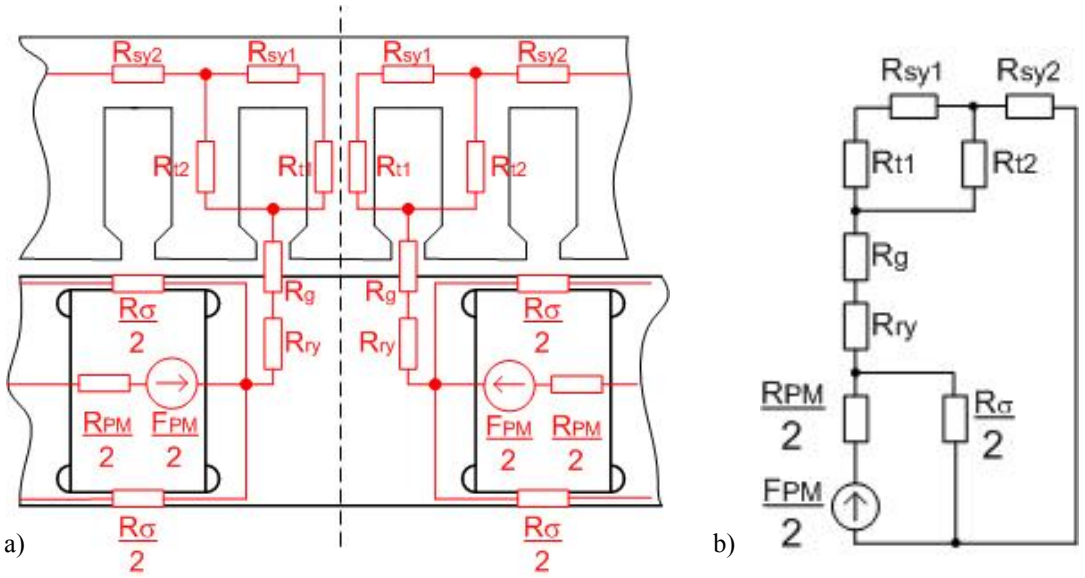

Fig. 4-2 a) Equivalent magnetic circuit of Spoke-Axial Flux machine on top of the layout of the machine. b) Redrawn version for actual iterations**.**

It is sufficient to calculate magnetic field per one-half of a pole since magnetic field is distributed symmetrically against axis of a permanent magnet, as shows Fig. 4-2 b) Therefore, only a half of magnet's tangential length as well as only half of peripheral airgap length is considered. On the stator side, the equivalent circuit accounts for a half of physical flux tube too.

A MMF developed by a permanent magnet F_{PM} depends on magnet tangential thickness l_t and coercitive force of the magnet H_c:

$$F_{PM} = l_t \cdot H_c \tag{4-3}$$

Additionally, permanent magnet accounts for its reluctance R_{PM}:

$$R_{PM} = \frac{l_t}{\mu_0 \mu_{PM} l_a l_r} \tag{4-4}$$

where μ_{PM} represents relative permeability of the magnet material, l_a magnet length in axial direction and l_r length in radial direction. The variable magnet tangential length

l_t takes into account only a half of actual tangential thickness due to previously mentioned symmetry. Following Fig. 4-3 helps in understanding of geometric variables required for calculations related to the equivalent reluctance circuit.

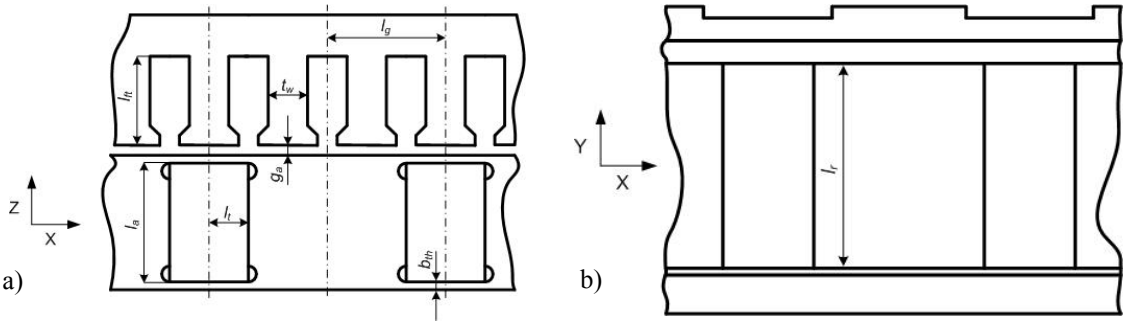

Fig. 4-3 Definition of geometric variables of the Spoke Axial-Flux Machine a) in XZ, b) in XY plane**.**

Reluctance of the airgap considers only a half of its circumferential length l_g due to applied symmetry:

$$R_g = \frac{g_a}{\mu_0 l_g l_r} \tag{4-5}$$

where g_a represents airgap length in axial direction.

Estimation of reluctances of stator teeth and corresponding parts of stator back iron requires understanding of magnetic loading of each individual stator part. Assuming that the stator tooth aligned with the direct taxis is faced to the peak of the flux density waveform in the airgap $B_{g,pk}$, the expected magnetic loading is

$$B_{T1} = \frac{s_{sp}}{t_w} B_{g,pk} \tag{4-6}$$

where s_{sp} is slot span and t_w is tooth width. The ratio between slot span and tooth width reflects that flux crossing the airgap is in fact focused from a slot span peripheral width into a tooth width whilst penetrating the stator steel.

The neighbouring tooth is facing the airgap flux density waveform at 60deg electrical position, so that the magnetic loading is adequately lower:

$$B_{T2} = \frac{s_{sp}}{t_w} B_{g,pk} \cdot \cos\left(60^o\right) \tag{4-7}$$

Knowing the level of flux density in a stator tooth allows obtaining, based upon BH curve for a given electrical steel, intensity of magnetic field H_t. Then a drop of MMF at a particular tooth is:

$$F_t = H_t \cdot l_{ft} \tag{4-8}$$

where l_{ft} is length of a fluxline in a stator tooth.

Stator tooth conducts magnetic flux ϕ_t proportional to the level of magnetic loading B_t and to geometry of the tooth:

$$\phi_t = B_t \cdot t_w \cdot l_r \tag{4-9}$$

Eventually, stator tooth reluctance is given as:

$$R_t = \frac{F_t}{\phi_t} \tag{4-10}$$

Analogical procedure is applicable to estimation of reluctances of the stator and rotor yoke. Initial condition for calculation of stator teeth and yoke reluctances takes into consideration the targeted values of magnetic loading.

The bridge holding magnets in the rotor structure account for vast majority of the stray flux within the magnetic circuit. The bridge as seen by a magnet almost acts as, in fact, short circuit. Therefore, intention is to minimize axial thickness of the bridge b_{th} in order to maximize its reluctance. Considering that electrical steel of the bridge is entirely saturated, one may assume that magnetic loading of the bridge rises up to $B_\sigma = 2.2T$ as given by particular BH curve. Knowing therefore relative permeability of the saturated bridge $\mu_{r,\sigma}$, the equivalent reluctance of the bridge is:

$$R_\sigma = \frac{l_t}{\mu_0 \mu_{r,\sigma} \cdot b_{th} \cdot l_r} \tag{4-11}$$

Once the bridge reluctance is known, the total stray flux per bridge is given as:

$$\phi_\sigma = \frac{F_{PM} - \Delta F_{PM}}{R_\sigma} \tag{4-12}$$

where ΔF_{PM} is drop of MMF on a permanent magnet.

Besides magnet bridges, there are additional sources of leakage flux:

- stray flux through inner carrier ring of the rotor, made of austenitic stainless steel
- a single turn of unslotted turn of electrical steel at inner diameter, acting as an additional bridge in tangential direction with regards to magnet position
- stray flux behind the rotor plate, leaking out of saturated bridges
- the outer retaining ring made of austenitic stainless steel
- the sensing ring on top of one of the rotor plates with castellations for Hall-effect sensor-based position estimation

Though, except the leakage path through the single unslotted turn of electrical steel, all of these leakage fluxpath exist in fact in materials with relative permeability at one, or converging to one, these additional cases need to be evaluated by Finite-Element Analysis and added to the total leakage flux.

Actual solution of the equivalent reluctance circuit according to Fig. 4-2 b) provides airgap flux ϕ_g. Then peak value of airgap flux density B_g is given as:

$$B_g = \frac{\pi}{2} \cdot \frac{\phi_g}{l_r \cdot \tau_p} \tag{4-13}$$

where τ_p represent polespan at mean magnet diameter.

Overall accuracy of calculations by previously described method may be increased by dicretizing the equivalent circuit in radial direction so that there is more accurate representation of variable pole span. This allows considering of variable magnetic loading of stator teeth, which is decreasing with rising diameter.

4.2.2. Sizing of Permanent Magnets

A number of different combination of magnet tangential and radial thickness may lead toward desired level of flux density in the airgap. However, certain combinations of magnet dimensions could be inefficient, or even wasteful in terms of overall magnet mass per entire machine. Therefore, it is desirable to find out such magnet dimensions for a fixed stator configuration so that overall magnet mass is minimized.

Limiting factor for the sizing permanent magnets are the bridges holding magnets in their place. Results of a mechanical analysis have shown that minimal required axial thickness of bridges is 2mm, ensuring that the rotor structure will resist combined mechanical loading by axial magnetic and centrifugal forces.

Fig. 4-4 presents outcomes of parametric sizing of permanent magnets. Solid curves are parameter of magnet axial and tangential thickness providing peak airgap flux density. The same plot includes magnet mass as a parameter of axial and tangential magnet thickness represented by dashed curves. The tangential magnet thickness is considered as independent variable, allowing matching up interrelation between airgap flux density and magnet mass per reference axial and tangential magnet thickness. In order to achieve required $B_g = 0.9T$, the magnet axial thickness must exceed 30mm whilst considering maximum magnet tangential thickness of 30mm given by manufacturing constraints.

Assuming magnet axial thickness of 30mm, the tangential thickness reaches 20mm resulting in $B_g = 0.9T$ at magnet mass of 13.7kg. However, a combination of magnet axial thickness of 32mm and tangential thickness leads to the same value of B_g, but at required magnet mass of 10.9kg, providing saving of 2.8kg of magnet material.

Fig. 4-4 relates to 18-poles configuration of the spoke axial flux machine in particular. Similar calculations may be performed for different number of poles as well. Stator design for considered 16-, 18-, and 20 pole combinations always assumes one slot per pole per phase layout.

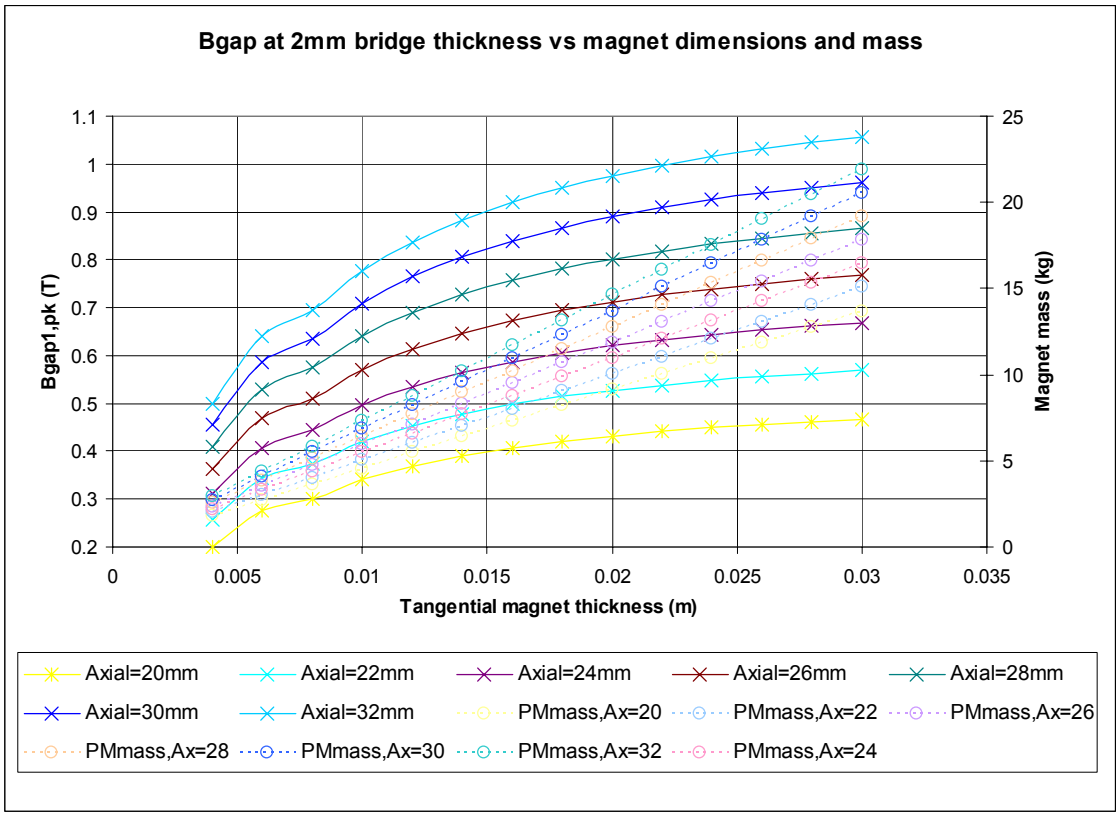

Fig. 4-4 Targeted airgap flux density as a function of magnet thickness in tangential and axial direction (solid curves), and dependency of magnet mass on tangential and axial dimensions of a magnet (dashed curves)

4.2.3. Induced voltage and Winding analysis

The actual winding design needs to reflect the character of machine's operation as a part of variable-speed drive. Considering the base speed at 1300rpm, the open-circuit voltage E at that speed must allow operation in motoring mode under Id=0 control strategy at entire torque range. The base speed is also considered as the very minimum speed when the machine enters the field-weakening mode, characterized by adjusting the current angle β so that the voltage drop $X_d I_d$ helps to compensate for excessive open-circuit voltage. Both operation under Id=0 and field weakening control algorithm are depicted in terms of vector diagrams on Fig. 4-5.

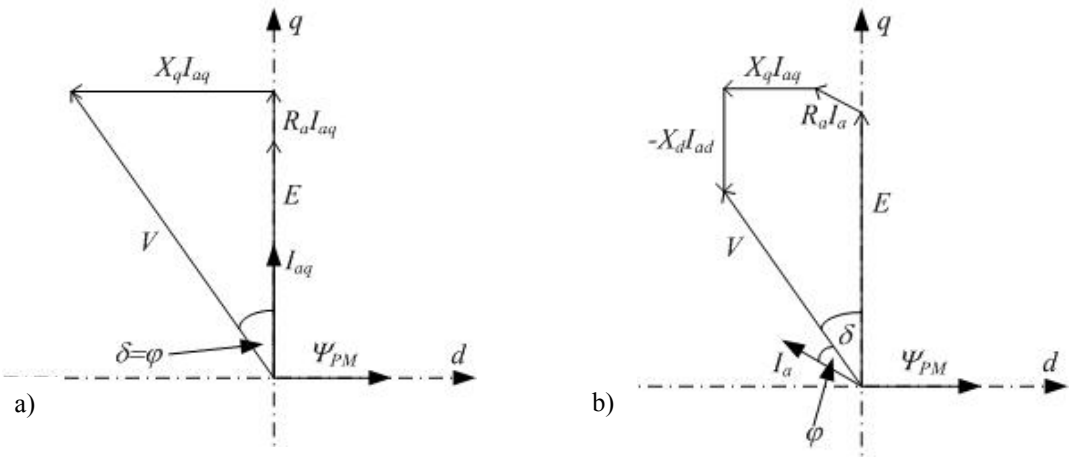

Fig. 4-5 a) Operation under Id=0 control strategy, b) in field weakening mode

On one side, concerning Fig. 4-5 a), E must be selected at base speed in such a way so that the input converter voltage will be sufficient to cover the voltage drops on winding resistance and q-axis inductance besides actual open-circuit voltage. On the other side, the drive must be able to ensure safe field weakening operation according to Fig. 4-5 b) at minimum input voltage, so that the d-axis current required requirements will not be excessive. The total armature current at maximum speed, and therefore full field weakening operational condition must be still within the converter ratings.

The actual open-circuit voltage E depends in terms of machine design on the winding configuration and level of the airgap flux:

$$E = 2\pi \cdot f_s \cdot k_w \cdot N_{ph,s} \cdot \phi_g \tag{4-14}$$

where f_s is the stator electrical frequency at base speed, k_w represents winding factor and $N_{ph,s}$ is number of turns in series per phase. The winding factor k_w decomposes into the winding distribution k_d, winding pitch k_p and skew factor k_s:

$$k_w = k_d \cdot k_p \cdot k_s \tag{4-15}$$

The pitch factor considers ratio of coil pitch y to polespan τ_p:

$$k_p = \sin\left(\frac{y}{t_p} \cdot \frac{\pi}{2}\right) \tag{4-16}$$

The coil pitch of the particular toroidal winding is exactly the same as polespan, therefore, $k_p = 1$.

The winding distribution factor k_d represents ratio of geometric sum of induced voltage on active coils sides to their arithmetic sum:

$$k_d = \frac{\sin\left(\frac{q_s}{Q_p} \cdot \frac{\pi}{2}\right)}{q_s \cdot \sin\left(\frac{1}{Q_p} \cdot \frac{\pi}{2}\right)} \tag{4-17}$$

where Q_p is a number of slots per pole and q_s number of slots per pole per phase.

Skewing of stator slots is not considered due to manufacturing constraints, which may lead to increased distortion of induced voltage and higher torque ripple. However, an angular displacement of rotor plates in terms of alignment of their magnetic axes would have the same effect. Offset angle analysis will be further described in section 4.4.3.

4.2.4. Inductances

Spoke Axial flux permanent magnet machine is considered as inverse-salient reflecting variable profile of reluctance as it is seen by the stator armature current reaction field. Once the armature current pattern is aligned in q-axis, the armature reaction flux closes through the iron poles of the rotor in between permanent magnets as is depicted on Fig. 4-6 b). The alignment in d-axis directly either opposes or supports the main magnet flux concentrated into axis of the iron pole. However, the d-axis

armature reaction flux needs to overcame a significant reluctance represented by a permanent magnet and a bridge holding the magnet.

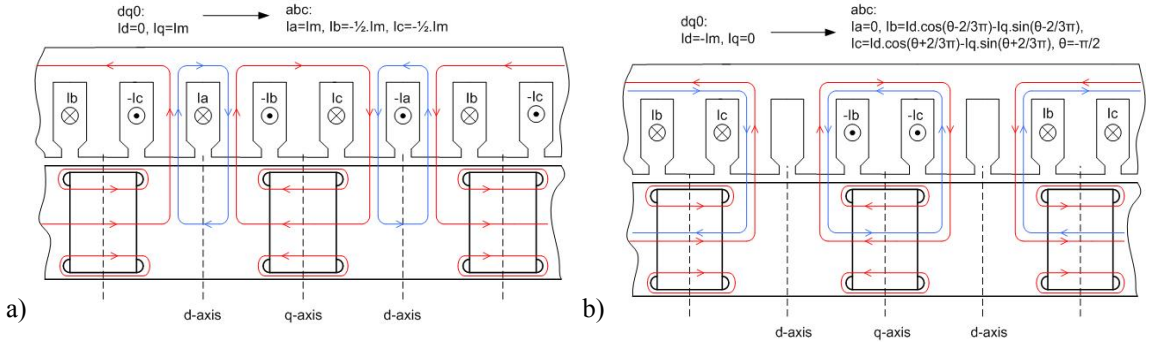

Fig. 4-6 a) alignment of stator armature current pattern vs. rotor in q-axis and b) in d-axis

The adequate currents according to patterns depicted on Fig. 4-6 in abc reference frame may be obtained by inverse-Park transformation so that:

$$\vec{k}_{abc} = \vec{T}_{dq0}^{-1} \cdot \vec{k}_{dq0} \tag{4-18}$$

where $\vec{k}_{abc}$ is vector of variables in abc, $\vec{k}_{dqo}$ is vector of variables in dq0 reference frame and $\vec{T}_{dqo}^{-1}$ is inverse-Park transformation matrix:

$$\vec{T}_{dqo}^{-1} = \begin{bmatrix} \cos(\vartheta_r) & -\sin(\vartheta_r) & 1 \\ \cos\left(\vartheta_r - \frac{2\pi}{3}\right) & -\sin\left(\vartheta_r - \frac{2\pi}{3}\right) & 1 \\ \cos\left(\vartheta_r + \frac{2\pi}{3}\right) & -\sin\left(\vartheta_r + \frac{2\pi}{3}\right) & 1 \end{bmatrix} \tag{4-19}$$

where ϑ_r is actual displacement angle of the current space vector $\vec{k}$ with regards to the q-axis, giving $\vartheta_r = -90^o el$ for d-axis and $\vartheta_r = 0^o el$ for q-axis. The current space vector $\vec{k}$, which is in fact projection of three-phase variables, is given as:

$$\vec{k} = \frac{2}{3}\left(k_a(t) + k_b(t) \cdot e^{j\frac{2\pi}{3}} + k_c(t) \cdot e^{j\frac{4\pi}{3}} \right) \tag{4-20}$$

where $k_a(t)$, $k_b(t)$ and $k_c(t)$ are three-phase variables [51].

The effect of armature reaction on the airgap flux density illustrates Fig. 4-7. The flux density waveform for full armature reaction in d-axis illustrates effectively a case of defluxing, in other words suppressing of first harmonic of airgap flux density in the airgap. The case for the armature reaction due to the maximum q-axis current shows deformation of the airgap flux density, which may lead to local saturation of the stator teeth, and therefore needs to be considered during actual design.

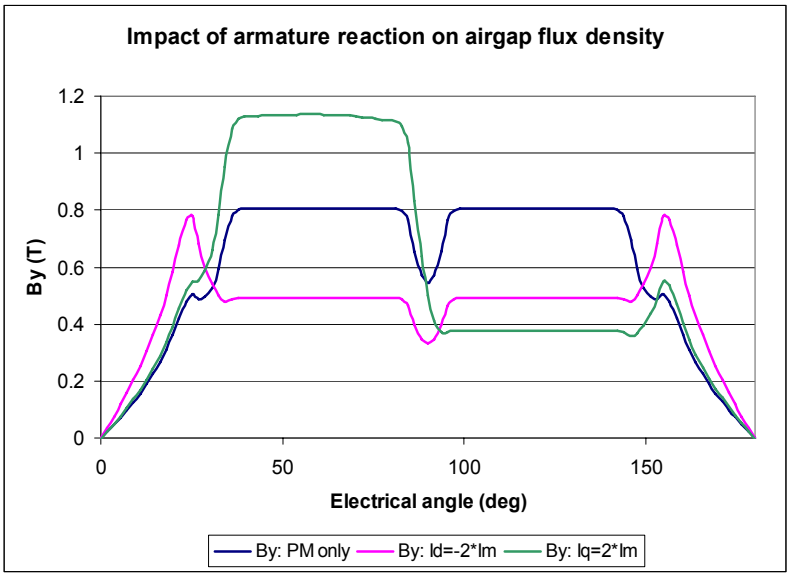

Fig. 4-7 Impact of armature reaction for maximum in d- or q- axis on the airgap flux density waveform obtained by Finite-Element Analysis

An effective way, how to investigate true fluxpath for armature reaction flux is to disable permanent magnets and energize stator winding at d- and q-axis alignment separately. Following Fig. 4-8 shows waveforms of airgap flux density for alignment purely in d- and q- axis at various current levels up to maximum 2p.u. current obtained by FEA.

a)

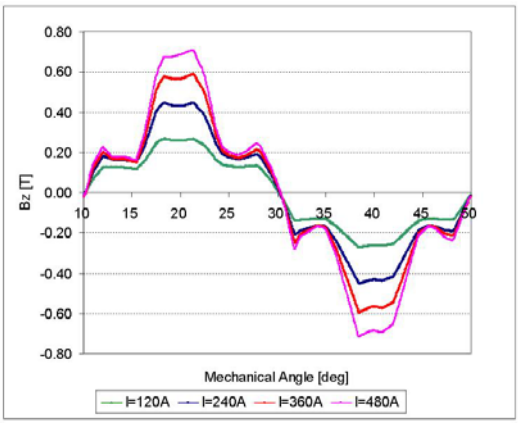

b)

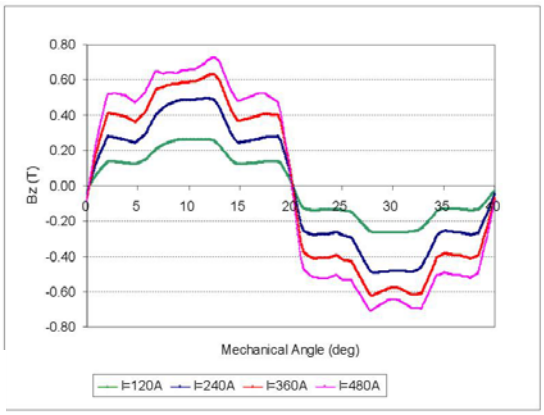

Fig. 4-8 Airgap flux density due to pure armature reaction flux in a) d-axis, b) q-axis rotor alignment

Such waveforms may help to determine armature reaction fluxpath in the airgap and hence, the effective airgap for both d- and q- axis alignments.

The actual inductance depends on geometry of the machine, number of turns in series of the stator winding, and indirectly on the effective airgap length g'' [18]:

$$L = \frac{3\mu_0 \cdot D_m \cdot l_r \cdot \left(k_w \cdot N_{ph,s}\right)^2}{\pi \cdot p_p^2 \cdot g''} \tag{4-21}$$

where p_p is number of polepairs.

The d-axis inductance is then obtained by substituting g'' by effective airgap in d-axis g''_d, obtained as [18]:

$$g_d^{''} = \frac{g^{'}}{k_{1,ad} - \frac{k_1 \cdot k_{\alpha d}}{1 + P_m \cdot R_g}} \tag{4-22}$$

where $g^{'}$ is physical airgap corrected by Carter's coefficient k_c, coefficient $k_{1,ad}$ represents ratio in between the first harmonic component to flat-top value of armature reaction flux in d-axis, $k_{\alpha d}$ considers pole arc to pole pitch ratio, and k_1 is constant considering ratio of fundamental to flat-top flux density waveform in the airgap due to armature reaction.

$$g_q^{''} = \frac{g^{'}}{k_{1,aq}} \tag{4-23}$$

where $k_{1,aq}$ represents ratio in between the first harmonic component to the flat-top value of armature reaction flux in d-axis.

4.2.5. Model in dq0 reference frame

Mathematical model of Spoke axial flux machine needs to fulfil a commonality role for further modelling of the machine. Alongside with actual performance estimation, such model should link with efficiency calculations, be convenient for control design, and provide enough flexibility for modelling of an electric drive as a part of entire vehicle's powertrain. A frequently used approach is to apply Park's transformation and recalculate variables from abc reference frame into dq0 reference frame applying the transformation matrix $\vec{T}_{dq0}$, as may be found in literature [51].

The actual set of equation describing a synchronous permanent machine in dq0 reference frame may be rewritten into a following form with torque production defined as [58]:

$$T_{em} = \frac{3}{2} \cdot p_p \cdot \left(\Psi_{PM} \cdot i_q + (L_d - L_q) \cdot i_d \cdot i_q \right) \tag{4-24}$$

where Ψ_{PM} is flux linkage constant, obtained from peak value of Back-EMF E_{peak} at base mechanical speed $\omega_{m,base}$ as:

$$\Psi_{PM} = \frac{E_{peak}}{\omega_{m,base} \cdot p_p} \tag{4-25}$$

The voltage equations follow equivalent circuits of the machine in d- and q- axis, as they are depicted on Fig. 4-9.

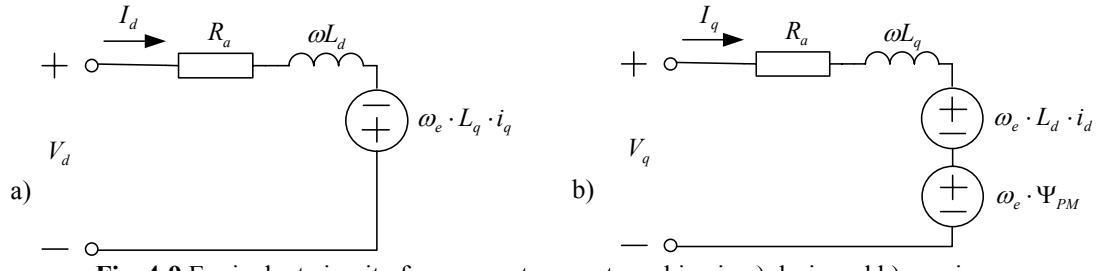

Fig. 4-9 Equivalent circuit of permanent magnet machine in a) d-xis and b) q-axis

The voltage equations corresponding to Fig. 4-9 are then:

$$\begin{aligned} V_d &= R_a \cdot i_d + L_d \frac{di_d}{dt} - \omega_e L_q i_q \\ V_q &= R_a \cdot i_q + L_q \frac{di_q}{dt} + \omega_e L_d i_d + \omega_e \Psi_{PM} \end{aligned} \tag{4-26}$$

The peak phase voltage V_{pk} in abc reference frame would then be:

$$V_{pk}^2 = V_q^2 + V_d^2 \tag{4-27}$$

which leads to restriction of maximum available voltage with regards to DC-bus voltage

$$V_{pk,\max} = \frac{V_{DC}}{\sqrt{3}} \tag{4-28}$$

The peak phase current is analogically to Equ. (4-27) given as:

$$i_{pk}^2 = i_q^2 + i_d^2 \tag{4-29}$$

The machine's model presented in set of Equations (4-24) – (4-29) is valid only for a case of linear machine's parameters. However, it is expectable that the actual machine might be nonlinear, especially in terms of inductances, so that $L_q = f(I_q)$ and $L_d = f(I_d)$. The phenomena of saturation will be subject of a Finite-Element Analysis in Chapter 4.4.5.

4.2.6. Estimation of machine's performance and field weakening capability

The initial performance evaluation focuses mainly on available torque production, ability to field weaken and overall fit into restriction defined by converter specification. Considering the most basic Id=0 current control strategy, the electromagnetic torque production is given by Equ. (4-24) with considering i_q current only:

$$T_{em} = \frac{3}{2} \cdot p_p \cdot \Psi_{PM} \cdot i_q \tag{4-30}$$

The Id=0 current control strategy needs to be available up to maximum torque/base speed load point so that the machine does enter the field weakening mode only beyond its base speed. Since power electronics component are sized up in terms of rated current concerning the peak current of the electrical machine, the maximum current at whatever distribution in d- and q- axis needs to fulfil Equ. (4-29).

The transition into field weakening depends according to Equ. (4-26, 4-27, 4-28) for a fix speed and given parameters of the electrical machine on DC bus voltage. Field weakening control is in fact voltage-tracking control so that once Equ. (4-27, and 4-28) are not fulfilled, the controller increases proportion of negative d-axis current, and therefore decreases voltage in q-axis according to Equ. (4-26). Therefore, the electric design of the machine considers the minimum DC bus voltage as a design case. Hence, higher is the DC bus voltage over the minimal value, greater is availability of a current control strategy before voltage-tracking control is imposed as illustrates Fig. 4-10:

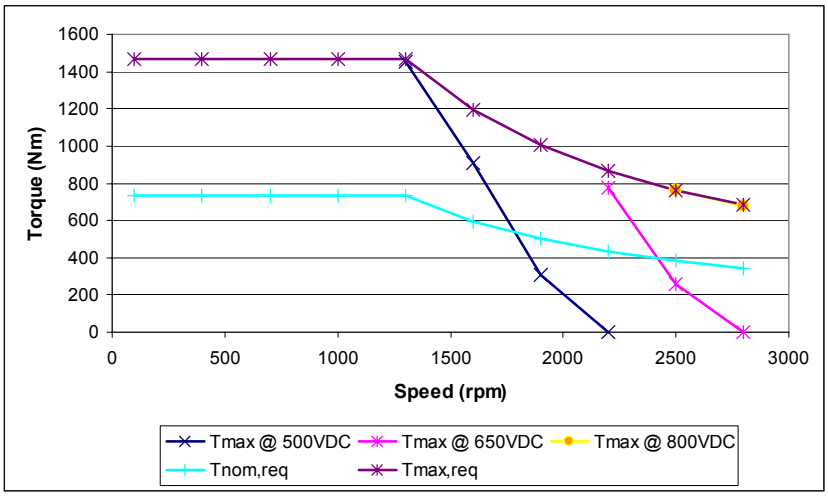

Fig. 4-10 Impact of DC bus on transition of controller into field weakening.

The maximum DC bus voltage can reach up to 800 VDC at full state of charge of the battery. The DC bus voltage is in fact determining when the controller needs to transit into the field weakening mode. This is occurring particularly for the maximum DC bus voltage almost at maximum power/maximum speed loadpoint, as Fig. 4-10 depicts. Therefore, the d-axis current controller should preferably include outer loop comparing available and required converter voltage, and if the required voltage is excessive, use the difference as reference error signal for d-axis current controller. This will ensure superiority of field weakening over actual current control strategy, and therefore safe and reliable operation of the electric drive.

The design constraints from machine's side in field weakening include alongside with voltage constraint the phase current limitation. The total current at nominal power at maximum speed needs to be below the current at nominal torque at base speed. This ensures that the total $R_a \cdot I^2$ loss, or total loss once iron loss are included, are within the loss limit so that the machine is within nominal torque/power operation not thermally overloaded. Profiles of phase current at nominal and maximal torque/power loading depict Fig. 4-11 below.

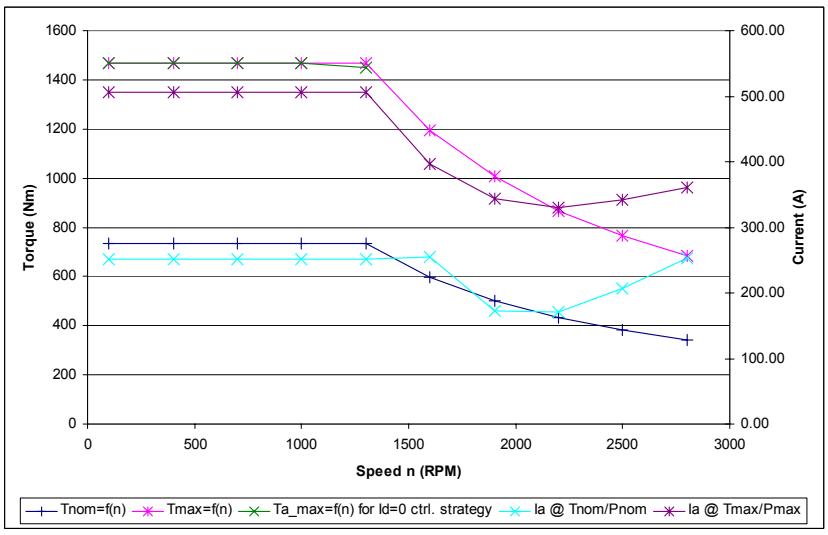

Fig. 4-11 Profiles of phase current at nominal and maximal torque/power loading

An electric machine in hybrid electric vehicle operates in wide operational zone in terms of load torque and reference speed. In order to evaluate overall performance of

the machine in a vehicle, the machine's efficiency needs to be investigated accordingly. Feasible representation of efficiency is through a 2D look-up table within machine's operational range, which may be applied into overall vehicle's simulation model. A way of visualizing such look-up table is to create an efficiency map, as is depicted on Fig. 4-12 below:

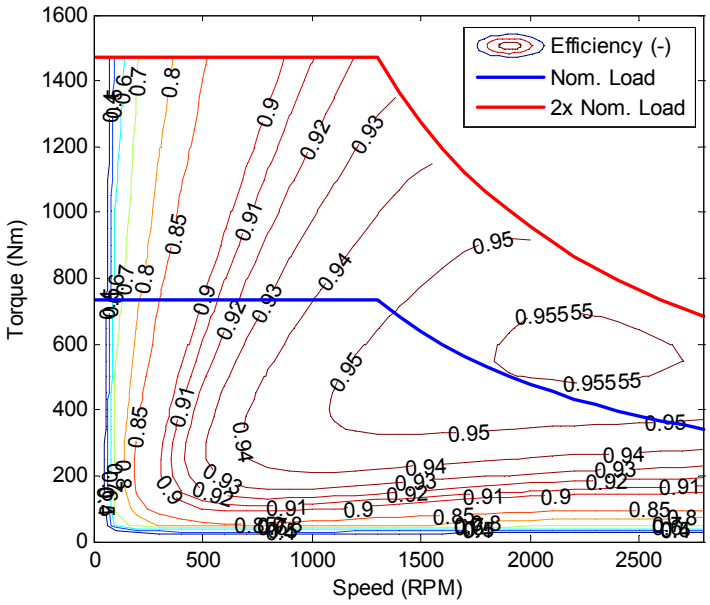

Fig. 4-12 Efficiency of 18-pole design at minimal DC bus voltage of 500V

The efficiency map presented on Fig. 4-12 covers only 1st quadrant, therefore motoring operation, though the drive is designed for regenerative braking in 2nd quadrant too. The efficiency map on Fig. 4-12 considers Field Weakening control algorithm and Id=0 control strategy whenever applicable. However, further enhancement of performance, efficiency and power density of the electric machine and drive may be obtained by selection of appropriate control strategy, as will be discussed in Chapter 6. The following Fig. 4-13 illustrates, how Maximum Torque-per-Ampere control strategy, utilizing reluctance torque alongside with magnet torque, helps to reduce overall phase current, and therefore ratings of the converter switching devices.

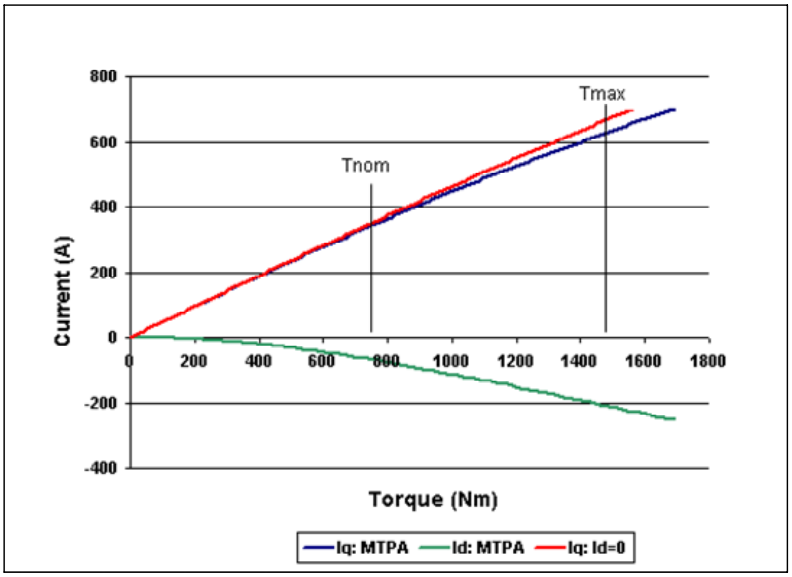

Fig. 4-13 Current demands for a reference torque under Id=0 and MTPA current control strategies

In order to develop the maximum torque of 1469.9Nm, Id=0 control strategy requires 480Arms unlike MTPA control strategy 461Arms. According to Equ. (4-24), MTPA benefits in a case of machine design with relatively high actual difference in between values of q- and d- axis inductances, when the reluctance torque may significantly contribute to overall torque production. An example of such design may be found in [17], where a reluctance-torque participates by up to 47% of the total torque production. The spoke axial flux machine might be considered as magnet-torque oriented due to the reluctance torque, when MTPA is applied, contributes by as little as 6% to the overall torque production at maximum load torque.

4.2.7. Comparison of initial machine design

The initial design considered 16-, 18,- and 20-poles configurations due to above mentioned constraints. The aim of this exercise was to achieve required power/torque at fixed outer diameter in order to carry out diameter-restricted comparison on power density basis. Moreover, selected diameter relates to expected cooling capability and amount of heat loss to be dissipated at nominal torque and base speed. The following Tab. 4-1 below presents referred designs:

Tab. 4-1 Comparison of initial 16-, 18- and 20-pole designs of axial spoke machine

Design	**16 poles / 48 slots**	**18 poles / 54 slots**	**20 poles / 60 slots**
Nominal power Pn @n_b (kW)	100		
Peak power Pmax @n_b (kW)	200		
Nominal Speed n_b (rpm)	1300		
Maximum Speed n_{max} (rpm)	2800		
Nominal Voltage V_{nom} (V_{rms})	204		
Nominal Current I_{nom} (A_{rms})	216	240	264
Current @ nmax, Pnom	167	237	226
Power Density (kW/dm^3)	9.609	9.887	10.494
Number of poles	16	18	20
Back-EMF @n_b (V_{rms})	157	141	129
Peak Airgap Flux density, 1st B (T)	0.84	0.94	0.97
Ld (mH)	0.599	0.230	0.182
Lq (mH)	0.713	0.318	0.221
Ra (Ω)	0.0227	0.0178	0.0161
Efficiency @ Pnom, n_b (%):	95.8	95.8	95.4
Winding configuration:	Toroidal, full pitch		
Slots/pole/phase	1		
Turns per slot		5	
Number of parallel paths		2	
Nominal winding temperature (degC)		160	
Coolant composition	50% glycol, 50% water		
Coolant inlet temperature T_{in} (degC)	105		
Nominal Coolant Flow Rate q (l/min)	15		

According to Tab. 4-1, the power density grows with increasing number of poles due to reduced volume of the machine. Higher number of poles requires thinner back

iron both at rotor and stator side. Higher number of poles in general brings also reduction of axial length of the machine.

The predicted EMF has got inverse-proportional trend with regards to the number of poles. The main reason is in impact of number of polepairs on inductance according to Equ (4-24) eventually causing that L_d is greatest for the 16-pole design. Higher L_d allows to reduce required negative d-axis current, or in other words, increase EMF whilst keeping the phase current below 1 p.u. even at maximum speed. As expected, the Back-EMF correlates inverse-proportionally with phase current at nominal speed, that means the total torque production according to Equ (4-30) relies for 16-pole design on Back-EMF, unlike the 20-pole design is more current-oriented in terms torque production. Therefore, the torque constant k_T might be considered as inverse proportional to the number of poles.

The main advantage of 16-pole design appears to be in lower current requirements at base speed and feasibility for field weakening operation due to reduced current at the maximum speed. However, the Id=0 control strategy is available only up to nominal torque at base speed, which is limiting factor for overloading of the machine in constant-torque operation. The input voltage is insufficient due to relatively high EMF and voltage drops across X_d and X_q reactances.

The 20-pole design takes advantage in the shortest axial length out of presented designs on one hand. However, the converter would have to been sized for the highest current on the other hand. An extra issue appears to be at saturation of stator teeth at inner diameter due to space constrains because of the number of stator slots. This may cause manufacturing issues since endwindings at inner diameter tend to overlay.

The 18-pole design appears to be the trade-off between 16- and 20- poles designs in terms of axial length and phase current. It meets the target for availability of Id=0 control strategy up to maximum torque at the base speed. Meanwhile, current requirements at maximum speed do not restrict the field weakening operation. In terms of efficiency, all presented designs reaches similar value, and the differences may be accounted for computational error considering accuracy of the initial sizing. Because of above mentioned consequences, the 18-pole design proceeds further for analysis that is more detailed.

4.3. Iron losses

Besides copper losses, iron losses are among the most significant contributors of power losses in an electric machine. However, iron loss estimation may be affected by certain level of uncertainty due to empirical character of iron loss models with impact on accuracy of calculation. Therefore, it is recommendable to combine several different approaches behind modelling of iron loss.

4.3.1. Analytical approach and expansion of dq0 machine model

A very frequent method for calculation of iron loss is based on a split into hysteresis loss component ΔP_h and eddy current loss component ΔP_{ed} according to [47]. Such model considers actual magnetic loading B and remagnetization frequency

f_r allowing to select iron loss coefficient c_{Fe} according to Epstein test results for specific steel grade. The model uses as a reference specific magnetic loading B_{base} and frequency $f_{r,base}$ at base speed and nominal load.

$$\Delta P_{iron} = \Delta P_h + \Delta P_{ed} = \frac{1}{2} m_{Fe} \left(c_{Fe} \cdot \left(\frac{B}{B_{base}} \right)^{1.6} \cdot \frac{f_r}{f_{r,base}} + c_{Fe} \cdot \left(\frac{B}{B_{base}} \right)^2 \cdot \left(\frac{f_r}{f_{r,base}} \right)^2 \right) \quad (4\text{-}31)$$

where m_{Fe} is mass of electrical steel.

The value of B needs to reflect impact of torque load on distribution of magnetic field in the machine in order to be enough representative. The total magnitude of flux linkage of the winding ψ might be decomposed into d- and q- axis components:

$$\psi^2 = \psi_d^2 + \psi_q^2 \quad (4\text{-}32)$$

Considering variables according to dq0 axis equivalent circuit (Fig. 4-9), the expression for flux linkage in d- and q- axis may obtain the following form:

$$\begin{aligned} \psi_d &= \psi_{PM} + L_d \cdot i_d \\ \psi_q &= L_q \cdot i_q \end{aligned} \quad (4\text{-}33)$$

so that Equ. (4.32) is finally rewritten as:

$$\psi = \sqrt{\left(\psi_{PM} + L_d \cdot i_d\right)^2 + \left(L_q \cdot i_q\right)^2} \quad (4\text{-}34)$$

Eventually, the airgap flux ϕ_g is expressed with considering the total number of winding turns in series $N_{ph,s}$ as:

$$\phi_g = \frac{\psi}{N_{ph,s}} \quad (4\text{-}35)$$

The airgap flux density *B* is then given by Equ (4-13).

The above presented approach allows to map up iron losses for purpose of analytical sizing and design of the machine. However, since the dq0 equivalent model is the preferred path for the system level modelling, it is convenient to expand the dq0 model according to Fig. 4-9. The resistor R_c represents iron losses by the parallel branch of the equivalent circuits on Fig. 4-14 below.

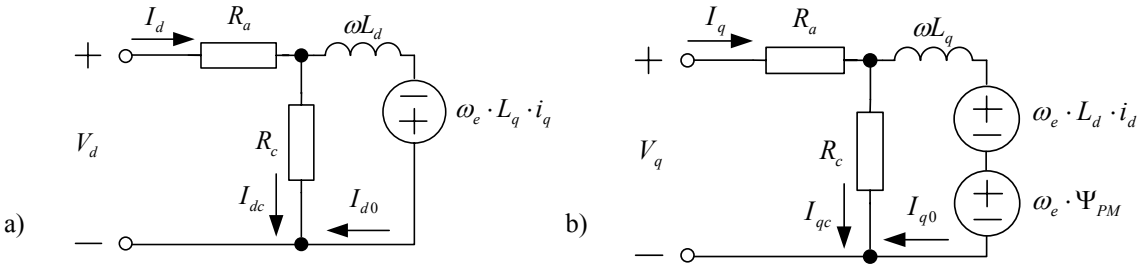

Fig. 4-14 Expanded dq0 equivalent circuit including iron losses in a) d- and b) q-axis

The iron loss resistor R_c decomposes into parallel combination of hysteresis R_h and eddy current loss R_{ed} resistors:

$$R_c = \frac{R_{ed} R_h}{R_{ed} + R_h} \tag{4-36}$$

with values of R_h and R_{ed} obtained at base speed accordingly to losses worked out through Equ (4-31).

4.3.2. Iron loss model considering stator field harmonics

A frequent approach for modeling of iron loss is to apply Steinmetz equation, which is in fact empirical, and relying on measured power loss functions of electrical steel using Epstein test. Steinmetz equation is in certain extend generic, allowing modification of its closed form, as suggests following Equ (4-37):

$$P_{Fe} = k_h \cdot B^{1.6} \cdot f + k_e \cdot B^2 \cdot f^2; k_h = f(f); k_e = f(f) \tag{4-37}$$

The coefficients k_e accounting for eddy current loss and k_h for hysteresis loss are frequency-dependable, since the 1st harmonic of remagnetizing frequency ranges up to 420Hz. The remagnetizing frequency adequately rises for higher harmonics of magnetic field. Such approach of frequency dependable coefficients introduces extra two degrees of freedom into Stainmetz equation, hence ability to approximate power loss functions in a more accurate way. The following Fig. 4-15 depict approximation of iron loss as function of magnetic loading and remagnetizing frequency f_r for M235-35A steel grade at 400Hz and 1000Hz bands:

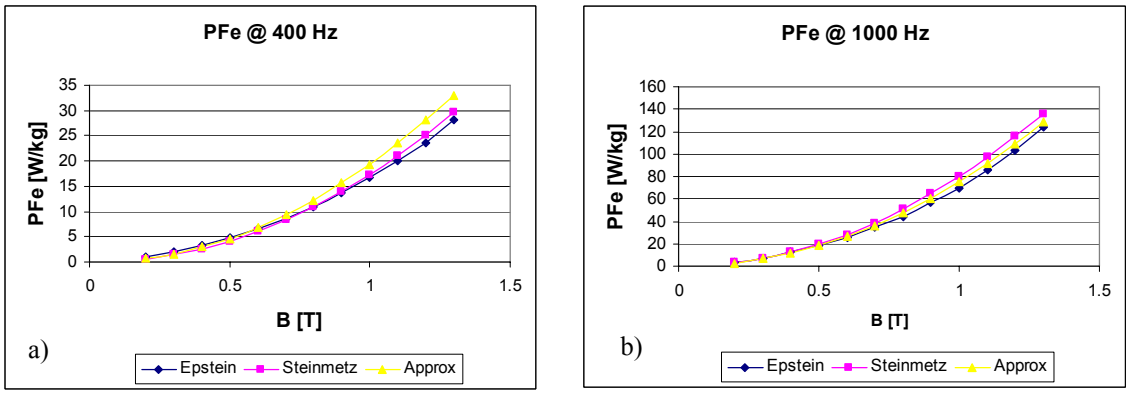

Fig. 4-15 Profile of power loss obtained by Epstein test (blue), approximated by Steinmetz equation (pink), and recalculated after regression (yellow) of ke=f(f) kh=f(f) functions for a) 400Hz, and b) 1000Hz remagnetization frequencies

The actual results of Epstein test are approximated by the Steinmetz equation so that values of k_e and k_h are obtained for each particular remagnetization frequency, as Epstein test data are available up to 2kHz frequency. Then actual coefficients k_e and k_h may be approximated by exponential and polynomial function respectively, as illustrates following Fig. 4-16.

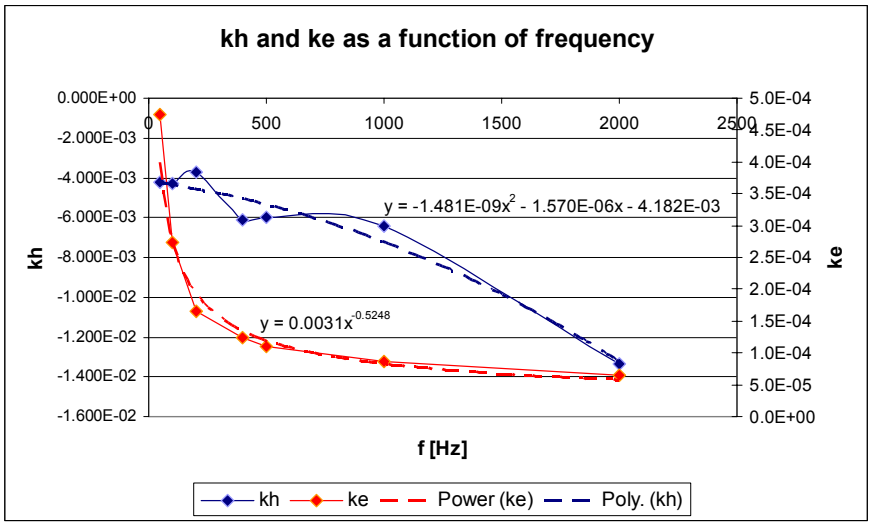

Fig. 4-16 Coefficients ke and kh in Steinmetz equation as a function of frequency

Knowing dependency of k_e and k_h on frequency allows performing calculations of iron loss numerically at various remagnetization frequencies and magnetic loadings. The actual algorithm analyses waveforms of magnetic flux density in x-,y- and z-direction at pre-defined loadpoints in terms of torque and speed, obtained at different parts of stator core:

- Tip of tooth
- Middle of toot
- Backiron-behind slot
- Backiron-behind tooth

Following Fig. 4-17 depicts Bx, By and Bz waveforms in the middle of tooth at 1300rpms and maximum power alongside with the same waveforms obtained in the backiron behind tooth for maximum power at maximum speed of 2800 rpms loadpoint. B_{MOD} waveform represents magnitude of flux density vector. These flux density profiles are outcome of Finite-Element Analysis, so that the stator segment with AC current loading adequate to the load is remagnetized by rotor magnets field at a given speed for one electrical period.

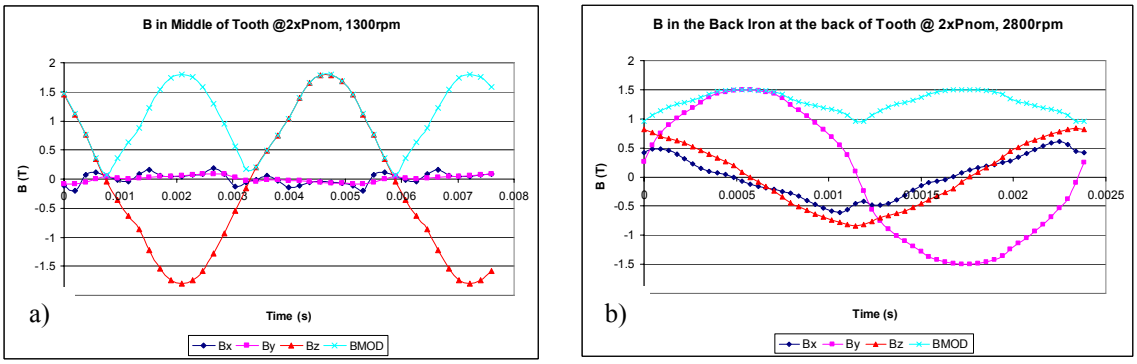

Fig. 4-17 Bx, By, Bz and Bmod wavefroms a) in the middle of stator tooth and b) in a backiron behind a stator tooth at defined loadpoints

Such waveforms are feasible input for harmonic analysis using Fourier series providing magnitude of each harmonic of B in x,y and z directions. Defining Fourier series as:

$$s(t) = \sum_{m=-\infty}^{+\infty} c_m \exp(jm\omega_1 t) \tag{4-38}$$

where $s(t)$ is analyzed harmonic signal, c_m is coefficient of the m-th harmonic and ω_1 is angular frequency of the carrier. The c_0 coefficient represents the DC component of the signal. For every $m > 0$ is valid that:

$$|c_m| = |c_{-m}| = \frac{1}{2} C_m ; \arg(c_m) = -\arg(c_{-m}) = \varphi_m \tag{4-39}$$

where C_m is magnitude and φ_m phase of the m-th harmonic component. The c_m coefficients may be obtained as:

$$c_m = \frac{1}{T} \int_{-T_1/2}^{T_1/2} s(t) \exp(-jm\omega_1 t) dt \tag{4-40}$$

where T represents period of the analyzed signal.

The outcome of the Fourier analysis gives understanding of what component of field at what magnitude remagnetize each part of the stator iron in x,y and z-direction. This allows feeding back such field components into Steinmetz equation for each loadpoint at torque vs speed map and therefore, obtain level of iron losses. Following Fig. 4-18 illustrates impact of a load torque on iron losses with consideration of higher harmonics of to 9th order. The increased magnetic loading in the airgap projects also into rise of peak flux density in electrical steel. Since MTPA control strategy, which partially imposes also d-axis current, is applied, the flux density wavefrom in a tooth, accordingly to Fig. 4-17a does not get significantly distorted in terms of unsymmetry of the waveform.

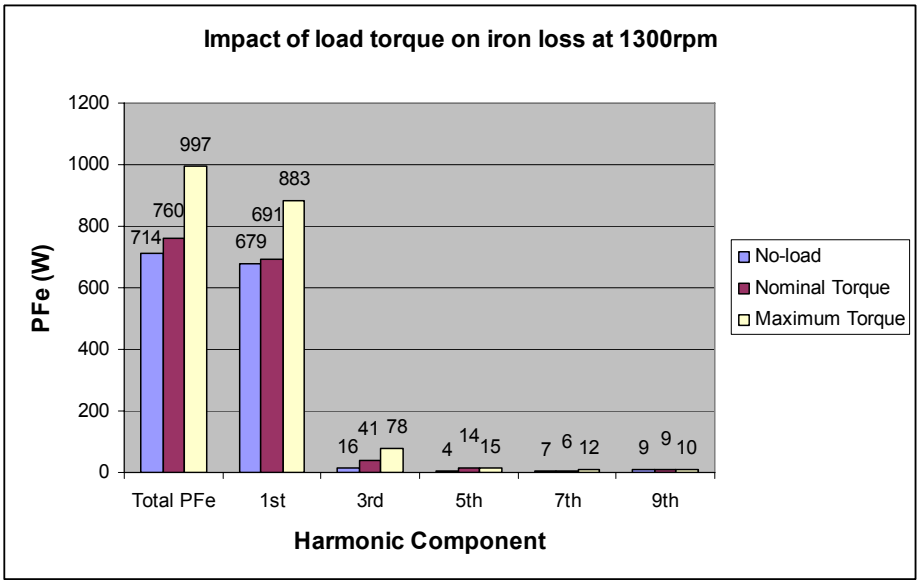

Fig. 4-18 Impact of load torque on harmonic components of iron losses

An other case worth of investigating is no-load operation at maximum speed of 2800rpms. One may distinct two different cases, the machine may either spin without power electronic active, let's assign abbreviation "No-load" to this operational mode, or power electronics may actively perform field weakening, with assigning "Idling"

expression to such status. Operation in "Idling" mode assumes that the machine does not deliver any torque at the shaft, and compensates in terms of its electromagnetic torque for losses only. Fig. 4-19 quantifies difference in iron losses in between "No-load" and "Idling" operation.

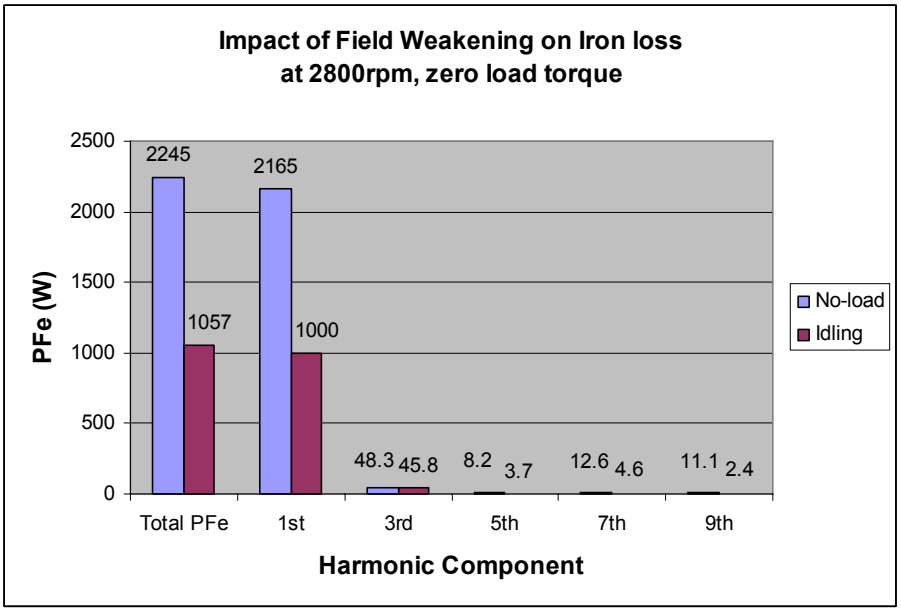

Fig. 4-19 Impact of active field weakening on iron losses at maximum speed

The reason for significant reduction of iron losses in "Idling" operation is in reduction of flux density in the airgap throughout imposing negative d-axis current. For illustration of this phenomena, Fig. 4-20 shows throughout FEA snapshot magnetic loading in the airgap in "Idling" operation, therefore full field weakening. The peak flux density in the airgap then reaches 0.869T.

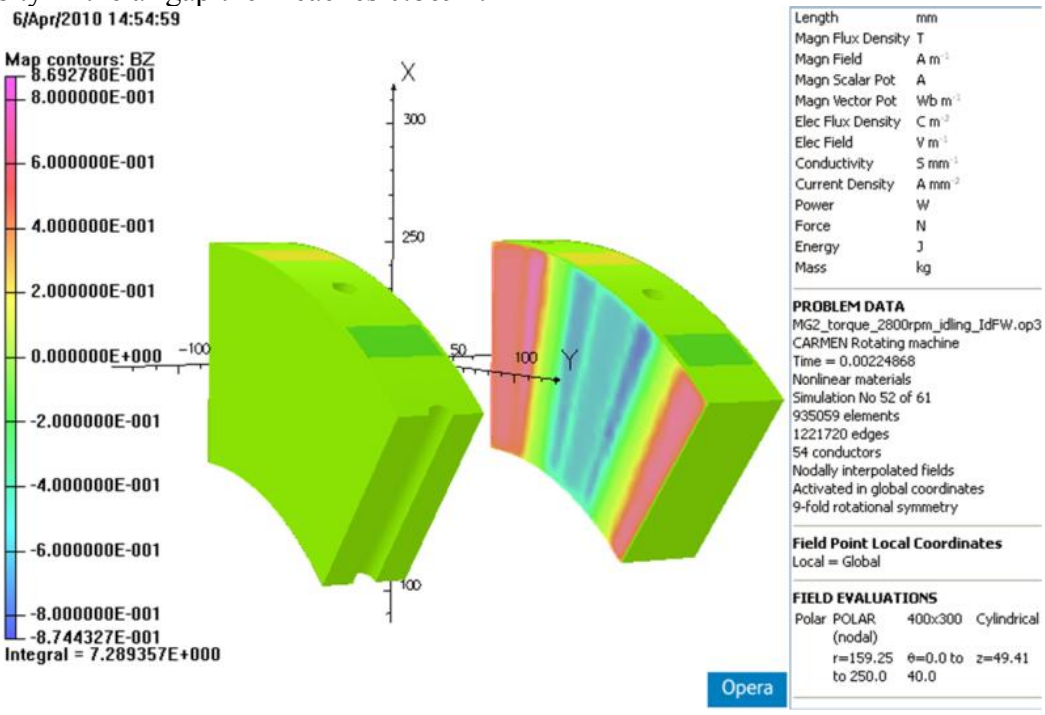

Fig. 4-20 Magnetic loading in the airgap in "Idling" operation

Hypothetically, a case with reversing the current angle so that the d-axis current would be increasing the magnetic laoding in the airgap in "Flux-up" mode may occur.

To illustrate level of influence of such phenomena, a peak flux density in the airgap would rise up to 0.946T according to FEA snapshot shown in Fig. 4-21.

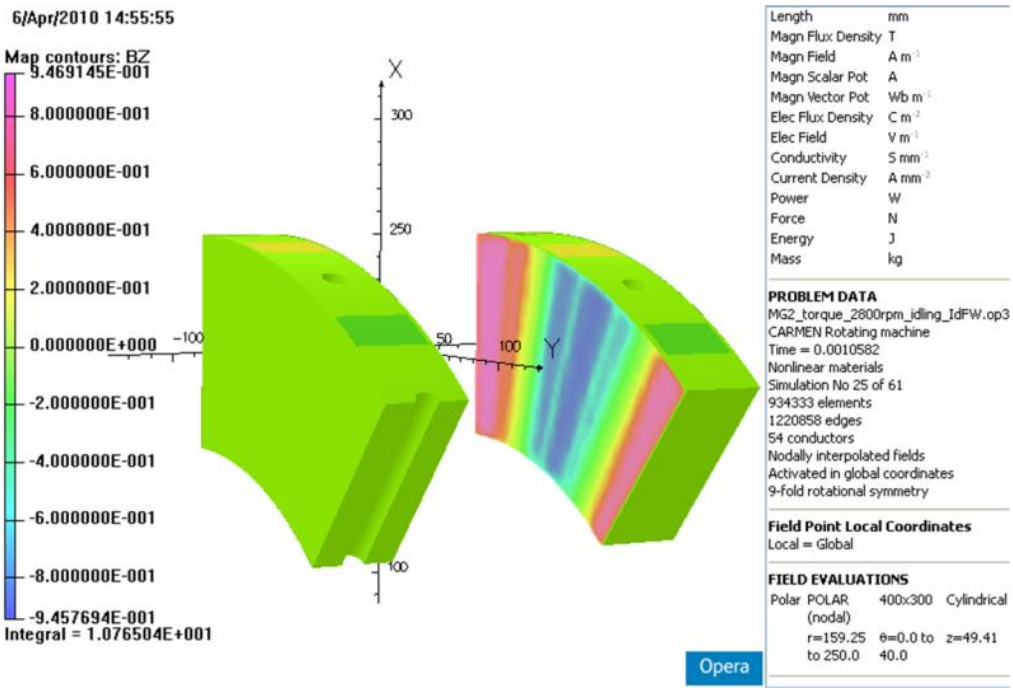

Fig. 4-21 Magnetic loading in the airgap at maximum speed in "Flux-up" operation

Actual difference in total iron losses in "N-load" mode across wide speed range vs. "Idling" operation at maximum speed shows Fig. 4-22 below.

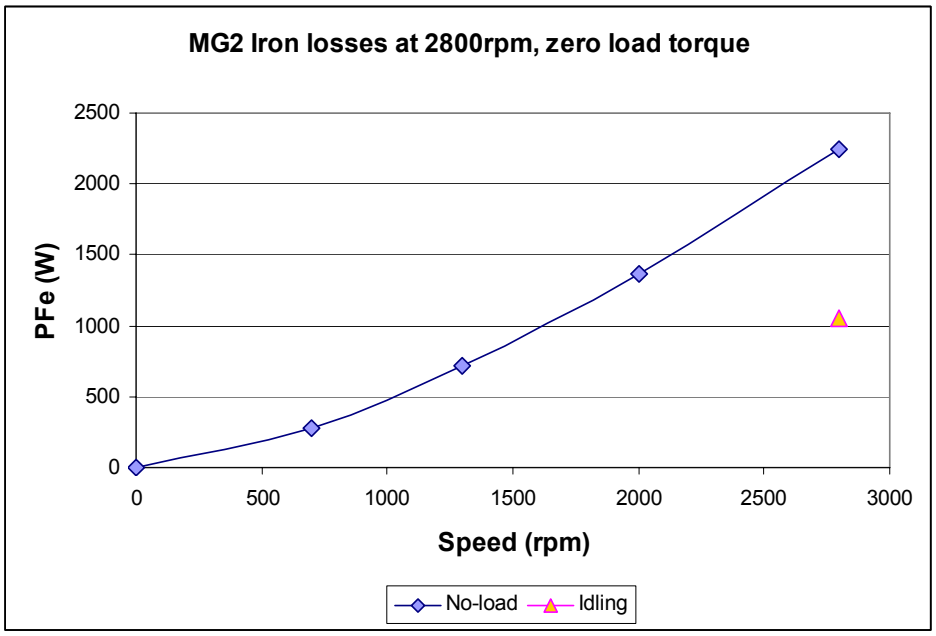

Fig. 4-22 Total No-load iron losses across speed range in comparison to iron losses in "Idling" at maximum speed of 2800rpms

Analysis of flux density waveforms at number of loadpoints allows creating a grid of loadpoints with FEA-calculated iron losses. Since the involved FEA is time consuming bit of the analysis, it is appropriate to increase density of loadpoints with estimated iron losses by interpolation, in this particular case by adopting cubic spline algorithm. Fig. 4-23 illustrates such iron loss map, exactly overlapping an efficiency map.

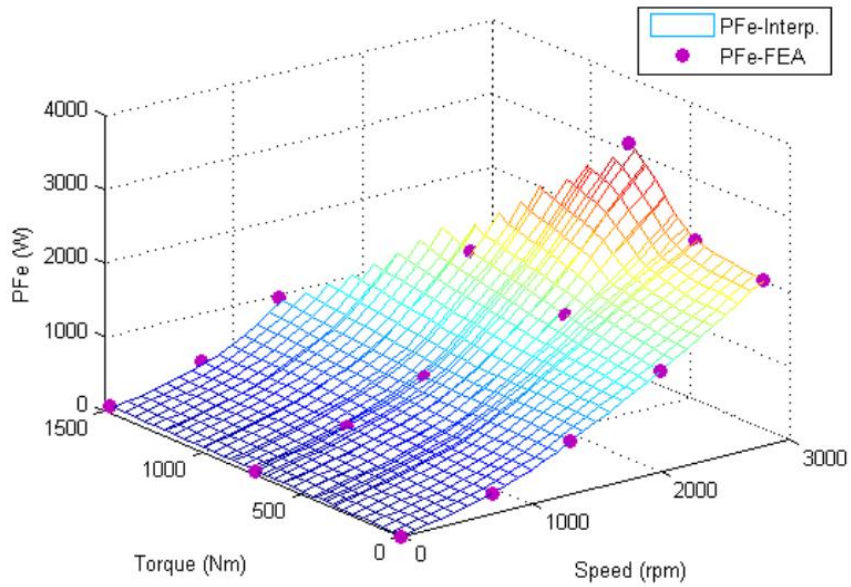

Fig. 4-23 Iron loss map as an outcome of the iron loss model, exactly overlapping an efficiency map. Violet points represent loadpoints analyzed by FEA.

The iron loss map may be stored as two-dimensional look up table, and therefore, is feasible for generating efficiency maps or for system level simulation purposes.

4.4. Finite – Element Analysis of Spoke Axial Flux Machine

The numerical modeling of electric machines, in particular Finite element analysis, enhanced level of understanding the electric machines. FEA helps to predict electromagnetic fields within the machine, and estimation of its parameters and performance. FEA appears to be particularly advantageous for nonlinear magnetic circuits, such as Spoke-Axial Flux machine, when it may help to calibrate analytical tools as well.

4.4.1. Estimation of leakage flux

Design of the Spoke-AFM based on equivalent-reluctance circuit assesses leakage flux within the machine, according to Fig. 4-2 mainly due to main bridges keeping magnets in the rotor structure. However, more detailed look at distribution of magnetic field within the machine advices, that there are actually additional leakage fluxpath further reducing amount of flux crossing the airgap alongside the main ones:

1. Bridge holding the magnet – airgap side
2. Bridge holding the magnet – back side
3. Air behind the rotor plate
4. Single turn of unslotted lamination at rotor inner diameter
5. Stainless steel hub at inner diameter
6. Stainless steel retaining ring
7. Construction-steel made sensing sing on top one of the rotor plates

These cases are depicted in two-dimensional cuts through a rotor plate, and annotated in terms of numbering on following Fig. 4-24.

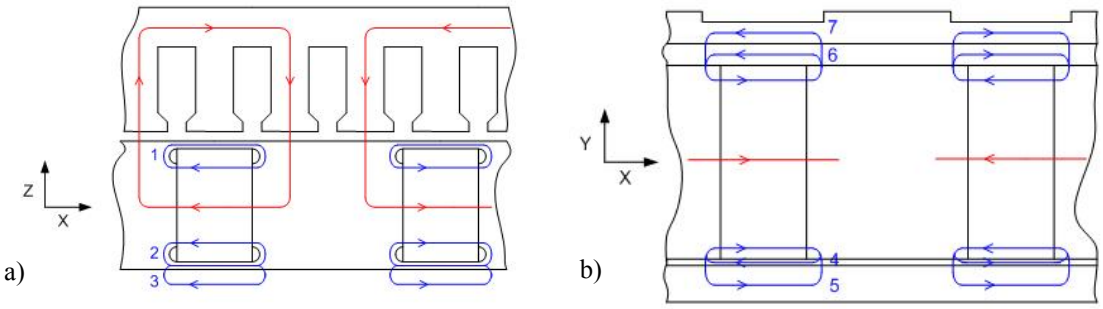

Fig. 4-24 2D-cuts through the rotor plate a) in XZ plane and b) in XY plane depicting leakage fluxpaths

The FEA snapshot in Fig. 4-25 below helps to visualize leakage fluxpath through single turn of unslotted lamination at inner diameter of the rotor corepack, in this particular case by vectors of magnetic flux density.

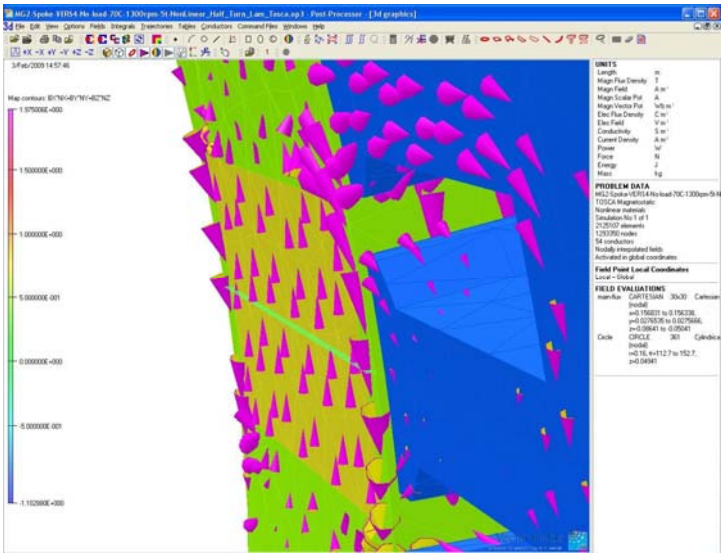

Fig. 4-25 Leakage fluxpath through single turn of unslotted lamination

Analogically Fig. 4-26 depicts leakage fluxpath through the air behind a rotor plate. Extra leakage flux may appear in this location sice permeability of bridges holding magnets as a paralel leakage fluxpath is already low due to their saturation.

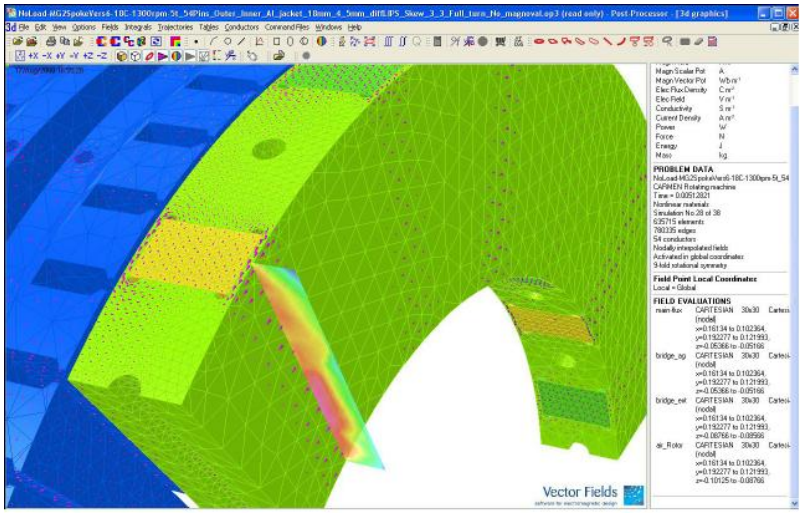

Fig. 4-26 Leakage fluxpath in the air behind the rotor core.

In a case of Fig. 4-25, the single unslotted turn of lamination in fact creates a "magnetic short" for the bottom portion of the magnet. Fig. 4-26 shows a radial patch in the air behind the rotor plate, capturing stray flux avoiding saturated bridges, which permeability is close to unity.

The following Tab. 4-2 assigns quantity of leakage flux for each fluxpath as described above for the 18-pole design of Spoke-AFM:

Tab. 4-2 Leakage flux through stray fluxpaths of the rotor

#	Description	Leakage Flux (Wb)
1	Bridge-airgap side	3.47E-04
2	Bridge-back side	3.66E-04
3	Air behind rotor plate	1.25E-04
4	A turn of unslotted lamination	3.55E-05
5	Stainless steel hub at ID	1.54E-04
6	Stainless steel retaining ring	3.15E-05
7	Sensing ring	1.63E-04

The leakage flux data presented in Tab. 4-2 helps to calibrate the analytical design tools so that further designs would require lower level of FEA work involved. The main peak airgap flux per pole reaches 3.885mWb for comparison to the level leakage flux.

4.4.2. Magnet flux linkage and no-load voltage

A magnet flux linking a coil is available from no-load solution, in particular magnetic vector potential A_z [52]:

$$\nabla \times \quad = \tag{4-41}$$

Assuming that an oriented curve l represents a loop of a coil, flux is given as:

$$\phi = \oint_{l} \quad dl \tag{4-42}$$

The line integral of the vector potential around a close path is equal to the magnetic flux linking that path. Labeling the "go" side of a coil as "1" and the return side as "2", the flux linking the coil is a difference between the magnetic vector potential of "1" and "2":

$$\phi = A_1 - A_2 \tag{4-43}$$

One may consider the option of reading the magnetic vector potential at center point of the coil, but it is more convenient to average the value of A over a slot region:

$$A_{avg} = \frac{1}{S} \iint_{S} \quad d \tag{4-44}$$

Then the magnet flux linkage, depending on the winding configuration, is given as:

$$\Psi_{PM} = 2 p_p l_r \frac{n_q}{n_{pp}} \sum_{q=1}^{Q/2pp} k_{jq} A_{avg} \tag{4-45}$$

where n_q is number of conductors in a slot, n_{pp} indicates number of parallel paths of the winding, $Q/2p_p$ is the number of slots per pole and k_{jq} might take the values of $\pm 1 or \pm 0.5$ depending on the winding configuration.

Considering Faraday's law – the integral of electric field **E** along a prescribed path *l* is equal to decrease of magnetic flux with time:

$$\int_l dl = -\frac{d}{dt} \tag{4-46}$$

The induced voltage may be obtained numerically from Equ (4-46) for a given timestep ΔT as illustrates Fig. 4-27:

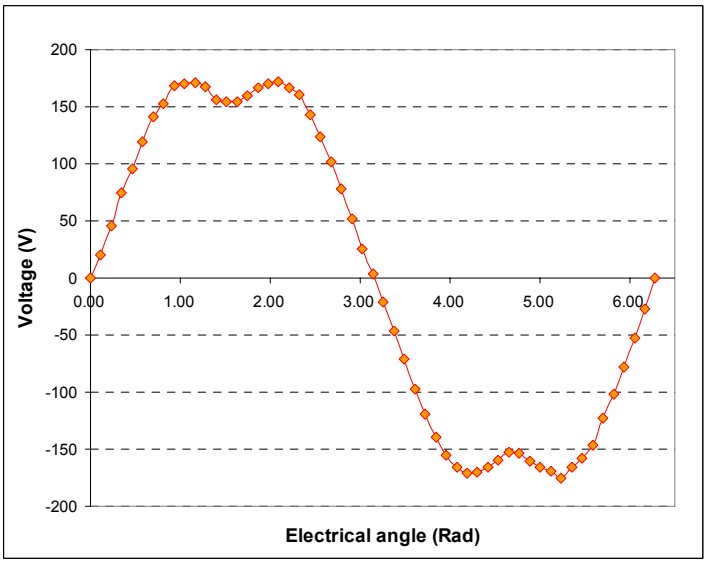

Fig. 4-27 No-load voltage waveform at 1300rpm for zero offset angle between rotor plates and permanent magnets at 70degC temperature

The first outlook on a EMF waveform of line-to-neutral voltage at base speed indicates significant presence of 3rd harmonic component. The higher harmonic of induced voltage lead toward unfavourable side effects such as possible torque ripple, noise or increased losses, and therefore should be reduced.

4.4.3. Offset angle analysis and THD reduction

The waveform of induced voltage usually contains higher harmonics, which should be ideally suppressed. There are several ways how to eliminate higher harmonics in EMF waveform, and some of them are applicable to design of MG2. Frequently employed technique is to skew stator slots, or magnets on the rotor side. The option of adjusting shape of magnets from their regular block shape is not applicable due to the rotor manufacturing process. However, the design of the rotor subassembly offers introduction of an offset angle between rotor plates, so that they are not magnetically aligned anymore. Thus, waveforms of the induced voltage induced in a coil due to each individual rotor plate do not exactly overlap, and shape of the final waveform may be optimized.

A way of quantifying higher harmonic content in induced voltage is to calculate Total Harmonic Distortion (THD), defined as:

$$THD = \frac{\sqrt{V_3^2 + V_5^2 + V_7^2 + V_9^2 + V_{11}^2 + \ldots + V_n^2}}{V_1} \tag{4-47}$$

THD according to definition by Equ (4-47) includes all odd harmonics of EMF greater or equal to third in terms of their order. However, the third harmonic and its multiplicands will have no impact to the behavior of the machine due to star-connection of the machine's winding. Therefore, we may introduce modified $THD_{,mod}$ excluding third and its multiplicands so that

$$THD_{,\mathrm{mod}} = \frac{\sqrt{V_5^2 + V_7^2 + V_{11}^2 + \ldots + V_n^2}}{V_1} \tag{4-48}$$

According to [43], higher harmonics included in $THD_{,mod}$ may cause torque ripple effect to the machine. The 5th, 11th etc… harmonic in abc reference frame projects as 6th, and 12th etc… harmonic in dq0 reference creating accordingly to their order of torque ripple with respect to the rotor mechanical position ϑ_r:

$$\begin{aligned} T_{e,r}(\vartheta_r) &= i_d\left(\Psi_{d,6}\sin(6\vartheta_r) + \Psi_{d,12}\sin(12\vartheta_r)\right) + \ldots \\ &+ i_q\left(\Psi_{q,6}\sin(6\vartheta_r) + \Psi_{q,12}\sin(12\vartheta_r)\right) \end{aligned} \tag{4-49}$$

Assuming Id=0 control strategy, Equ (4-49) simplifies into:

$$T_{e,r,\max} = i_q\left(\Psi_{q,6} + \Psi_{q,12}\right) \tag{4-50}$$

Considering the EMF waveform of Spoke-AFM with zero offset angle in Fig. 4-27, the total content of higher order of harmonic is summarized in Tab. 4-3

Tab. 4-3 Content of higher harmonic for machine with zero offset angle

Harmonic Order	1st	3rd	5th	7th	9th	11th	13th	15th	17th	19th	21st	23rd	25th	27th
Peak Voltage (V)	187.36	22.09	9.59	1.3	0.84	0.41	0.46	0.36	0.61	0.34	0.72	0.51	0.08	0.54
Ratio against 1st		11.79%	5.12%	0.70%	0.45%	0.22%	0.24%	0.19%	0.33%	0.18%	0.38%	0.27%	0.04%	0.29%

A mechanical layout of the machine offers effective way of reducing THD of the EMF. Rotor plates may be angularly displaced by given offset angle in terms of their magnetic d-axis so that their airgap flux density waveforms do not exactly overlap. That means the airgap flux density in one airgap is lagging behind the waveform in the other airgap. Accordingly to the displacement of field waveforms is the same happening to the EMF waveform so that one active side of a winding turn contributes by time-wise displaced EMF than the other. This basically allows to control shape of the EMF waveform. Imagine that the waveform presented on Fig. 4-27 is divided by two. Such waveforms with half of the total magnitude may be displaced to each other and summed up eventually for a given range of offset angle. Such shifting of relative positions of waveforms to each other has therefore an impact on content of higher harmonics, as illustrates Fig. 4-28. The offset angle varies up to angle corresponding to one slot span.

As is illustrated on Fig. 4-28 a), the 3rd harmonic drops down with growing offset angle. However, considering the 5th harmonic as a most harmful because of torque ripple issue, the targeted offset angle should most likely be at 3.3deg mechanical, therefore half of a slot span. Such angle reduces at the most the $THD_{,mod}$ as well

according to Fig. 4-28 b). The same figure illustrates the main drawback in terms of 1st harmonic reduction too.

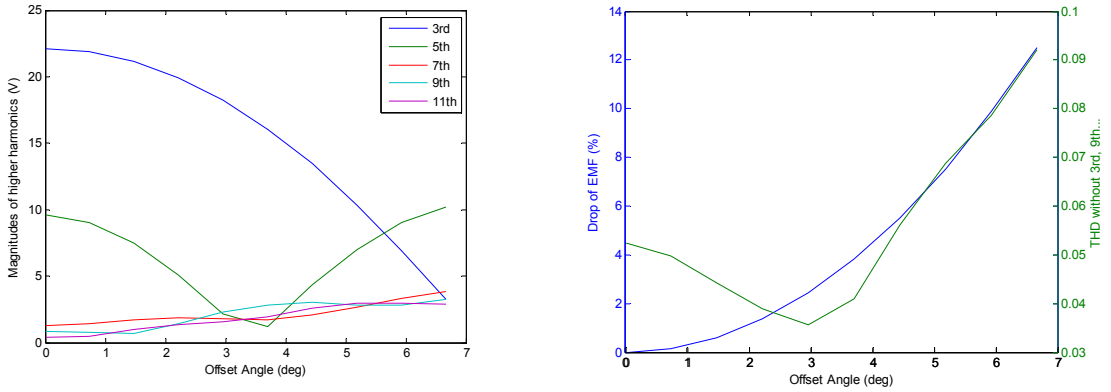

Fig. 4-28 a) Dependency of magnitude of higher harmonic on offset angle and b) drop of 1st harmonic and THD,mod as a function of offset angle

Actual EMF waveform for 3.3.deg offset angle is depicted on Fig. 4-29 below:

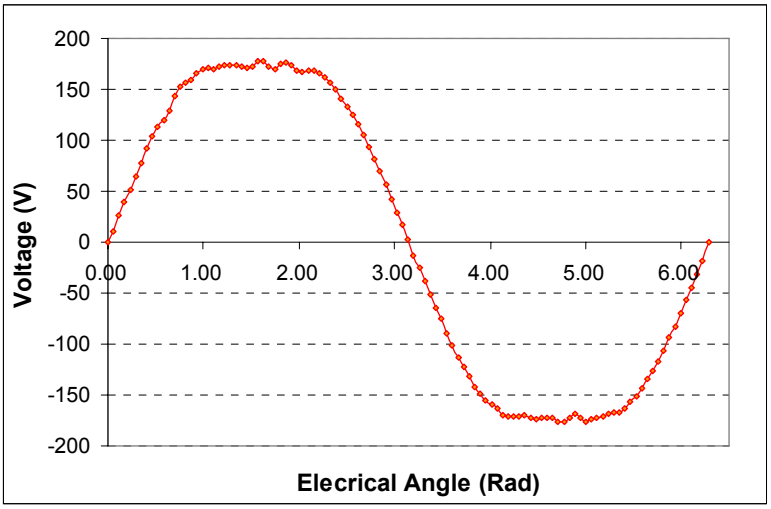

Fig. 4-29 EMF waveform at 1300rpm for 3.3.deg offset angle between rotor plates

The impact of adjusted offset angle for 3.3deg case on higher harmonic components of EMF quantifies Tab. 4-4:

Tab. 4-4 Harmonic components of EMF waveform at 3.3deg offset angle

Harmonic Order	1st	3rd	5th	7th	9th	11th	13th	15th	17th	19th	21st	23rd	25th	27th
Peak Voltage (V)	189.29	17.34	2.86	0.25	0.86	0.13	0.21	0.51	0.2	0.18	0.48	0.33	0.26	0.17
Ratio against 1st		9.16%	**1.51%**	0.13%	0.46%	0.07%	0.11%	0.27%	0.11%	0.09%	0.25%	0.18%	0.14%	0.09%

The 5th harmonic as a result of offset angle adjustment dropped down from 5.12% to 1.51% of the 1st harmonic. Outcomes of harmonic content reduction summarize the barchart in Fig. 4-30:

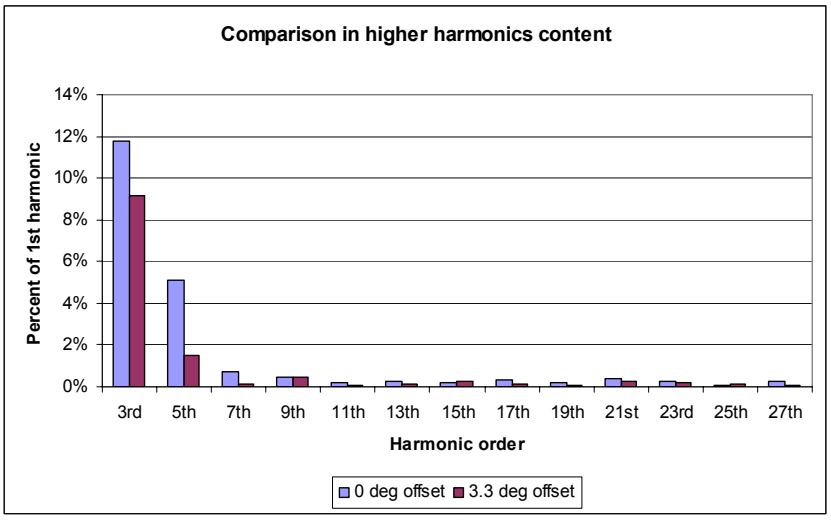

Fig. 4-30 Direct comparison of higher harmonics for zero and 3.3 deg offset angles

In terms of impact on torque ripple, by adjusting the offset angle to 3.3deg the magnitude of 6th torque harmonic dropped from $20.7Nm$ to $6.7Nm$ at maximum load torque.

4.4.4. Torque production

A straightforward method of determining torque production using FEA is Maxwell stress tensor method. Electromagnetic torque can be then determined by the line integral along enclosed path *l*.

$$T = \frac{l_r}{\mu}\oint_l B_n B_t r \cdot dl \tag{4-51}$$

where B_n is normal and B_t tangential component of magnetic flux density in the airgap at radius *r*. The actual analysis estimates profile of torque production versus different current angle β. Thus, actual peak torque production versus distribution of stator current pattern may be determined. The computational setup may follow rotating motion analysis either with DC-current fed stator winding and rotor moving at required, most likely, base speed. The other option with results presented at Fig. 4-31 assumes stator winding fed by AC current waveform with electrical frequency corresponding to base speed, and locked rotor.

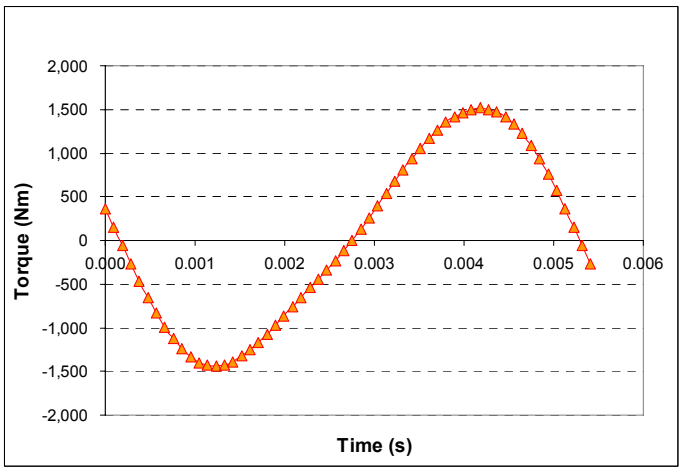

Fig. 4-31 Torque production of MG2 at base frequency and maximum current of 480Arms

Similar analysis may be performed at maximum speed in order to verify that the machine is able to deliver for predicted current the maximum power. Meanwhile, such analysis provides corresponding current angle as well, helping to verify field weakening performance of the machine.

4.4.5. Cogging torque

There are two major components creating pulsating torques in the electrical machine. Alongside with previously estimated torque ripple depending on the level of stator current, cogging torque is determined mainly due to geometry of stator slots, and is thus almost independent of the load. A source of cogging torque is in interaction of the rotor magnetic field and stator teeth, where slot opening causes sudden change of magnetic energy W_m. Cogging torque may increase with load of the machine once tips of stator teeth saturate due to armature reaction field, causing effectively increase of slot opening due to drop of relative permeability of the stator steel. The cogging torque obviously does not apply to slotless machines.

Cogging torque T_{cog} may be expressed as variation of magnetic energy versus rotor position ϑ for a constant stator current.

$$T_{cog} = \left(\frac{dW_m}{d\vartheta} \right)_{i=const} \tag{4-52a}$$

where magnetic energy in the airgap is obtained by volume integration from airgap flux density:

$$W_m = \frac{1}{2\mu_0} \int_V B_g^2 dV \tag{4-52b}$$

Following Fig. 4-32 depicts cogging torque waveform as a function of the rotor mechanical angle obtained by Finite-element no-load analysis. The cogging torque waveform may be characterized by periodicity of 3.3deg mechanical due to offset angle between rotor plates of 3.3deg. Application of the offset angle doubled the frequency of cogging torque, as a machine with zero offset angle would produce cogging torque waveform corresponding to slot span of 6.6deg. Moreover, application of the offset angle helps reducing the magnitude of cogging torque since variation of magnetic energy due to slotting happens not in the same instant for each airgap.

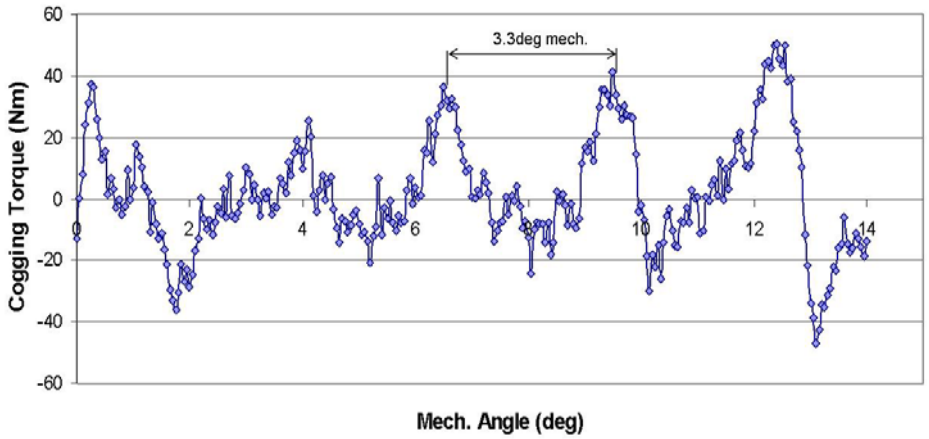

Fig. 4-32 Profile of cogging torque showing periodicity of its waveform at 3.3deg mechanical

According to Fig. 4-32, the absolute value of magnitude of the cogging torque is up to 50Nm. Cogging torque is thus proportionally at 3.4% of peak torque production of 1470Nm.

4.4.6. Inductances

FEA focused on calculation of inductances is limited to flux variance method due to nonlinear character of the magnetic circuit. Permanent magnets of the machine need to be magnetized for a purpose of the analysis so that bridges holding them in the rotor structure are saturated, as this is the default case for the machine at whatever operational conditions. The actual flux variation method determines inductance based on change of flux linkage with current $\Delta\psi / \Delta I$. Therefore, it is valid to assign for d-axis inductance

$$L_d = \frac{\Psi_d - \Psi_{PM}}{I_d} \tag{4-53}$$

considering that d-axis flux linkage Ψ_d includes contribution of armature reaction flux as well as flux due to permanent magnets. The q-axis inductance may be expressed analogically as:

$$L_q = \frac{\Psi_q}{I_q} \tag{4-54}$$

The actual postprocessing of FEA follows the same procedure as described by Equ (4-41) – (4.45) for obtaining the magnet flux linkage. A profile of inductances as a function of current depicts Fig. 4-33:

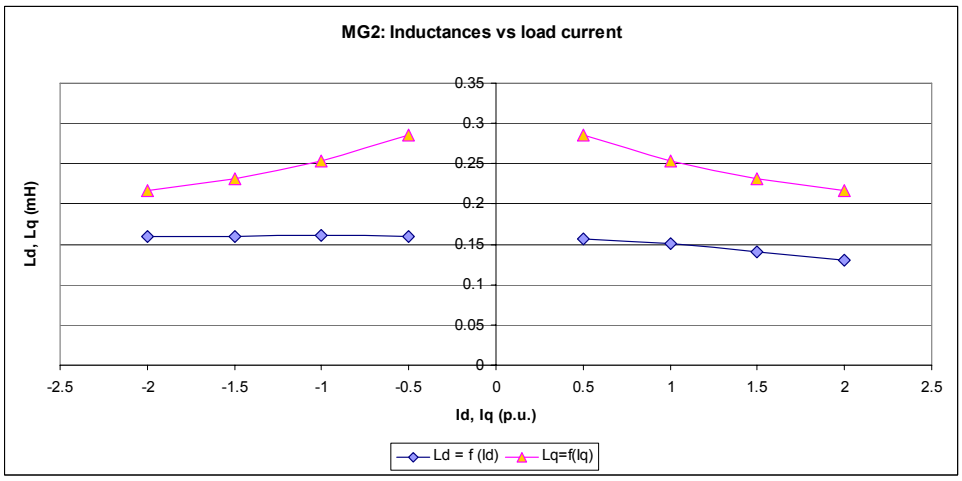

Fig. 4-33 Profile of d- and q-axis inductances for both positive and negative current pattern alignments up to maximum 2pu current of 480Arms

The q-axis inductance exceeds in terms of its size the d-axis one supporting the assumption of inverse-saliency of MG2 design, though there is a clear impact of saturation. The d-axis inductance saturates only for fluxing-up operation, when positive d-axis current effectively increases the first harmonic of magnetic flux density in the airgap, causing saturation of the stator iron. However, the d-axis inductance is immune to saturation for negative d-axis current pattern since its effect is de-saturation of the iron core. Hence, d-axis inductance may be assumed as constant due to the machine will

not be operated in fluxing-up operation. Following Tab. 4-5 summarizes numerically profiles of d- and q- axis inductances:

Tab. 4-5 d- and q- axis inductances as a function of current

Id (p.u.)	-2	-1.5	-1	-0.5	0.5	1	1.5	2
Iq (p.u.)	-2	-1.5	-1	-0.5	0.5	1	1.5	2
Ld (mH)	0.160	0.160	0.160	0.064	0.157	0.150	0.141	0.131
Lq (mH)	0.217	0.231	0.253	0.286	0.286	0.253	0.231	0.217

Impact of q-axis inductance saturation needs to be addressed during control design since it may affect optimum split of current components into d- and q- axis for MTPA or field weakening control strategies.

4.5. Axial forces in MG2

One of the inputs for MG2 design is the nominal airgap thickness. However, there are several reasons why the nominal airgap may not not maintained. Variation because of manufacturing and assembly tolerances is among the biggest contributors. According to provided Dimensional Variation Analysis, the total nominal airgap variation because of manufacturing and assembly processes is $\pm$0.59mm, out of $\pm$0.328mm is contribution caused by pure axial displacements and $\pm$0.262mm is due to angular displacement in bearings. These inputs from mechanical design side identify a case for analysis of axial forces in the machine in the following cases:

- axial forces when both rotor plates are exactly aligned
- a case when rotor plates are axially shifted, but airgaps are still parallel
- angular displacement of rotor plates versus stator causing unparallel, tilted airgaps
- a combined case of axial shift and angular misalignment.

Any misalignment of airgaps creates misbalance between forces acting on each of the rotor plates. Shorter is the airgap, greater are the axial forces over a rotor plate. This creates a positive feedback loop, so that once the rotor plates are misaligned versus the stator, the effect tends to amplify. Unless this phenomenon is adequately addressed in mechanical design, any axial flux machine is faced to a risk of a collision of rotating and stationary parts during its operation.

4.5.1. Axial forces at uniform airgaps

Attraction force in the airgap may be determined by applying virtual work method as a variation of stored magnetic energy W_m with regards to variation of the airgap length in z-direction:

$$F_z = \frac{dW_m}{dz} \approx \frac{\Delta W_m}{\Delta z} \tag{4-55}$$

An alternative approach is to estimate attraction force through distribution of magnetic flux density in the airgap:

$$F_z = \frac{1}{2}\frac{B_g^2}{\mu_0} S_{rp} \tag{4-56}$$

where S_{rp} is effectively rotor place surface area.

Both approaches allow applying FEA. The option of using distribution of magnetic flux density in the airgap benefits out of already available FEA models directly providing solution. However, there are several ways how to perform actual calculations of forces numerically. The airgap area may be discretized in terms of angle, so that the force F_z is calculated from inner up to outer diameter with increment Δr per fixed angular segment $\Delta\vartheta$:

$$F_{z,\vartheta} = \frac{1}{2}\frac{1}{\mu_0} \sum_{i=1}^{i=(OD-ID)/\Delta r} \left[\pi \left(\left(\frac{ID}{2} + (i+1)\Delta r \right)^2 - \left(\frac{ID}{2} + i\Delta r \right)^2 \right) \frac{\Delta\vartheta}{2\pi} \cdot B^2{}_{g,ri} \right] \tag{4-57}$$

where $B_{g,ri}$ is airgap flux density at particular radius r according to increment count i. This allows determining variation of force with rotor angle, and therefore prediction of loading of specific rotor parts by unbalanced forces as is shown in Fig. 4-34. Such profile of force vs. angle provides therefore necessary inputs for the rotor structural design.

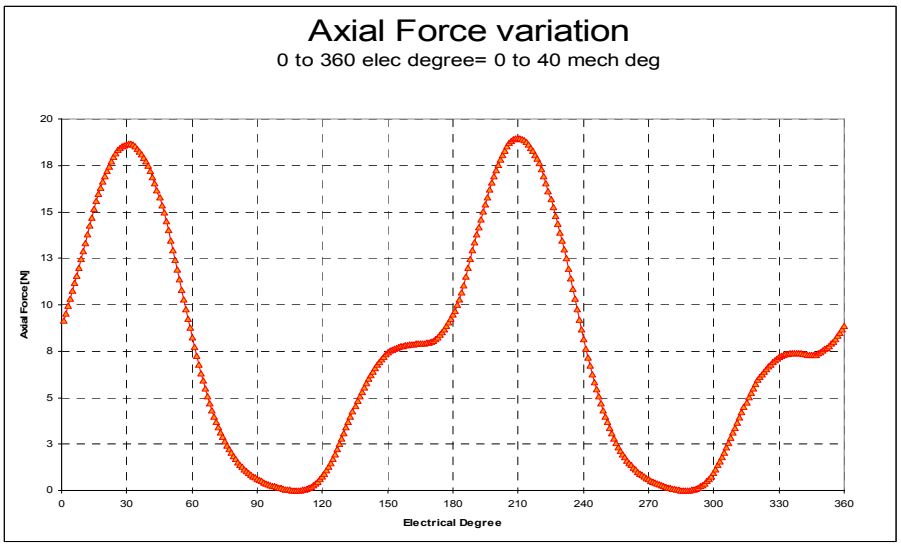

Fig. 4-34: Profile of axial forces considering angular segmentization

Peaks of axial force according to Fig. 4-34 at angle of 30deg and 210deg electrical aligns with the d-axis of the rotor plate. The presented profile of axial force versus angle corresponds to the maximum power/maximum speed load case.

A different way of analyzing a profile of axial forces is to perform computation per entire airgap circumference at given radius r with considering a radius increment Δr:

$$F_{z,r} = \frac{1}{2}\frac{1}{\mu_0} \sum_{i=1}^{i=2\pi/\Delta\vartheta} \left[\pi \left((r+\Delta r)^2 - r^2 \right) \cdot \left((i+1)\Delta\vartheta - i\Delta\vartheta \right) \cdot B^2{}_{g,\vartheta i} \right] \tag{4-58}$$

Fig. 4-35 gives indication, how axial forces varies with load and a diameter as a parameter.

The plot of forces vs diameter in Fig. 4-35 was obtained once again for maximum power/maximum speed loadcase. The plot indicates that the rotor plate might be subject of umbrella-type deflection due to the force increases with diameter.

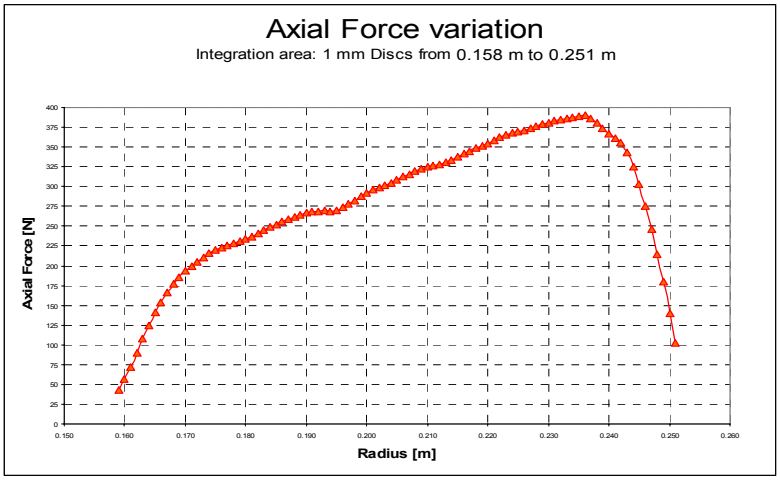

Fig. 4-35 Profile of axial forces considering radial segmentization

In terms of total axial force per a plate, two different load cases were investigated. The total axial forces per a plate at maximum torque/base speed loadcase are estimated to be 21.8kN, whereas forces at maximum power/maximum speed loadcase are predicted at 25.8kN. Therefore, the maximum power/maximum speed loadcase will be considered for further presented analyses

4.5.2. Pure axial movement of rotor plates

This case of axial forces investigates pure axial shift of rotor plates so that both rotor plates are still parallel with regards to the stator assembly. The pure axial shift may occur due to tolerancing issues on component side or during assembly process.

A process of calculating forces for pure axial shift is analogical to the one described in previous section 4.5.1. An increase of airgap thickness on one side of stator means in a case of this particular analysis a proportional decrease of the airgap thickness on the other side. Following Fig. 4-36 shows dependency of axial forces on axial move.

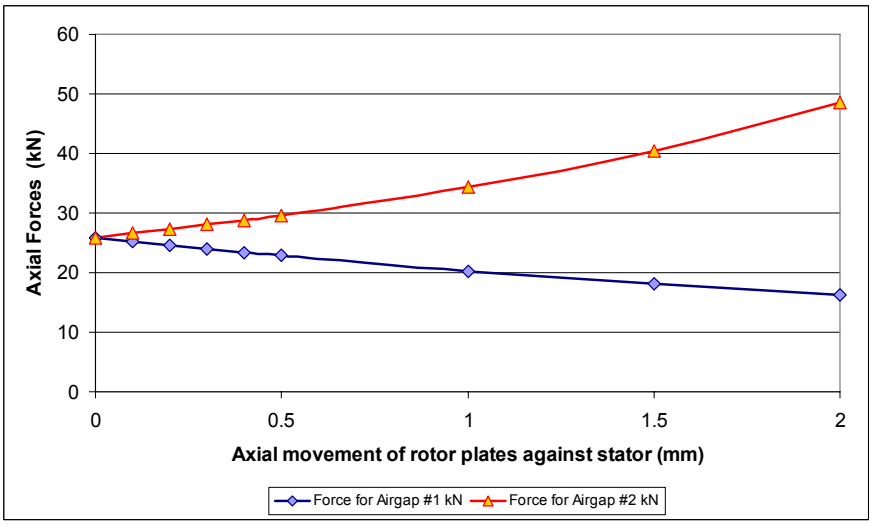

Fig. 4-36 Variation of axial forces for each airgap for pure axial shift of rotor plates

As the misalignment progresses, the total force rises for the loadcase maximum power/maximum speed from 25.8kN up 48.6kN, when one of the rotor plates is clamped to the stator core. This case may occur during assembly or handling of the machine. Therefore, design of assembly and handling tools required for those processes needs to assume as a worst case scenario, when one of the rotor plates is clamped to the stator. A profile of axial forces for pure axial shift case as depicted on Fig. 4-36 will vary depending on selected loadpoint.

4.5.3. Tilting of rotor plates

Design of the selected double-angular bearing allows angular displacement of up to 0.0566deg. That means, the rotor plates with regards to stator are no longer co-axial causing non-parallel alignment of airgaps. Assuming that tilting caused displacement of rotors at their outer diameter of Δz, the airgap thickness g_z might be redefined as $g_z \pm \Delta z$. Non-uniformity of the airgap causes discrepancy of the flux density waveform in the airgap. If the airgap thickness at 0deg mechanical position is $g_z + \Delta z$, then the airgap thickness at the opposite rotor plate position at 180deg must be $g_z - \Delta z$. The magnitude of airgap flux density waveform must change inverse-proportionally, as is illustrated on Fig. 4-37:

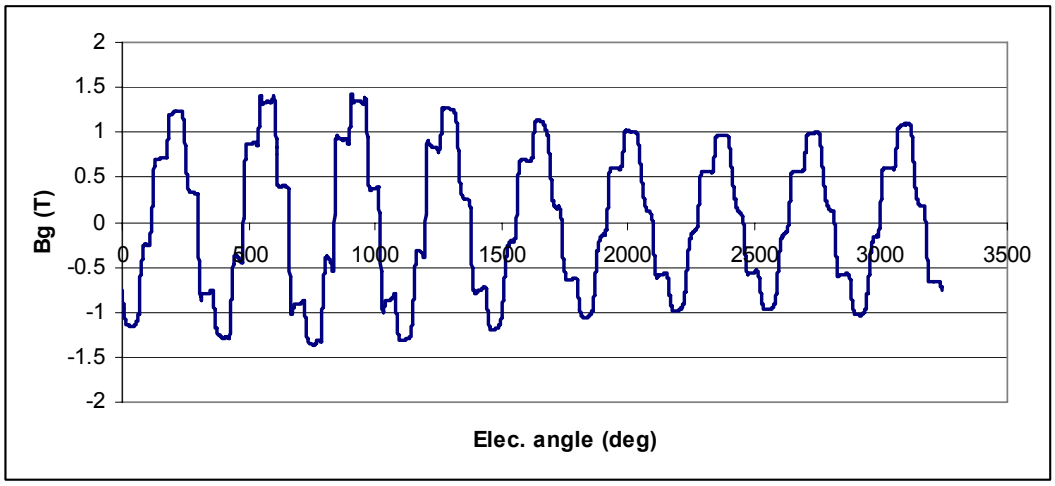

Fig. 4-37 Bg waveform at 240mm diameter though the middle of the airgap around entire airgap circumference

The waveform depicted on Fig. 4-37 assumes tilting case so that $\Delta z = 1mm$ at maximum power/maximum speed load case. Peaks of airgap flux density may vary by as much as 1.41T at 598deg electrical versus -0.97T at 2218deg, therefore at the opposite side of the rotor plate.

Distribution of axial force over a rotor plate varies accordingly to the profile of airgap flux density as shown in Fig. 4-37. A linearized map of axial force for the same loadcase and $\Delta z = 1mm$ according for Fig. 4-37 depicts Fig. 4-38.

Calculation of forces as shown in Fig. 4-38 considers discretization of the rotor plate surface by a grid defined angularly by one degree electrical and radially by one millimeter. Each of such incremental areas $S_{r,\vartheta}$ contributes adequately to the total force per rotor plate. In terms of actual airgap thickness, one geometrical half of the rotor plate forces, once the rotor plate is tilted, the airgap to be physically shorter, and the other half longer than nominal.

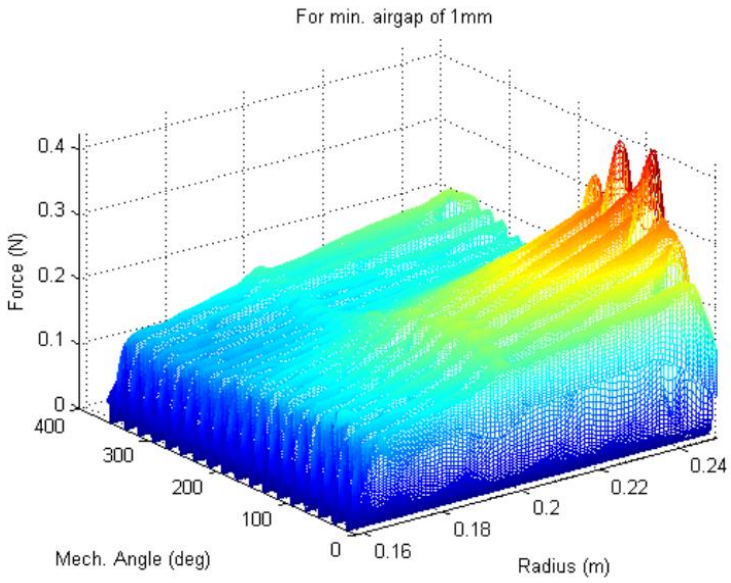

Fig. 4-38 Linearized map of axial forces for tilted rotor plates

Subtracting axial force according to Fig. 4-38 developed by incremental area $S_{r,\vartheta}$ on the side of the rotor plate with longer airgap from axial force developed at area displaced by 180deg mechanical $S_{r,\vartheta+\pi}$, but defined by the same set of radiuses, will indicate difference in force per two counter-located areas:

$$\Delta F = F(S_{r,\vartheta+\pi}) - F(S_{r,\vartheta}) \tag{4-59}$$

and hence incremental momentum ΔM acting at radius r in a direction of tilting:

$$\Delta M = \left(F(S_{r,\vartheta+\pi}) - F(S_{r,\vartheta})\right) \cdot r \tag{4-60}$$

Performing such calculation per a rotor plate provides a map of incremental moments, plotted against a half of a rotor plate due to applied subtraction of forces as seen by half of a rotor plate:

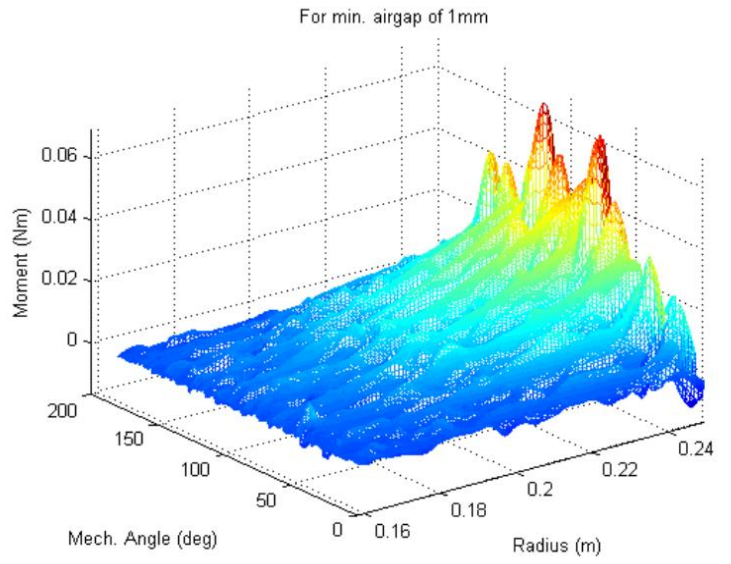

Fig. 4-39 Incremental moments per one half of a rotor plate during tilting event

A total momentum per entire rotor plate may be obtained through integration of incremental moments per both rotor plates. The total moment depends on level of tilting as depict graph on Fig. 4-40.

The actual level of tilting may not exactly correspond to nominal angular misalignment due to bearing operation, but there is possibility of even excessive tilting since the total moment acts in the direction of tilting, and therefore actively amplifies this phenomenon.

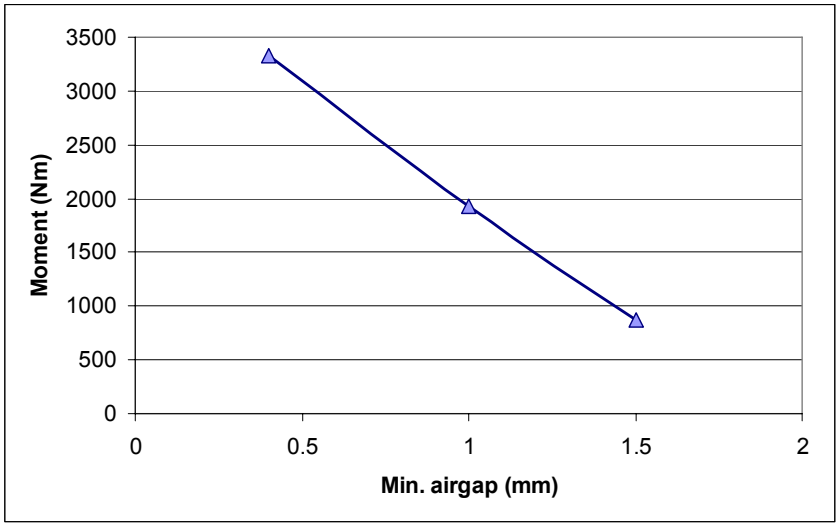

Fig. 4-40 Moment versus minimal airgap during various tilting events

4.5.4. Combined case

The last case to be analyzed in terms of axial forces is the combined case of axial shift and angular displacement. The combination of these phenomena plates illustrates Fig. 4-41 below:

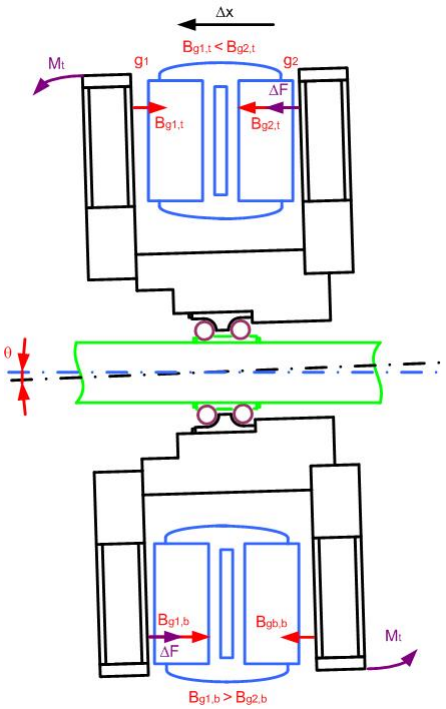

Fig. 4-41 Impact of axial shift and angular misalignment on MG2 operation

The case to be analysed assumes outcomes of DVA as declared in preamble to the Chap. 4.5, therefore $\Delta z = 0.59mm$ of combined effect of tilting and pure axial shift at rotor plate outer diameter. In terms of actual load, it is beneficial to assume average loading in terms of torque (157.8Nm) and speed (1217.2rpm) according to Manhattan drive cycle (Chap. 1.3). This allows to determining average momentum applied to the bearing due to the machine operation. By applying the same analysis and postprocessing methods as during previous cases for pure axial shift and tilting, the average bending moment applied to the bearing was determined at 271.1Nm. This provides necessary input for estimation of bearing selection and calculation of its lifetime.

5. Thermal Design

Assessment of thermal behavior of the electric motor-generator for a hybrid electric vehicle does not reduce to estimation of steady-state winding temperature, but rather focuses on prediction of temperature of the machine in transient operational mode. Concept of water cooling introduces a degree of freedom in terms of the machine control, so that the coolant flow rate may change adaptively according to instantaneous temperature of the machine and desired shaft power. This is an opportunity to enhance further efficiency of the hybrid electric vehicle by reducing pump power supplying coolant to the machine once the power demand to the machine is reduced. This suggests necessity of a thermal model to be able to cope with variety of operational conditions in terms of coolant flow rate and its inlet temperature, ambient temperature, drivecycle of the machine determining profile of losses versus time, and 'thermal history' reflecting past operation of the machine. In other words, what are the initial conditions in terms of winding temperature at an instant, when the desired load is applied. This will determine instantaneous overload capability including duration of the overloading event. Closer is the actual winding temperature to its limit according to the temperature class of the insulation system, smaller is a room for maneuvering with power demand in overload mode.

The thermal design primarily ensures that the machine is allowed to operate permanently under nominal torque/power load at specified flow rate and coolant temperature without exceeding the temperature limit of the insulation class. However, it is necessary to understand first a chain of relations beginning by the coolant flowing through the jacket as the main input to the cooling system. The chain continues by the heat transfer from the stator core to the cooling jacket, then by the loss model able estimating distribution and quantity of losses within the machine at any load point, and ending by instantaneous winding temperature as a main outcome of the thermal modeling and design.

5.1. Design and modeling of water-cooled machines

The range of options for design of cooling for electrical machines in HEV narrows down to application of liquid cooling due restrictions given by actual hybrid powertrain, in other words, the available real estate within the vehicle's chasis. Since the hybrid vehicles frequently operate in harsh environment, it is adequate to require totally enclosed design preventing pollution of the machine, and its winding in particular, by solid particles and chemical substances from ambient. Having said this, there is very limited heat transfer from the stator to ambient due to natural convection since the air exchange with ambient practically does not exist. The available options in terms of cooling options are narrowed down to application of the engine coolant water/glycol, or hydraulic oil available in wet clutches or transmissions. Hydraulic oil allows both direct and indirect cooling of windings in terms spraying the endwindings and in the same time, by circulating oil through the cooling jacket of similar

construction as presented on Fig. 2-1. However, application of oil as a coolant would require installation of separate cooling circuit with dedicated oil pump, a reservoir and a radiator. This may bring additional cost involved as well as space requirements as far as the vehicle integration is concerned. Though the choice of water/glycol as a coolant allows indirect cooling through the water jacket only, this solution introduces several advantages. Namely, opportunity for sharing the same cooling hardware with the engine as well as some favorable physical properties of water/glycol as the coolant, particularly lower viscosity and higher specific thermal capacity than the hydraulic oil. This may reduce requirements for the pump power.

The design and modeling of the cooling system assumes the only effective heat rejection path through the cooling jacket. Since the rotor structure is laminated with magnets protected from spacial harmonics of magnetic field by rotor laminations, it is assumed that the only heat sources are on the stator side in terms of copper and iron loss. In other words, there is no heat rejection through the airgap due to totally enclosed design of machine, moreover with smooth surface of the rotor plates introducing minimum of air paddling in the airgap.

5.2. Heat rejection capability of the cooling jacket

The aluminium jacket is shaped like a torus and has a narrow duct in the middle where the coolant flows. The duct has got a 'width gradient' along its length due to presence of grooves, as is apparent on Fig. 2-1. These grooves force flow of the coolant to become turbulent and therefore, improve heat transfer. Since the axial thickness l_a of the duct formed in the cooling jacket is far smaller than its radial thickness l_r, $l_r >> l_a$, the hydraulic diameter [53] L of the duct is defined to be equal to twice the radial thickness l_r.

The inlet and outlet pipes are on the same side of the jacket and therefore, a temperature gradient is created between the outlet coolant T_{out} and inlet coolant T_{in} pipes due to the coolant flow and heat absorption. The gradient T_{out} - T_{in} is given by:

$$T_{out} - T_{in} = \frac{P_{loss}}{q_m \cdot c_s} \tag{5-1}$$

where, q_m is mass flow rate, P_{loss} is the power loss to be dissipated from the stator and c_s is the specific thermal capacity of the coolant. Equ. (5-2) gives the average coolant temperature T_{av} with temperature of the aluminium duct surface T_{Al} obtained from CFD:

$$T_{av} = T_{Al} + \frac{T_{in} - T_{out}}{\ln\left(\frac{T_{in} - T_{Al}}{T_{out} - T_{Al}}\right)} \tag{5-2}$$

The assumption of turbulent flow in the duct needs to be supported by calculation of Prandtl number Pr, which should for turbulent flow lies in the interval $0.7<Pr<2500$. Prandtl number is given as:

$$\mathrm{Pr} = \frac{\mu}{\alpha \cdot \rho} \tag{5-3}$$

The coolant physical properties, such as thermal diffusivity α, mass density ρ and dynamic viscosity μ were adjusted according to the average temperature of the coolant.

Reynolds number Re needs to exceed 10,000 for the flow to be qualified as turbulent, and was determined as:

$$\mathrm{Re} = \frac{q_m \cdot L}{\mu \cdot S_{cj}} \tag{5-4}$$

where S_{cj} is cross-sectional area of the aluminium jacket duct. Once the assumption of turbulent flow in the cooling duct is validated, Dittus-Boelter correlation [53] is applied to determine a value of Nusselt number Nu:

$$Nu = 0.023 \cdot \mathrm{Re}^{0.8} \cdot \mathrm{Pr}^{0.4} \tag{5-5}$$

Heat transfer coefficient h is obtained from a Nu, L and thermal conductivity of the coolant λ:

$$h = \frac{\lambda \cdot Nu}{L} \tag{5-6}$$

A set of Equ. (5-1) – (5-6) provides closed-form solution for estimation of heat transfer coefficient for a given flow rate of the coolant, and its variable physical parameters. However, such analytical solution may introduce an error, with its potential distribution across following calculations. Therefore it is convenient to validate the analytical model numerically since a functional prototype may not be available at this design stage for practical tests. CFD is considered as a reliable way of obtaining heat transfer coefficient or static temperature distribution [54] over inner surface of the cooling jacket. The actual CFD simulation work was taken over from design of Motor-Generator MG1 with exactly the same design of the cooling system. Simulation cases of the volumetric flow rate from 5 up to 20 l/min, inlet temperature of 65 degC and total loss generated in the stator 1000 W were considered for calibration the of the analytical model, which was developed for MG1 first, and then transferred on MG2 design. Temperature distribution over a heat sink surface for a particular case of flow rate at 10 l/min depicts Fig. 5-1 below:

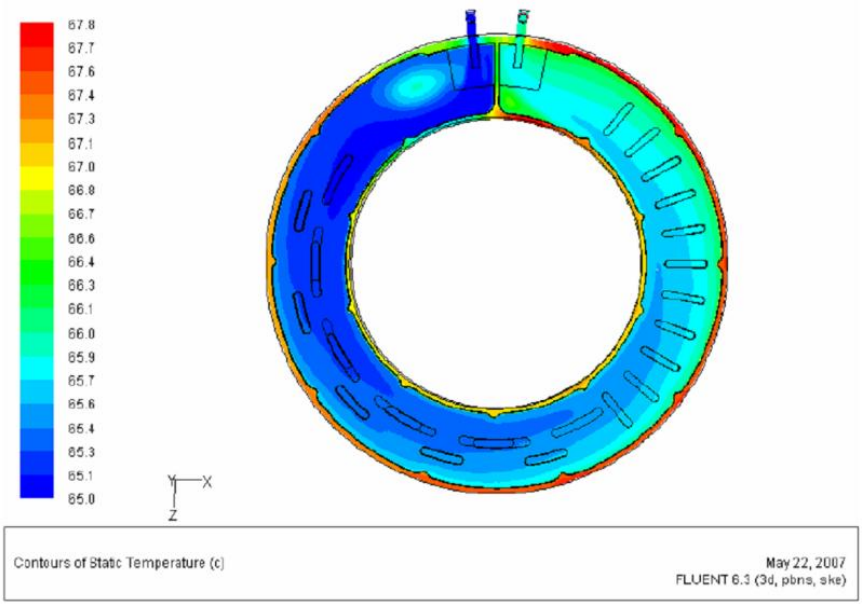

Fig. 5-1 Static coolant temperature in MG1 cooling jacket obtained using CFD

followed by distribution of heat transfer coefficient at inner surface of the cooling jacket for the same case of flow rate, as presented in Fig. 5-2.

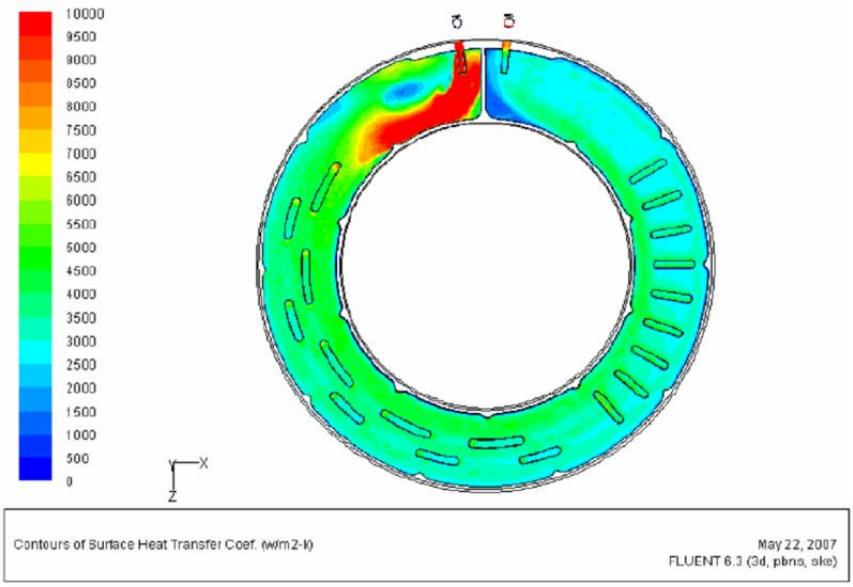

Fig. 5-2 Heat transfer distribution over MG1 heat sink surface

CFD – obtained results were applied to calibration of analytical calculations of heat transfer coefficient, calculated out of Nusselt number Nu. Both analytical and CFD calculations support application of Dittus-Boelter correlation, which is feasible for turbulent flow cases. Fig. 5-3 below illustrates CFD- and analytically-obtained heat transfer coefficient for MG1.

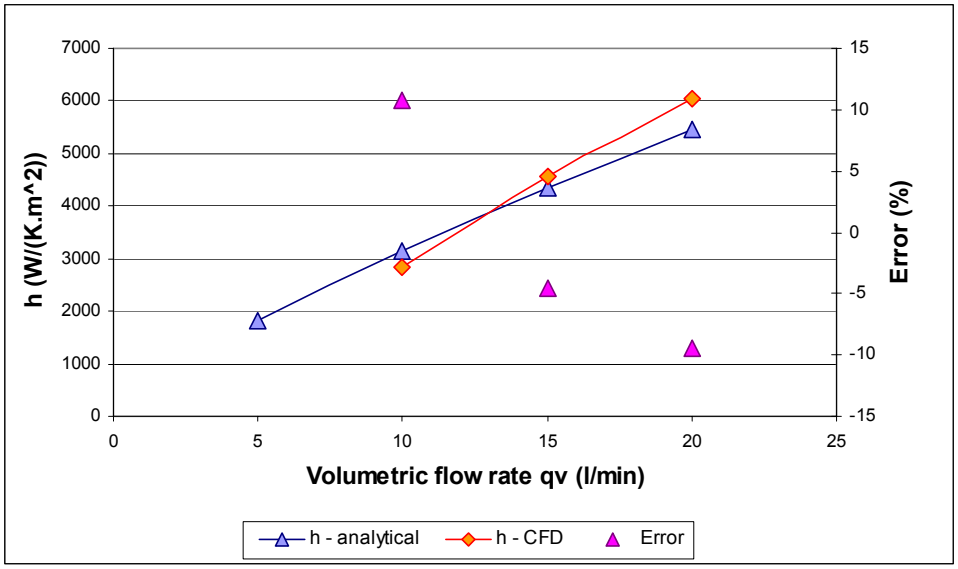

Fig. 5-3 Heat transfer coefficient as a function of volumetric flow rate for MG1 heat sink

The actual accuracy of analytical calculations versus results obtained by CFD is within 10% error margin for a range of flow rates from 5 up to 20 l/min. Analytical estimation of heat transfer coefficient for MG2 shows Fig. 5-4.

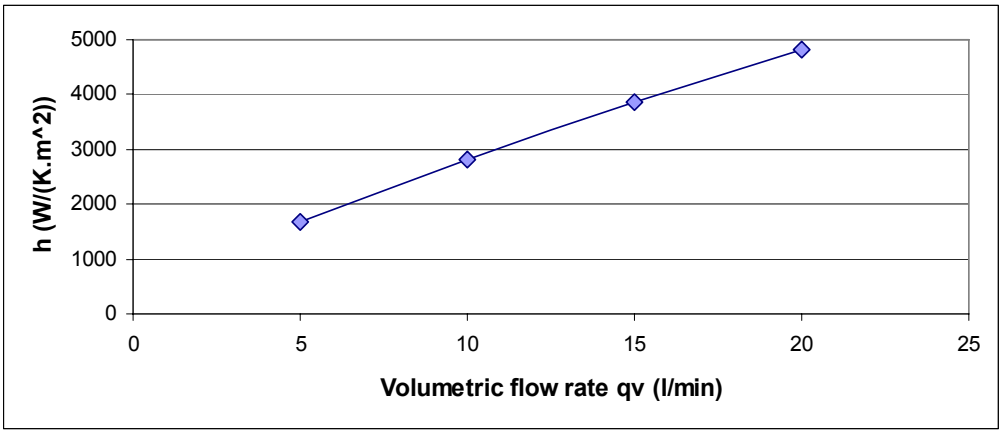

Fig. 5-4 Heat transfer coefficient as a function of volumetric flow rate for MG2

Modelling of heat transfer coefficient as a function of flow rate is necessary pre-requisite for estimation of the winding temperature as a main deliverable of thermal calculations in general.

5.3. Equivalent lumped-parameter thermal circuit

Heat dissipation out of Spoke Axial-Flux machine occurs vastly through the aluminium heat sink due to totally enclosed housing of the machine disabling any air flow from ambient, and thus convection heat transfer. It is feasible to model thermally with sufficient degree of accuracy only the stator subassembly in order to determine winding temperature in design stage for various load conditions. The rotor losses include in this particular case only eddy current loss in NdFeB Permanent Magnet material, and will be eliminated further. In terms of analytical estimation of winding temperature, equivalent circuit lumped-parameter network is feasible modelling tool [47]. The basic principle of such networks is to lump components with a similar temperature together, eventually represented by a single node. Particular nodes are then interconnected by thermal resistances effectively representing heat flow paths in between nodes. Each segment of the stator core is moreover represented by adequate thermal capacitance. Following Fig. 5-5 depicts distribution of heat fluxpaths in circumferential cross-sectional view through stator core.

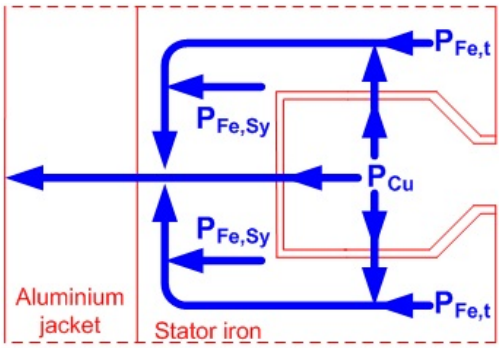

Fig. 5-5 Distribution of heat fluxpaths in the stator core in circumferential direction

Based on these assumptions, equivalent 3D transient thermal model consisting of 17 nodes has been developed. Assuming distribution of heat flux paths according to Fig. 5-5, the equivalent thermal circuit in linearized circumferential view is shown on Fig. 5-6. The thermal model is reduced to one slot pitch due to slot symmetry of the thermal model. In order to increase accuracy of the thermal model, the stator core is radially

divided into three tangential segments interconnected by thermal resistances. The thermal model includes major contributors to the total loss in terms of copper loss P_{Cu} and core losses assigned to individual parts of the iron core as P_{t2b} for a half of stator tooth and P_{Sy} for a backiron portion of the stator core. Results of electromagnetic analysis, in particular outcomes of Chapter 4.2.5 and 4.3 were fed into the thermal model in order to obtain power loss distribution in the stator at a given load point.

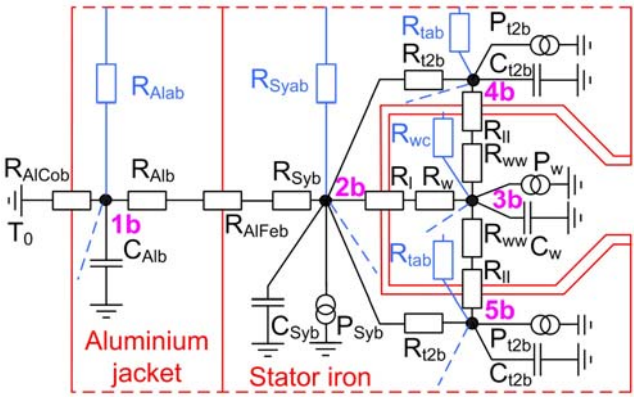

Fig. 5-6 Equivalent transient thermal circuit of the stator core in tangential direction

Since Spoke-Axial flux machine is toroidally-wound, there is a heat flow path following circumference of the coil, effectively conducting heat from winding overhangs into the stator core, since there is not high thermally conductive material in between the cooling jacket and the winding overhang. Following Fig. 5-7 depicts cross-section and equivalent thermal circuit through a half of a coil illustrating directions of heat flow within the coil.

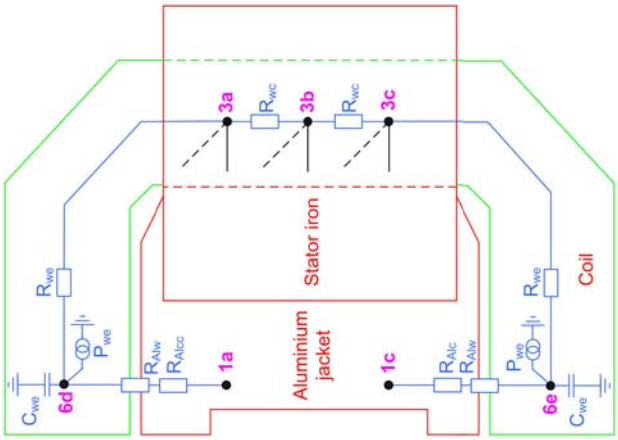

Fig. 5-7 Equivalent transient thermal circuit of the stator core in radial direction

Thermal resistance R_{th} generally depends inverse proportionally on the heat transfer coefficient h and the surface heat rejection area S_c, as describes Equ. (5-7) below.

$$R_{th} = \frac{1}{h \cdot S_c} \tag{5-7}$$

It may be convenient to reformulate expression for R_{th} as a function of thermal conductivity g_{th}, S_c, and length of the heat rejection path l according to following Equ. (5-8).

$$R_{th} = \frac{l}{g_{th} \cdot S_c} \tag{5-8}$$

Thermal capacitance C_{th} of a particular part of the machine depends on its mass m, and specific thermal capacity of a referred material c_{th}.

$$C_{th} = m \cdot c_{th} \tag{5-9}$$

Actual solution of the equivalent thermal circuit benefits from analogy between electric and thermal circuits so that one may by applying the method of nodal temperatures assign:

$$\frac{dT_w(t)}{dt} C_{th} + T_w(t) \cdot \lambda = P_{loss}(t) \tag{5-10}$$

where λ is thermal conductivity of a particular material.

Since the particular equivalent thermal circuit described in this paper consist of 17 nodes, it is therefore described by a set of 16 linear differential equations based on Equ. (5-10). This equation may be rewritten for convenience of numerical calculations, considering a time step Δt, into following form:

$$\frac{T_{w1} - T_{w0}}{\Delta t} C_{th} + T_{w1} \cdot \lambda = P_{loss} \tag{5-11}$$

where T_{w1} is winding temperature at actual time step, whereas T_{w0} was temperature of the winding in the previous time step.

The distributed equivalent thermal model may be simplified into equivalent circuit containing only a single thermal resistance and capacitance according to Fig. 5-8.

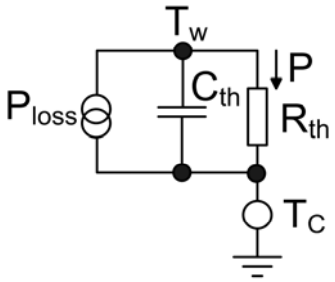

Fig. 5-8 Simplified equivalent thermal circuit based on RC constant referring to the coolant temperature T_c as a reference

Such approach approximates distributed network of thermal resistances and capacitances from the winding to the heat sink by single thermal resistance R_{th}, describing therefore effective thermal resistivity of this heat flux path. Similarly, C_{th} lumps distributed thermal capacitances of the machine components into a single one. Such simplification may be advantageous particularly for simulations on a vehicle level reducing complexicity of the vehicle model and thus, overal computational time.

5.4. Prediction of winding temperature rise

Coupling of the equivalent transient thermal circuit with heat transfer calculations for the heat sinks helps in understanding of the winding temperature for variety of cases in terms of the machine load and coolant parameters, such as its flow rate. The following Fig. 5-9 illustrates dependency of the equivalent thermal resistance R_{th} according to Fig. 5-8 on the coolant flow rate at inlet temperature of 105degC through the heat sink:

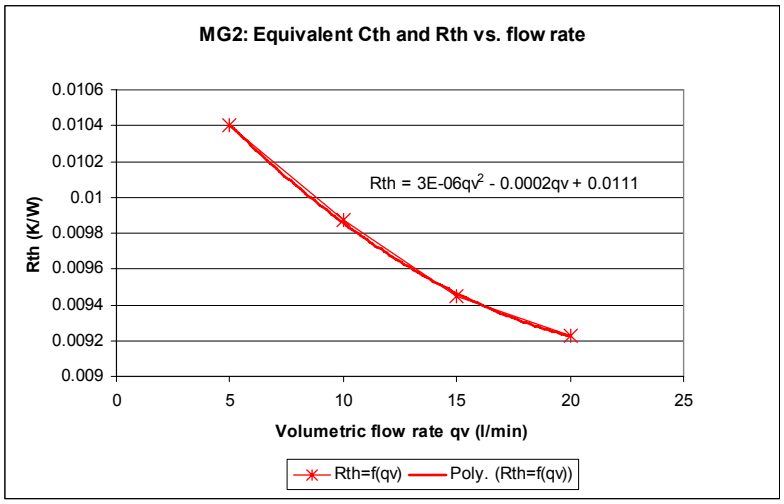

Fig. 5-9 Dependency of the equivalent thermal resistance R_{th} on a coolant flow rate

The profile of thermal resistance on Fig. 5-9 assumes fixed load of nominal torque at base speed of 1300rpm, therefore generating the nominal power loss. The same conditions apply to Fig. 5-10 below, depicting dependency of average winding temperature on the flow rate.

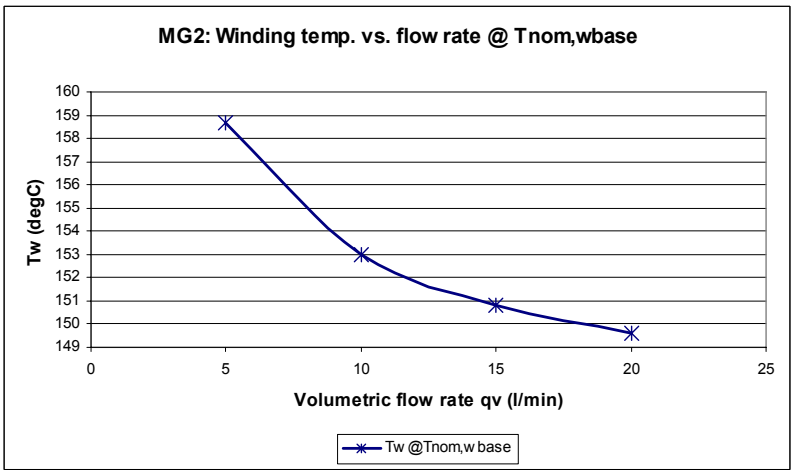

Fig. 5-10 Dependency of average winding temperature on a coolant flow rate

A rate of slope of the functional dependency of winding temperature on flow rate helps to optimize coolant flow rate through the heat sink. It is apparent that once the coolant flow rate exceeds 15 l/min, the effect of incremental increase of flow rate by 1 l/min reduces the winding temperature only by 0.13 K/l, unlike by 0.64 K/l for range of flow rates below 10 l/min.

A different way of interpreting results is using steady state winding temperature map as is shown on Fig. 5-11, exactly following in terms of reference torque and speed machine's operational zone. Coolant flow rate of 15 l/min at its inlet temperature at 105 degC is assumed.

Considering the maximum operational winding temperature at 160degC, each load point of the machine leading under thermal steady state temperature below this benchmark value, allows permanent operation at that point.

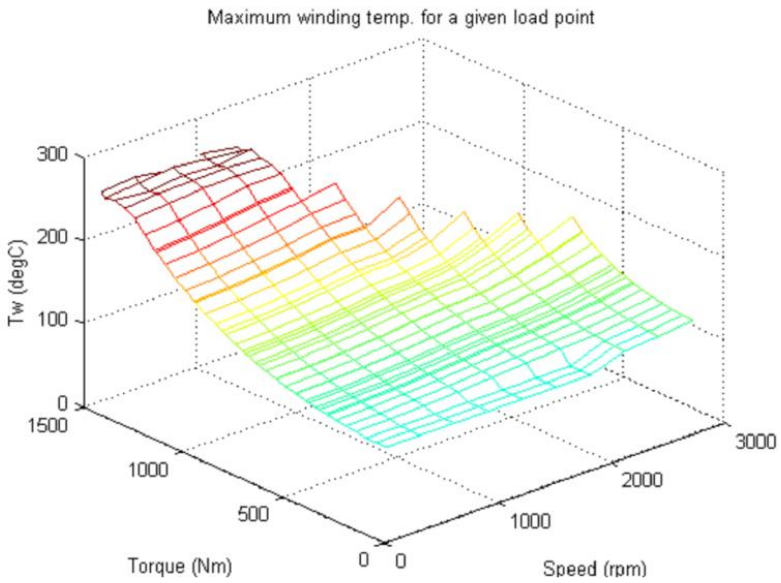

Fig. 5-11 Steady state winding temperature map at variable load for fixed coolant flow rate and its inlet temperature

However, the machine is designed to sustain the overload as well. Following Fig. 5-12 depicts time-on (scaled against thermal time constant τ as a ratio t_{on}/τ) as a function of duty cycle D, defined as ratio of time-on t_{on} versus period of the overload cycle T. Each particular curve is parameter of overload factor k, defined as ratio of actual power loss versus power loss at base point.

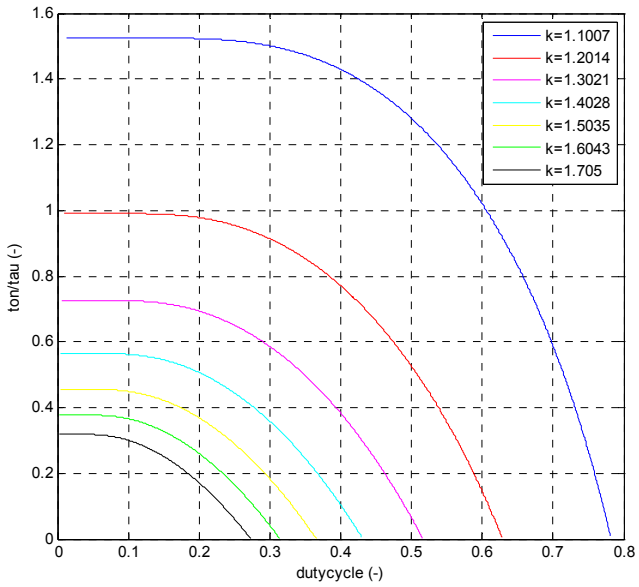

Fig. 5-12 Dependency of the thermal overload factor k on duty cycle and time-on

As an example, following the purple curve on Fig. 5-12 defining the overload factor $k \approx 1.3$, the machine under duty cycle $D \approx 0.4$ may stay at this load point for duration of 0.4τ, that means $113.24s$ before the load needs to be reduced at a level of power loss at the base point, or below. This simulation assumes initial winding temperature of 105degC prior loading of the machine starts.

The thermal analysis provides inputs for analysis of specific manufacturing and assembly techniques. There is a layer of thermal compound applied in between a stator core and the heatsink. Though the nominal thickness of thermal compound should reach

$0.15mm$, hence "Case B" at Fig. 5-13, the actual variation of the thermal compound thickness may vary up to $\pm 0.05mm$ either way due to manufacturing tolerances, mainly at the side of the laminated stator core. Fig. 5-13 illustrates sensitivity of the steady state winding temperature at base operational point against different thickness of the thermal compound.

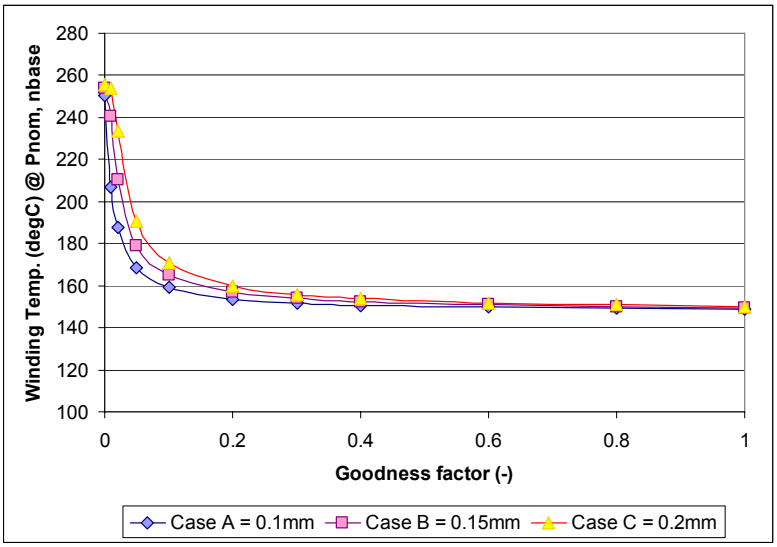

Fig. 5-13 Sensitivity of the winding temperature on thickness of the thermal paste and its goodness factor

The winding temperature on Fig. 5-13 is function of goodness factor of the thermal compound, where goodness factor "1" indicates ideal, consistent layer of the thermal compound without any porosities of voids. Zero goodness factor represents omitting of application of the thermal compound at all, therefore layer of air instead. The winding temperature is insensitive to the quality of the thermal compound layer, unless manufacturing techniques are significantly abused. Goodness factor of the thermal compound between the stator heat sink and the core is one of critical parameters to be monitored according to DFMEA process ensuring mitigation of potential failure modes.

6. Efficiency and Control of MG2

One of the critical requirements for electric drive applied in hybrid electric vehicle is maximization of efficiency. There are several contributors to this process, or in other words, to minimization of losses generated by the MG2 and its drive. Therefore, it is necessary to consider efficiency not only as one of the critical objectives of actual machine design, but to assess efficiency of power electronics supplying the machine, and also select appropriate control strategy for the drive as well. The power loss model adopts design developed particularly for MG2 drive. Design of power electronics was not a part of this work, and its loss model is introduced in order to complete the assessment of MG2 drive performance.

MG2 requires for its operation a control strategy, providing to the power electronics' controller reference values in terms of d- and q- axis currents. MG2 drive operates most likely in the torque-control mode, when reference torque is calculated of the requested power determined by the hybrid vehicle controller and actual speed of the vehicle. The actual power demand on the hybrid vehicle reflects position of the accelerator. The hybrid controller also decides whether MG2 will operate in motoring or regenerative braking mode. The idea is to capture as much of energy as possible during braking events in order to re-charge battery pack within its allowed limits, and therefore enhance the system efficiency. Sizing of the MG2 drive hence reflects the peak braking demand from the vehicle's requirements side.

The only exemption in terms of control mode for the MG2 drive would be for pre-transmission parallel configuration of the vehicle, when MG2 would have to ensure cranking of the engine through a slipping clutch in between MG2 and the engine. MG2 needs to bring engine on required cranking speed, and to keep the required speed for sufficient period in order to start the engine. The amount of torque and duration of the cranking event vary with particular engine, however demands for cranking torque rise generally with the engine displacement, and depends indirectly on temperature of the engine. However, this scenario is not applicable to the particular layout of the hybrid powertrain considered in this thesis.

The process of control strategy selection is therefore in an iterative loop with generation of power loss models for MG2 and its drive. The following pages do not focus on actual design of controllers, which are subject area beyond scope of this thesis. Instead, mathematical models of control strategies are provided, so that impact of control strategy selection on drive performance may be assessed.

Efficiency of the MG2 drive depends on parameters of the machine considered in its mathematical model. Parameters such as magnet flux linkage directly impact the torque production of the machine, hence its efficiency. It is noticeable that magnet flux linkage in particular depends significantly on the rotor temperature, which is a parameter the hybrid controller has no influence over. Therefore, impact of machine's parameters variation on efficiency based on operational conditions is analyzed as well.

6.1. Power loss of the electric drive

From a hybrid powertrain stand point of view, the electric drive may be considered as a "black box" consuming electrical power and delivering mechanical power on a shaft in the motoring mode, or vice versa in the generating mode. Let name efficiency of such energy conversion process as a drive efficiency. By having said this, it is appropriate to lump losses of both power electronics and electrical machine together, and to apply loss minimization conditions to the entire electric drive. The power losses by themselves are still allocated in the power electronics and the electrical machine separately, with exemption of impact of the power electronics switching frequency on additional stray core losses in the machine. However, analysis of additional core losses due to inverter switching frequency goes beyond the scope of this work. Therefore, it will not be included in the following power loss analysis.

6.1.1. Electrical Machine Loss Model

There are several main contributors to the power loss as far as electrical machine is concerned. The machine's power loss may decompose into:

- Copper loss
- Stator iron loss due to magnet field and armature current reaction
- Stray losses in the stator core as an effect of PWM-caused current ripple
- Eddy current loss in the heat sink due to current in stator winding overhang
- Eddy current loss in permanent magnets
- Eddy current loss in the rotor outer stainless steel retaining ring
- Bearing loss
- Windage loss

According to the modeling technique in dq0 reference frame adopted in this work, and corresponding equivalent circuit presented on Fig. 4-14, the loss minimization process effectively considers stator copper and core loss. Assuming fixed inverter switching frequency, the remaining power loss contributors would be lumped into category of uncontrollable losses, and simply added to the drive power loss after application of loss minimization conditions.

The equivalent circuit of synchronous PM machine according to Fig. 4-14 leads toward following expression of controllable power loss $P_{loss,EM}$ within the machine:

$$P_{loss,EM} = P_{Cu} + P_{Fe} = \frac{3}{2}\left(R_a \cdot \left(I_d^2 + I_q^2\right) + R_c \cdot \left(I_{dc}^2 + I_{qc}^2\right)\right) \tag{6-1}$$

The actual torque production of the machine is due to I_{q0} and I_{d0} components of total q-axis I_q and d-axis I_d current respectively, so that Equ. (4-30) describing machine's torque production may be rewritten into the following form:

$$T_{EM} = \frac{3}{2} p_p \cdot i_{q0}\left(\Psi_{PM} + i_{d0} \cdot \left(L_d - L_q\right)\right) \tag{6-2}$$

A possible way of achieving required values of I_{q0} and I_{d0} in the stator winding, in order to ensure accuracy of torque production and higher robustness of the control algorithm, is to add power loss compensator to the torque controller. The power loss compensator may offset reference torque as provided by the hybrid controller by adding additional compensation torque reflecting uncontrollable power loss for a given speed. One of possible ways how to implement such torque compensator is suggested on Fig. 6-1, when the compensation torque is stored as a single-dimensional look-up table defined versus mechanical speed. Mechanical speed is obtained through differentiation of actual shaft speed in time domain.

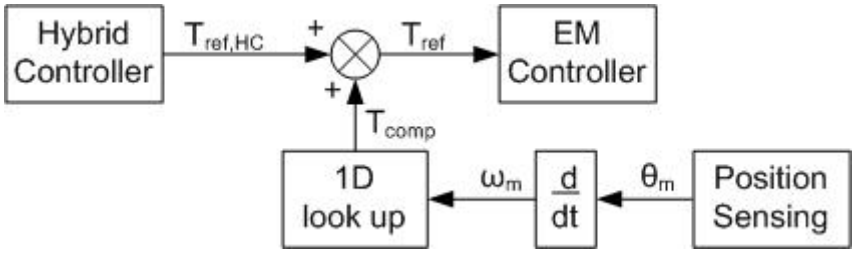

Fig. 6-1 Block diagram of torque compensation for uncontrollable losses of the drive

It would be possible to store uncontrollable power losses as a 2nd order polynomial and obtain compensation torque for a given speed through division operation, but that would cause increase of computational time from DSP stand point of view.

Assessment of the uncontrollable power loss summarizes Tab. 6-1. Each contributor to uncontrolled power loss is described by its functional dependency and actual coefficients related to it. Actual power loss for each of them was obtained at base speed. Eddy current losses as a particular case were calculated throughout FEA considering maximum load current as a worst-case scenario. Since eddy current losses are quadratically-dependent on frequency, eddy current losses are approximated by quadratic function without linear and constant coefficients. The windage loss was estimated based on [55].

Tab. 6-1 Assessment of uncontrollable power losses

	Acro-nym	Power loss at base speed	Remarks	Functional dependency	Coefficient value
Eddy current loss in heat sink	P_{HS}	325	At maximum current	$P_{HS} = a \cdot \omega_m^2$	$a=1.75 \cdot 10^{-2}$
Eddy current loss in permanent magnets	P_{PM}	42.5	At maximum current	$P_{PM} = a \cdot \omega_m^2$	$a=2.29 \cdot 10^{-3}$
Eddy current loss in rotor retaining ring	P_{RR}	9.9	At maximum current	$P_{RR} = a \cdot \omega_m^2$	$a=5.34 \cdot 10^{-4}$
Windage loss	P_W	19.3	-	$P_w = a \cdot \omega_m^2$	$a=1.04 \cdot 10^{-3}$
Main Bearing loss	P_{MB}	96.6	Nominal tilt/axial shift	$P_{MB} = b \cdot \omega$	$b=7.9 \cdot 10^{-1}$
Total uncontrollable Loss	P_{UC}	493.3	-	$P_{UC} = a \cdot \omega_m^2 + b \cdot \omega$	$a=2.62 \cdot 10^{-2}$ $b=7.9 \cdot 10^{-1}$

The total power losses of the drive may optionally include pump power required for circulation of coolant in the water jacket with experimentally estimated power consumption of 47.7W at maximum coolant flow rate. However, the coolant pump is

supplied from external 24VDC power supply, thus is not included in the loss model of the drive.

Graphically are uncontrollable power losses presented in Fig. 6-2, illustrating significance of the aluminum jacket losses due to eddy currents induced by armature current from endwindings. Labels in Fig. 6-2 for a particular power loss profile reflect assignment to a loss contributor from Tab. 6-1.

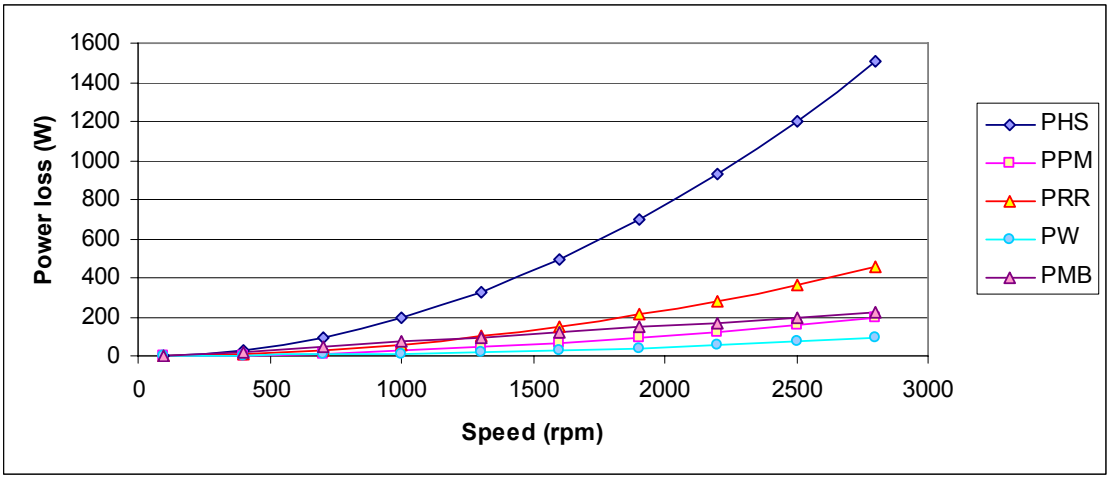

Fig. 6-2 Profiles of uncontrollable power losses versus speed.

The power loss profile of the main bearing was obtained for various bearing load cases in terms of applied axial forces. Through iteration with the bearing supplier, following profile of bearing loss versus speed, dependent on axial forces, was obtained for double angular contact bearing holding rotor plates of MG2, off 3312-A-2RS1. Fig. 6-3 depicts power loss profiles from zero up to 10kN of axial force as a boundary condition.

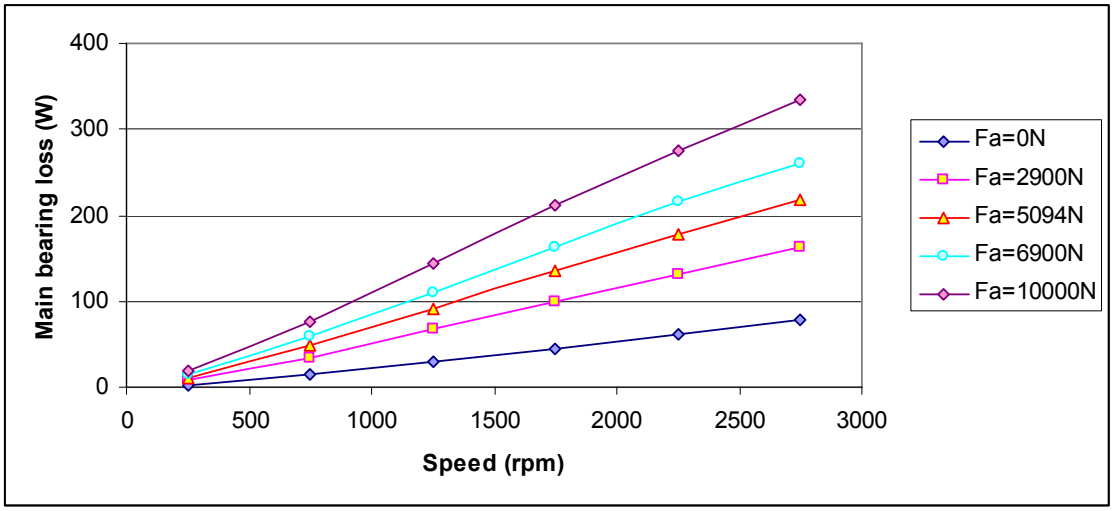

Fig. 6-3 Profile of the main bearing power loss as a function of speed and axial force

The bearing load case at 5094N of axial force corresponds to the torque and speed at average load case, axial displacement and tilting, as depicted in Chapter 4.5.4. The bearing is moreover permanently loaded radially by $F_r = 1216N$ due to gravity force corresponding to the rotor mass.

6.1.2. Power Electronics Loss Model

An integral part of MG2 drive loss model is representation of power electronics in terms of their losses. They may decompose into conduction and switching losses. Conduction losses P_c are determined out of Volt-Ampere characteristic of a device in on-state providing threshold voltage V_t and dynamic on-state resistance of silicon R_d at a specific load current so that:

$$P_c = V_t \cdot I_{av} + R_d \cdot I_{rms}^2 \tag{6-3}$$

Switching losses P_{sw} generally depends on switching frequency f_{sw} and dissipated energy during turning-on W_{on} and –off process W_{off} :

$$P_{sw} = f_{sw}\left(W_{on} + W_{off}\right) \tag{6-4}$$

A convenient way of obtaining switching losses is through switching energy as a function of current $W_{sw} = f(I)$ from a datasheet of the device by a quadratic approximation so that switching loss is function of time-variant current:

$$W_{sw}\left[I_a(t)\right] = E_{\max} \cdot k^2 \cdot \sin^2\left(\frac{2\pi}{T \cdot t}\right) \tag{6-5}$$

where $E_{\max}$ is datasheet value of the switching energy at maximum current, T is period of the current waveform and k is current utilization factor as a ratio between actual phase current and maximum current of the switching device.

The model for estimation of power electronics losses principally follows the block diagram on Fig. 6-4 below.

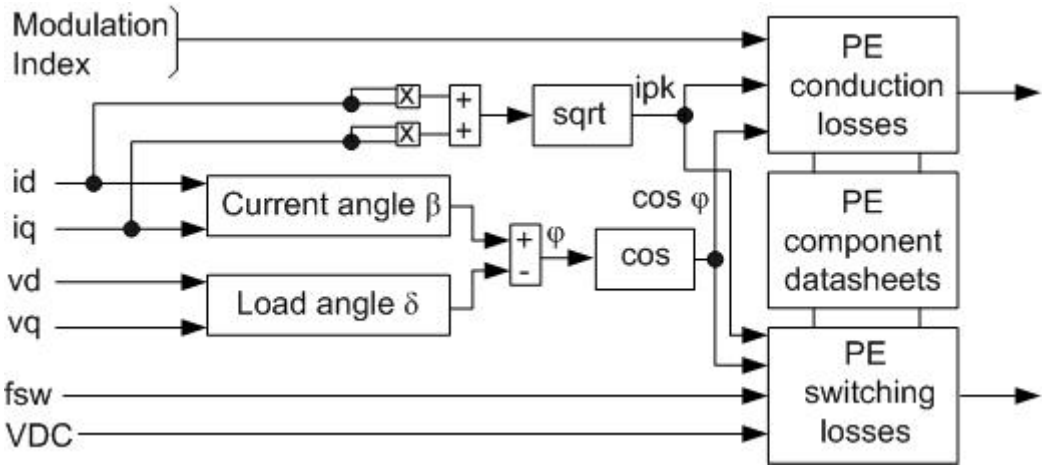

Fig. 6-4 Block diagram for power electronics loss calculation

The Modulation index M_i according to Fig. 6-4 is defined as a ratio of fundamental component magnitude of the line-to-neutral inverter output voltage V_{1m} to the fundamental component magnitude of the six step mode voltage $2 \cdot V_{DC} / \pi$

$$M_i = \frac{V_{1m}}{\frac{2}{\pi} V_{DC}} \tag{6-6}$$

Although power factor $\cos\varphi$ is not directly involved in calculation of power loss of power electronics devices, it influences quantity of power loss due to assumed modulation scheme. Implementation of Discontinuous Pulse-Width Modulation allows clamping of modulated phase either to positive or negative rail of the DC bus. In other words, zero sequence signal is added to the sine modulation waveform in an interval of up to $\pi/6$, when the modulation waveform is at its peak value. This modulation scheme thus allows minimizing of converter switching losses under unity power factor conditions due to pulling peak current through opened switch [56].

In the overall flow of the electrical drive loss simulation, the power electronics model directly links to electrical machine model in terms of d-and q- axis currents and voltages. The DC link voltage V_{DC} may be coupled as an input to a model of battery pack. The switching frequency assumed for these particular calculations is $f_{sw} = 10kHz$. Actual datasheet parameters for loss models of switching devices were obtained from design sheet of Semikron SKiM459GD12E4 power modules.

6.2. Control Strategies for Spoke Axial Flux Machine

There is wide variety of control strategies for electrical drives involving inverse-salient permanent synchronous machines, as they were already mentioned in Chapter 1.2. It is required to assess impact of each particular control strategy on performance and efficiency of the electrical drive in order to make a right selection for further implementation. However, alongside with performance and efficiency, there are other criterions involving robustness of the control algorithm, ease of implementation or computational demands affecting selection of appropriate DSP for the inverter control card. The scope of this work narrows following paragraphs into performance and efficiency assessment of control strategies.

6.2.1. Id=0 Control Strategy

The concept of Id=0 control strategy has been already introduced in Chapter 4.2.6. The reference current i_q^* is obtained out of Equ. (4-30). Due to its natural simplicity, Id=0 control strategy provides inherently straightforward implementation in terms of assessing i_q^* in order to achieve required torque production. Efficiency of MG2 drive under Id=0 control strategy is adopted as a baseline for further comparison of control strategies.

6.2.2. Maximum Torque-per-Ampere Control Strategy

Frequently employed option in terms of current control strategies for inverse-salient PM machines is Maximum Torque-per-Ampere (MTPA) Control Strategy providing besides maximization of torque-per-ampere ratio benefits by minimizing copper loss on the machine side and reducing current ratings of the inverter as well. An analytical way of calculating reference i_d^* current introduces Equ. (6-7) [40].

$$i_{d,MTPA}^* = \frac{\Psi_{PM}}{2\cdot\left(L_d - L_q\right)} - \sqrt{\frac{\Psi_{PM}^2}{4\cdot\left(L_d - L_q\right)} + \left(i_{q,MTPA}^*\right)^2} \tag{6-7}$$

The reference i_q^* current may be then obtained from Equ. (4-24).

However, the analytical expression according to Equ. (6-7) may fail in providing correct current references in a case of nonlinear machine parameters, as the particular design of Spoke-Axial Flux machine introduces non-linearity in terms of inductances according to Chapter 4.4.6. A block diagram on Fig. 6-5 proposes a way of calculating i_q^* and i_d^* currents for a general model of machine under MTPA control strategy for a machine with both nonlinear L_q and L_d dependent on phase current. The algorithm calculates optimal split of i_q^* and i_d^* for a particular value of phase current I_a throughout a search for peak torque production at the particular value of I_a using bisection method.

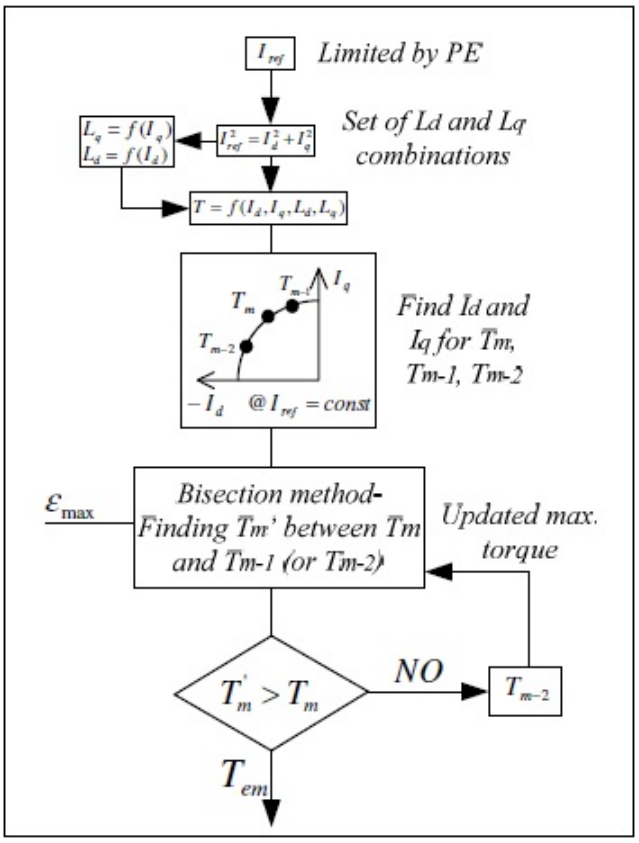

Fig. 6-5 Block diagram for calculation of reference i_q^* and i_d^* currents for MTPA control strategy feasible for a machine with nonlinear parameters, particularly inductances

The algorithm presented on Fig. 6-5 may be adopted for generation of reference polynomial generating dependency $i_{q,MTPA}^* = f(i_{d,MTPA}^*)$ substituting therefore Equation (6-7) and accounting for nonlinearities of the magnetic circuit. Such approximation could potentially suffer out of temperature dependency of flux linkage causing imprecision in generation of reference currents. Discussed trajectory of $i_{q,MTPA}^* = f(i_{d,MTPA}^*)$ depicts Fig. 6-6.

However, availability of MTPA is constrained by maximum input voltage. By neglecting voltage drop on the stator winding resistance, and assuming steady state operation of the machine, following condition defining requirements for input voltage may be formulated out of Equ. (4-26)-(4-28):

$$\left(\frac{V_{DC}}{\sqrt{3}}\right)^2 = \left(-\omega_e \cdot L_q \cdot i_q\right)^2 + \left(\omega_e \cdot L_d \cdot i_d + \omega_e \cdot \Psi_{PM}\right)^2 \tag{6-8}$$

Equation (6-8) represents an ellipse from mathematical stand point of view. Such ellipse is eccentric concerning the origin, with its centre point lying at negative portion of the x-axis. The ellipse represents voltage envelope for MTPA control strategy. Considering the MTPA reference current trajectory on Fig. 6-6, the intersection of the trajectory with voltage ellipse determines the boundary for MTPA at a given speed. That means MTPA is not available for anyhow higher q-axis reference current. The minor and major axes of the voltage-constrained ellipse are inverse-proportional to mechanical speed of the machine, as illustrates Fig. 6-6.

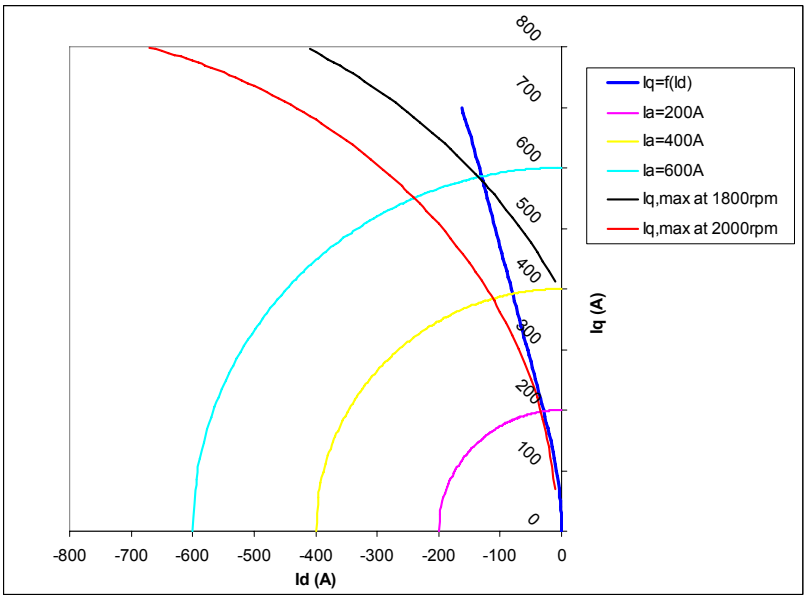

Fig. 6-6 Reference i_q and i_d currents for MG2 under MTPA taking into account nonlinear machine parameters and limitation due to maximum input voltage

Any requested load point, which would require combination of reference currents beyond the voltage ellipse, means transition into voltage-constrained field weakening.

Appendix A depicts proposal for actual implementation of MTPA controller. Reference i_q^* current is obtained out of desired torque T_{ref} considering i_d^* from previous time step of the controller according to sampling period of current sensing interface. The i_d^* for the actual time step of the controller may be obtained accordingly to Equ. (6-7) or by adopting polynomial dependency for MTPA trajectory $i_{q,MTPA}^* = f(i_{d,MTPA}^*)$ as is depicted on Fig. 6-6. Difference in between reference and measured d- and q- axis currents generate error signal for PI controllers in both d- and q- axis providing eventually reference voltages. The v_q^* and v_d^* reference voltages in abc reference frame are transferred to the PWM modulator after inverse-Park transformation. Eventually the PWM modulator controls gate drivers for each particular transistor of the three-phase inverter. Desired feedback signals are phase currents and rotor angular position.

The featured controller may be further improved by adding decoupling, that means compensating for cross-coupling voltages $\omega_e L_d i_d$ and $\omega_e L_q i_q$.

Practical implementation would also include current limiters for both d- and q-axis with priority for d-axis so that total current will not exceed the converter, or machine current limit.

The field-weakening control algorithm will be discussed further in Chap. 6.2.4.

6.2.3. Maximum Efficiency Control Strategy

The aim of Maximum efficiency control strategy is to minimize both copper and iron losses, as MTPA focuses on copper loss only. Ultimately, MTPA converges with ME control strategy for $\omega \to 0$, and therefore $R_c \to \infty$.

In terms of generation of reference i_q^* and i_d^* currents, Maximum Efficiency control strategy may be derived, with consideration of Equation (6-1) out of loss minimization conditions as a partial derivative of power losses and torque equations against d-axis current:

$$\frac{\partial P_{loss,EM}}{\partial i_d} = 0 \tag{6-9}$$

followed by

$$\frac{\partial T_{EM}}{\partial i_d} = 0 \tag{6-10}$$

The loss minimization conditions are, however, related to the losses of electrical machine only. The analytical solution is obtained by combining these loss minimization conditions, and in terms of d- and q- axis reference currents might be found in [57]. However, the computational complexity of such analytical solution hardly limits practical implementation of Maximum Efficiency control strategy into theoretical exercise, since the closed form solution does not consider variation of machine's parameters based on operational conditions.

6.2.4. Field Weakening Control Strategy

The main purpose for introducing of field weakening control strategy is to satisfy voltage conditions described by Equation (6-8). It is necessary to inject additional negative i_d current in order to reduce EMF by reactive voltage drop projecting into v_q voltage. Neither MTPA, nor ME control strategies are therefore valid. According to the controller proposal presented in Appendix A, the field weakening controller is superior to the actual current controller in d-axis, tracking whether the required DC bus voltage V_{DC}^* is smaller than available DC bus voltage $V_{DC,m}$. Once this condition is violated, the PI controller for field weakening ramps up negative i_d current.

6.2.5. Power Losses as a Function of Controlled Variables

The efficiency of an electric drive may be further optimized once power electronics losses are included. Power losses both of the electrical machine and the power electronics are in fact coupled by i_d and i_q currents as the controlled variables of the drive. It is therefore possible to plot both power electronics and electrical machine losses as a function of possible combinations of i_d and i_q currents providing the required torque production at a given speed. One may then discover the efficiency optimization potential for a given load point. Following Fig. 6-7 depicts profile of electrical machine, power electronics and overall drive losses at base speed, nominal torque load point.

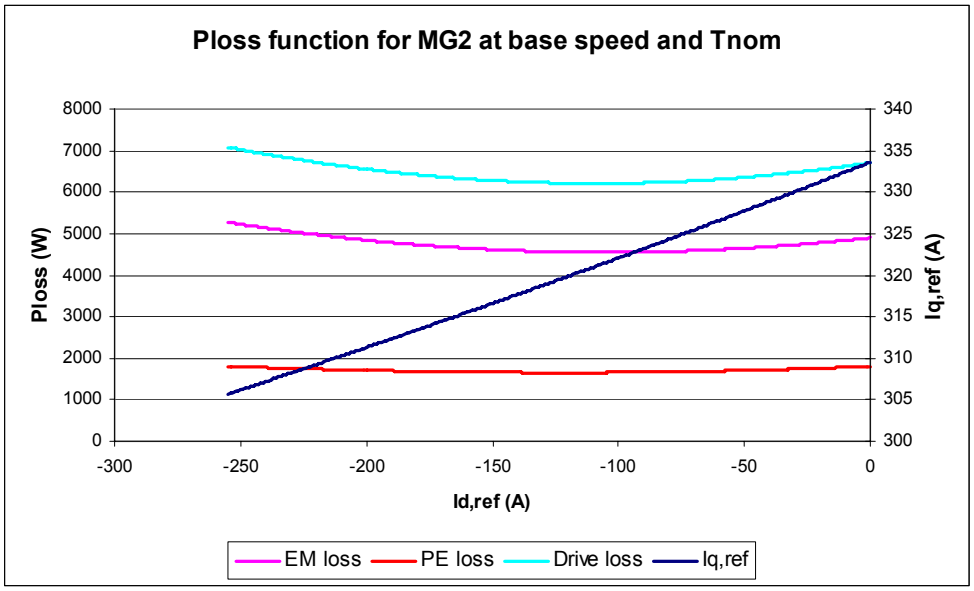

Fig. 6-7 Power loss of electric drive as a function of i_d at base speed, nominal torque

A similar loss profile presented on Fig. 6-8 was obtained for a load point at 1800rpm, 50Nm, which is typical by significance of iron losses in terms of proportion to overall machine losses. Obviously, iron losses would be greater at further elevated speed, however, the controller has to in such circumstances switch into field weakening mode, which in fact reduces reedom for any control action.

Tab. 6-2 summarizes for both considered load points reference i_d and i_q currents for selected control strategies, therefore Id=0, MTPA and Maximum Efficiency. The last-named control strategy benefits at 1800rpm, 50 Nm load point since this control strategy takes into account iron losses whilst optimizing drive efficiency. The overall efficiency benefits though did not exceed 0.5%. It is also noticeable, that power electronics losses might be slightly higher for ME than MTPA since ME requires greater phase current than MTPA.

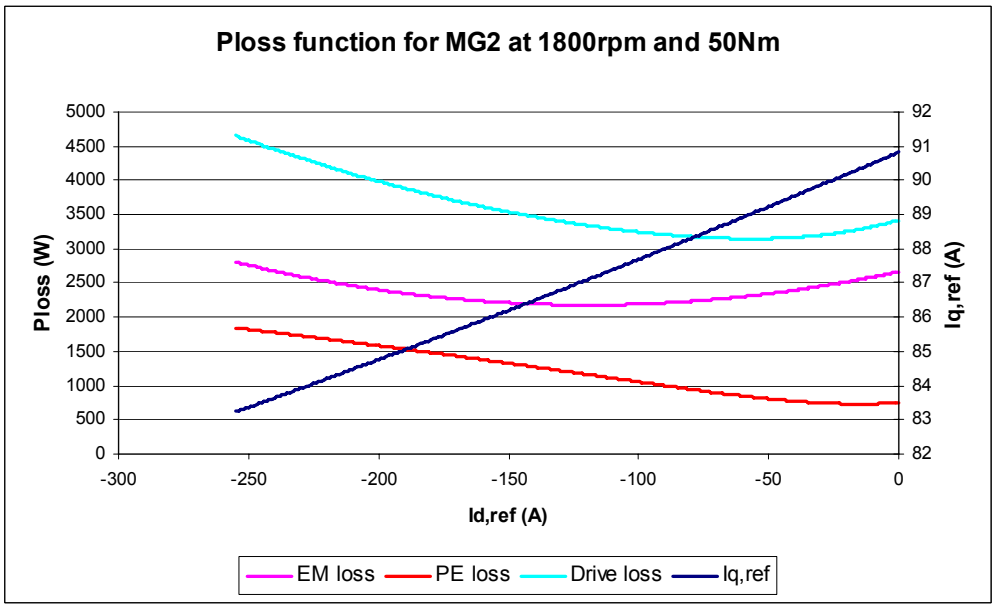

Fig. 6-8 Power loss of electric drive as a function of i_d at 1800rpm, low torque as a load point with significant iron losses

Tab. 6-2: Reference currents and efficiency at selected load points

Load point	Control strategy	id,ref (A)	iq,ref (A)	η (%)
735Nm, 1300rpm	**Id=0**	0	334	93.7
	MTPA	-38	329	94.0
	ME	-109	321	94.2
50Nm, 1800rpm	**Id=0**	0	91	91.7
	MTPA	-3	90	91.8
	ME	-57	89	92.3

The Maximum efficiency control strategy seems to be more beneficial for drives operating at higher speed, where iron losses would become more significant. It is therefore questionable, whether there is justification for implementation of ME control strategy for this particular drive. The control strategy selection should address complexity of the algorithm, and potential issues related to accuracy of estimation of i_d and i_q reference currents concerning variation of machine's parameters.

The power loss functions shown in Fig. 6-7 and Fig. 6-8 consider winding resistance R_a at 160deg, magnet flux linkage Ψ_{PM} accordingly to the rotor temperature of 70degC, and eventually DC bus voltage at 500VDC. Power electronics switching frequency is fixed at 10kHz. Since the level of DC bus voltage enforces transition into field weakening, the ME control strategy may further expand its operational zone if the battery pack is able to provide higher DC bus voltage depending on its state of charge.

6.3. Efficiency Maps for MG2 and its Drive

A way of representing efficiency of the electric machine, power electronics, or combined one for entire drive, is through efficiency maps. Unless it is flagged up, all presented efficiency maps below consider exactly the same conditions as applied to generation of power loss functions on Fig. 6-7 and Fig. 6-8.

6.3.1. Electrical Machine Efficiency Map

The primary aim of this section is to assess impact of control strategy on efficiency of the machine. For that purpose, efficiency maps for electric machine under Id=0, MTPA and ME control strategies were generated. The actual difference in efficiency is obtained by subtraction of efficiency maps according to the scheme presented on following Fig. 6-9. An efficiency map governed by a strategy with expected lower efficiency is subtracted from the one with greater predicted efficiency.

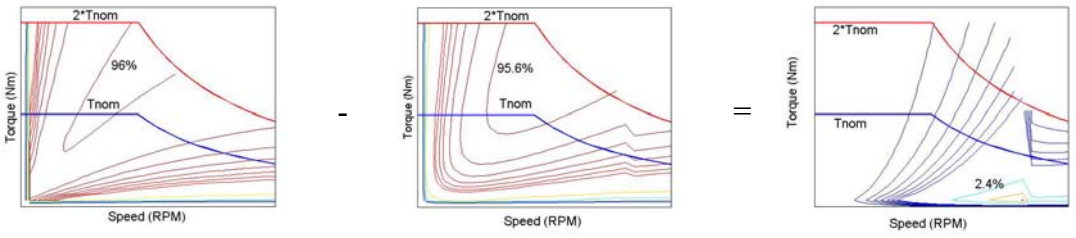

Maximum Efficiency - MTPA = Efficiency Improvement

Fig. 6-9 Proposed way for obtaining difference of efficiency under different control strategies

Since it is expected that ME will provide greater efficiency that MTPA, the efficiency map of electrical machine under MTPA is subtracted from the map under ME strategy. Analogically, an efficiency map under Id=0 is subtracted from the map under MTPA.

Advantageous feature of MTPA is utilization of the torque production due to employment of reluctance torque. Hence, it is expectable to observe efficiency improvement in low speed-high torque operation, as illustrates Fig. 6-10.

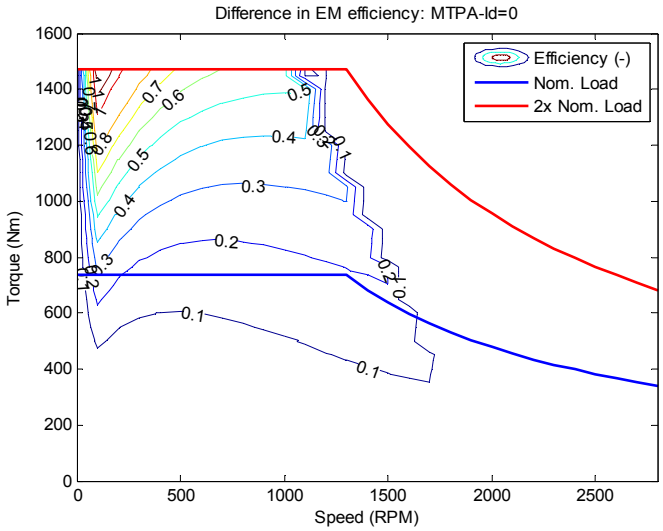

Fig. 6-10 Efficiency improvement for electrical machine under MTPA vs. Id=0

The observed improvement is up to 1% at peak torque production. Effect that is more significant would have been noticed for a machine design with greater $L_d - L_q$ difference in inductances, as a prerequisite for higher significance of reluctance torque.

Due to ME minimizes both copper and iron losses in the machine, ME should benefit in operational zones at higher speed and relatively low load torque, before the controller transits into field weakening mode, as depicts Fig. 6-11 below:

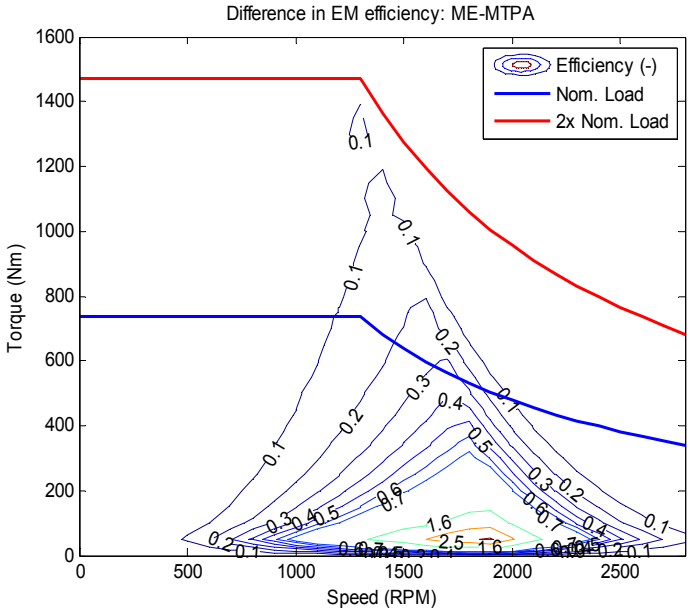

Fig. 6-11 Improvement in electrical machine efficiency under ME over MTPA control strategy

The peak efficiency improvement by employing ME control strategy instead of MTPA is up to 2.5%, as illustrates Fig. 6-11. The left-hand side boundary of the 'onion' illustrating efficiency improvement is determined by available DC voltage, thus transition into field weakening. ME transits into field weakening operation at higher speed due to higher proportion of $-i_d$ in the current split.

6.3.2. Overall Efficiency of MG2 Drive

A different outlook on the efficiency improvements provides inclusion of power electronics losses into the comparison in between control strategies. In a case of assessing benefits of ME control strategy, higher demands on phase current, as it has been presented in Tab. 6-2, almost wipe out the improvement achieved for separate electrical machine, dropping down from up to 2.5% to up to 0.6% only, as presents Fig. 6-12. One may doubt such improvement as potential error due to accuracy of models for both power electronics and electrical machine.

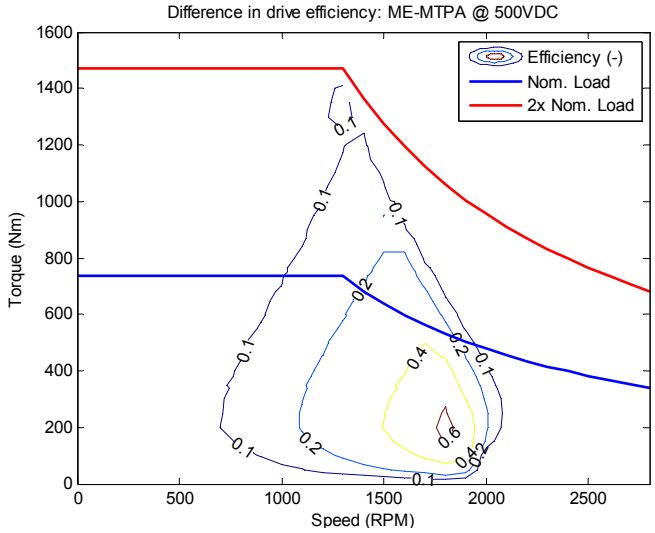

Fig. 6-12 Improvement in drive efficiency under ME vs. MTPA control strategy

Since the elevated DC-bus voltage may provide opportunity for extending the operational zone under ME control strategy, Fig. 6-13 shows efficiency improvement caused by ME over MTPA at maximum inverter DC supply voltage at 800V.

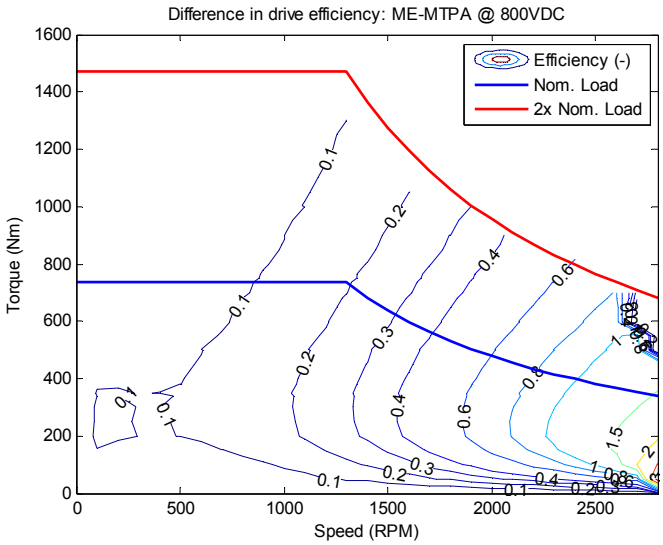

Fig. 6-13 Impact of elevated DC bus voltage at 800VDC on availability of ME strategy

It is noticeable that the machine is enforced to enter field weakening only in very limited proportion of its operational zone, at top speed of 2800rpm and peak power of 200kW. Then ME provides benefit up to 2% in drive efficiency at maximum speed due to further increased significance of iron losses on the machine side. However, a likelihood of operating the drive at DC-bus voltage of 800V is fairly low, as it is not desirable to keep the energy storage at full state of charge, which would cause such scenario to happen.

6.4. Sensitivity of Efficiency on Parameter's Variation

Efficiency of the drive depends on wide range of parameters, starting by those taking part in machine's equivalent circuit in dq0 reference frame. One may continue by DC bus voltage and eventually considering coolant temperature having impact on winding resistance, or ambient temperature influencing rotor plates temperature, and thus, magnet flux linkage.

6.4.1. Critical Parameter Tree Impacting Efficiency

Due to complex nature of parameters and their interrelations influencing drive's efficiency, it may be convenient to map up graphically actual involved parameters and their interrelations. A critical parameter tree in Appendix B appears to be feasible tool for such task. The flow of critical parameter tree follows objective of minimizing power losses of the drive, and thus maximize system efficiency. As the top-layer of the critical parameter tree identifies sources of power losses such as, the second and third line dive into actual parameters, which are off interest for purpose of efficiency modeling. Moreover, it is possible to control some of the involved parameters directly (in boxes with solid green background color), the other chunk of them is only indirectly influence able (parameters in boxes cross-hatched by green color), and eventually, parameters of the loss model left in blank boxes are completely uncontrollable, such as mechanical losses of the machine.

Directly controllable parameters, such as phase current or inverter switching frequency, could be enforced to the drive by a control action, hence, their impact on drive's efficiency is well-understood from previous sections. Attention needs to be paid to such parameters, which control has got only indirect influence over, since those may bring certain level of uncertainty into efficiency modeling.

6.4.2. Spread of MG2 Parameters

According to the critical parameter tree and specification of the drive determining boundary operational conditions, five parameters of the drive model described in Tab. 6-3 were identified as under indirect influence, thus potentially introducing uncertainty into efficiency modeling.

A good example of such parameter with only indirect control is DC-bus voltage VDC, dependent on state of charge of the battery back. DC bus voltage is in fact function of state of charge SOC of the battery pack, which is supposed to be kept in certain range by the battery management system (BMS), approximately in a range from 25% up to 70% based on a particular pack design. The drive controller has, according to the structure of HEV overall control, zero impact on decision making process of the

BMS, which follows commands of the hybrid controller. Though SOC is controllable variable, it is enforced parameter from electrical drive point of view.

Tab. 6-3 Spread of electrical machine parameters based on boundary operational conditions

Parameter *Condition*	**Min.**	**Mean**	**Max.**
Ra (mΩ)	6.93	9.73	14.32
Winding temperature:	*-40deg*	*60deg*	*160deg*
Ld (mH)	0.16	0.16	0.16
Current p.u.	*0.5*	*1.25*	*2*
Lq (mH)	0.286	0.242	0.217
Current p.u.	*0.5*	*1.25*	*2*
ΨPM (Wb)	0.2049	0.1803	0.1385
Ambient temperature	*-40*	*32.5*	*105*
VDC (V)	500	650	800
Battery SOC	*Depleted*	*Nominal*	*Fully charged*

Parameters described in Tab. 6-3 are considered as source data for Design-of-Experiment (DOE) exercise identifying spread of efficiency caused by each particular parameter out of this group.

6.4.3. Variation of Efficiency based on Spread of MG2 Parameters

Four different operational points of critical interest in terms of power split from hybrid control stand point of view, were considered for DOE exercise. A summary of these is provided in Tab. 6-4 below, with annotation as follows:

- LSHT: Low Speed-High Torque
- BP: Base Point
- TA: Torque Assist
- TEL: Transition Emission Load

DOE method varies involved input variables so that boundaries of unknown parameters, in this case efficiency, are obtained. Feeding the DOE by variables and their spread according to Tab. 6-3, following variation of efficiency was predicted, as describes Tab. 6-4 below.

Tab. 6-4 Identification of operational points for DOE, and estimated spread of efficiency

Operational point	**Reference Torque (Nm)**	**Reference Speed (rpm)**	**Minimum Efficiency (%)**	**Maximum Efficiency (%)**	**Difference in Efficiency (%)**
LSHT	1469.1	500	86.08	96	9.92
BP	734.6	1300	95.62	97.3	1.68
TA	500	1700	94.73	97.27	2.54
TEL	1000	1500	95.13	97.58	2.45

The maximum variation of efficiency up to 9.92% was predicted at LSHT operational point. Since the machine in LSHT operational point may be frequently employed for traction purposed both in motoring or regenerative braking, such spread may significantly involve optimization of power split in between ICE and electric machines in HEV.

7. Testing of MG2

The design and analysis iterations leading toward proposed and constructed MG2 design requires validation by test results. Proposed structure of tests focuses on demonstration of performance, efficiency, cooling capability and support of modeling work. Once a test setup is introduced, each particular test is described and presented in a separate section in terms of measured vs. predicted values.

Certain restrictions limited scope of performed testing. First of all, a set of dummy rotor plates was not available in order to perform split of no-load losses into iron, windage and bearing loss. Instead, no-load losses were measured on a machine with magnetized permanent magnets, thus providing these losses as a combined value at a particular mechanical speed.

Secondly, the three-phase inverter supplying MG2 was not able to provide maximum current of 480Arms. The inverter actually composes of two parallel-connected inverters with the same current conducting capability. Inductor on output for each phase balances off current loading for each branch of the inverter throughout inductive coupling. Since the magnetic core of the inductor saturates at approximately 390Arms, the torque and power availability of MG2 is limited accordingly.

7.1. Test Bed Setup and Instrumentation

Testing as described in this work, took its place in Tech Centre of Cummins Generator Technologies, Stamford, UK. Following Fig. 7-1 illustrates MG2 in its housing as a part of test bed setup, ready for testing.

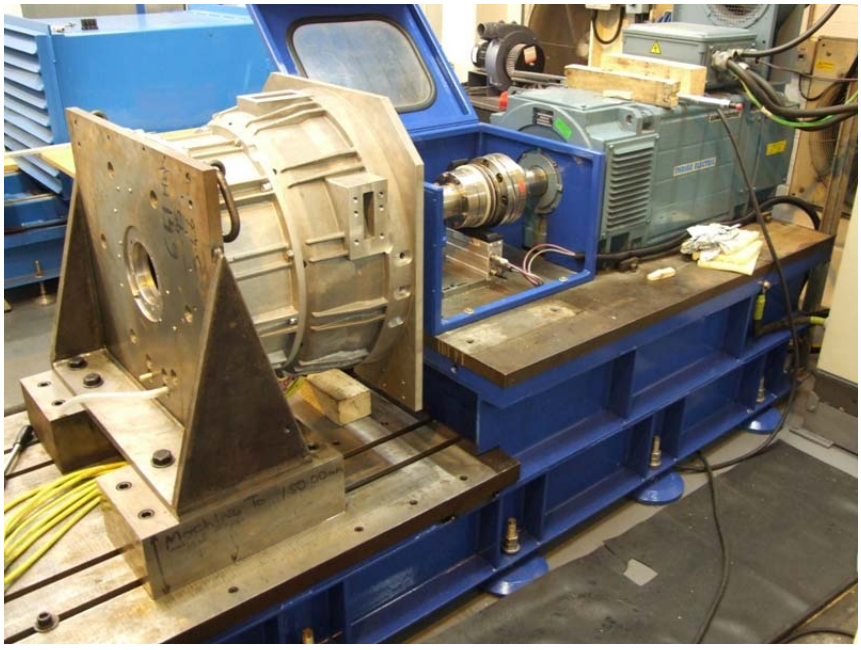

Fig. 7-1 MG2 as a part of the test bed setup

The actual test setup includes a DC motor drive able of operation in four quadrants of torque-vs-speed map, driving or braking MG2 depending on required operational mode. The DC motor also includes reference speed measurement. The driveline then continues by strain-gauge torque transducer, followed by flexible coupling and actual MG2 located in its housing. The MG2 housing is mechanically connected to the vertical support plate via MG1 housing. The MG2 housing also holds the clutch spindle, fulfilling role of support for the MG2 double-angular contact ball bearing. The entire MG2 assembly is in terms mechanical alignment further aligned by a MG2 support plate holding input shaft to MG2 throughout deep-groove ball bearing.

The actual measurements were performed with a set of instrumentation including LCR meter, three-phase power analyzer, micro ohm-meter and torque transducer, as shows Tab. 7-1 below, including detailed information concerning each particular instrument.

Tab. 7-1 Instrumentation taking place in MG2 testing

Name	LCR-Hi Tester	Digital Power Analyzer	Micro Ohmmeter	Torque Transducer	Data Logger/Data Acquisition Unit
Vendor	Hioki	Yokogawa	Tinsley	HBM	Fluke
Model	3532-50	253751-EI/EC	5895	T12/2kNm	2625A/2620A
Serial No.	2001-0340982	91H718811	013242101	122030056	9328011

The list of instrumentation includes data logger/data acquisition unit for connection of RTD temperature sensors measuring instantaneous winding temperature during heat runs.

7.2. Winding Resistance

The Tinsley 5895 Micro Ohm meter was used for measurement of the winding resistance. Actual measurement considers line-to-line resistance, which is then divided by two in order to obtain resistance per a phase. The measured value at 8.8degC ambient temperature is $R_{a,m} = 9.172 m\Omega$. The initial design calculations predicted for the same temperature $R_{a,p} = 11.007 m\Omega$. Such discrepancy is due to different applied winding technique in terms of arrangement of interconnections in between groups of coils. Moreover, a cable with increased cross-sectional area in comparison to flying leads with the same copper cross-section as in a slot was applied for connection to a terminal block. The spreadsheet was corrected accordingly, predicting currently $R_{a,p,corr} = 9.357 m\Omega$ at 8.8degC winding temperature.

7.3. Phase Inductances

MG2 is characterized as inverse-salient machine, thus having profile of inductances dependent on relative position of the rotor to the stator. Considering MG2 is 18-pole machine, a rotor locking mechanism with 40deg mechanical span and with discretization by 0.5 deg mechanical was developed. This allows fixing the rotor position and thus, overcome cogging torque prior to the measurement. Outcome of the inductance measurement in line-to-line arrangement is then a profile dependent on the rotor angle, with its peak in q-axis and a dip locating d-axis inductance.

Two different methods, by LRC meter, and by resonant LRC circuit were implemented, both providing close results. However, none of these testing methods considers phenomena of saturation of the magnetic core under relatively higher torque loads of the machine. An indirect method is applied, as is described in section 7.6 further, as a part of the torque production test.

7.3.1. Surge Test by RLC Resonant Circuit

The experiment setup consists of a capacitor *C* connected in parallel to the terminals of the winding as illustrates Fig. 7-2. The capacitor may be isolated from the winding by opening the switch *S2*. Having this situation as initial condition, a DC voltage source is connected via a switch *S1* to the terminals of the capacitor.

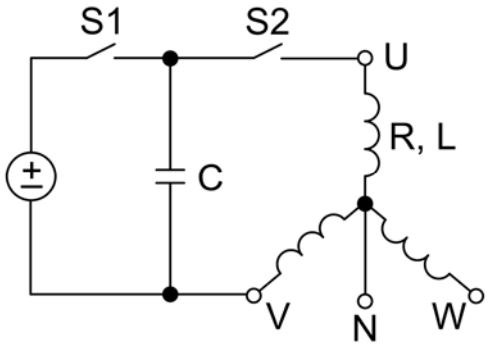

Fig. 7-2 Circuit diagram for LRC resonant circuit

Considering *S1* closed and *S2* opened, the DC voltage source charges up the capacitor to the required value. According to Fig. 7-3, a voltage level of 10V at the DC source was chosen.

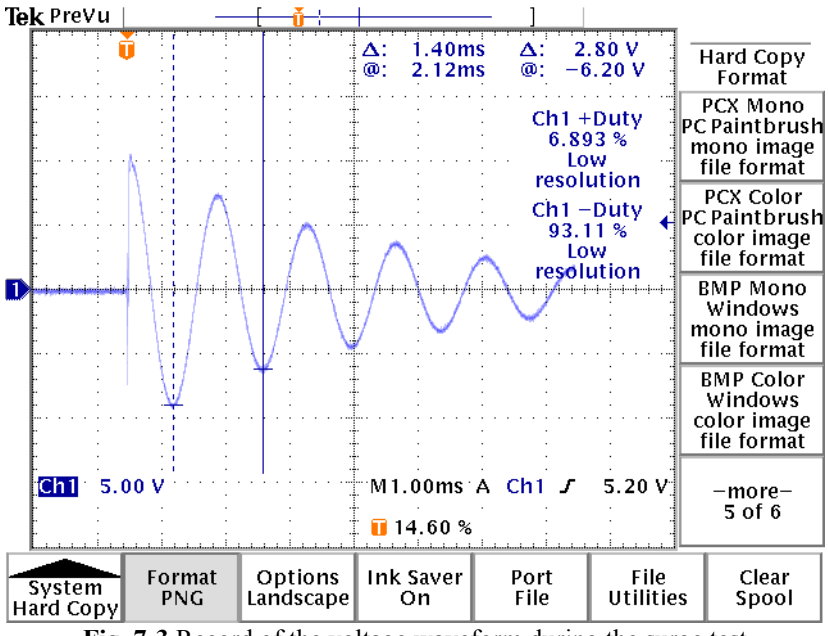

Fig. 7-3 Record of the voltage waveform during the surge test

Once *S1* is opened and *S2* closed, the capacitor discharges to the winding creating oscillatory waveform, with angular frequency corresponding to Thomson's equation:

$$\omega = \frac{1}{\sqrt{LC}} \tag{7-1}$$

Knowing the value of the capacitor and a period of the oscillation T according to Fig. 7.3, Equ. (7-1) may be rewritten into:

$$L = \frac{T^2}{4\pi^2 C} \tag{7-2}$$

A value of the capacitor may be preliminary selected so that the period of the oscillating waveform lays in a band of operating electrical frequencies of the machine, or specifically at a base electrical frequency.

7.3.2. Test Using LRC-Meter

The test using LRC meter was specifically performed at testing frequency of the internal AC source at 195Hz, matching up the base electric frequency of the machine. Both methods of Surge test by LRC circuit and Hioki LRC meter measured inductance with defined discretization in terms of rotor position by 0.5deg in 40deg span, thus inductance profiles vs rotor angle were obtained as illustrates Fig. 7-4 below.

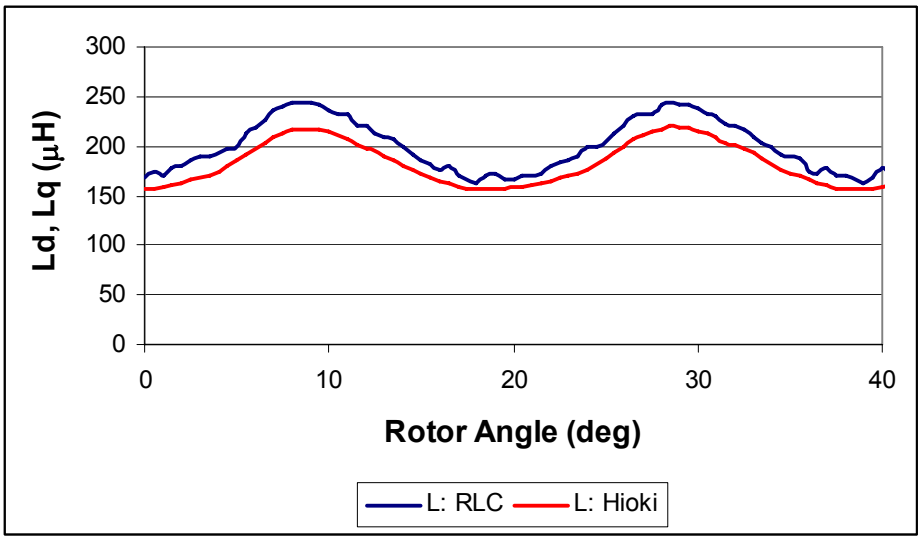

Fig. 7-4 Profile of phase inductance vs. rotor angle obtained by Hioki LRC tester and LRC resonant circuit

Tab. 7-2 below records values in terms of L_d and L_q for both testing methods and FEA analysis for comparison.

Tab. 7-2 Comparison of measured values of inductances with FEA-based prediction

Phase Inductances	Predicted FEA	Tested RLC	Tested Hioki
Ld (mH)	160	162	156
Lq (mH)	286	244	220

As measured values of L_d differs from FEA prediction by as little as $4\mu H$, in terms of L_q measurements shows results lower by up to $66\mu H$. The reason why FEA provided higher values might be in reduction of the FEA model into 2D domain at mean diameter of the machine. Therefore, FEA may not have captured impact of higher magnetic loading of stator teeth at inner diameter of the stator corepack, leading towards drop of permeability of electrical steel.

7.4. Back-EMF Test

Measurement of Back-EMF was performed by digital power analyzer allowing sampling of the actual voltage waveform and thus, further data postprocessing. Besides check-out of the actual EMF waveform vs. the one predicted by FEA, the postprocessing included analysis of harmonic content of the waveform. Moreover, linearity of EMF vs. speed was confirmed too.

7.4.1. Measurement of EMF

The EMF waveform, as presented on Fig. 7-5, was obtained at base speed of 1300 rpm and at 18.7degC ambient temperature. The no-load FEA considered exactly the same speed and temperature conditions as during testing in order to mimic the exact coercitive force H_c and remanent flux density B_r of the magnets.

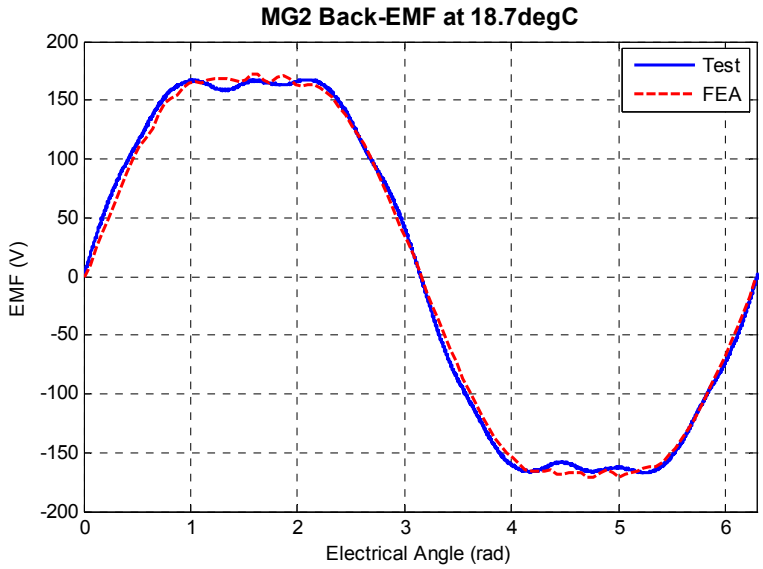

Fig. 7-5 Phase EMF waveform at 1300rpm

The FEA-predicted waveform includes all aspects of manufacturing causing extra leakage flux on the rotor side as it was discussed in Chap. 4.4.1.

The linearity of EMF vs. speed within complete operational range of the machine was verified at exactly the same temperature conditions, as is depicted on Fig. 7-6.

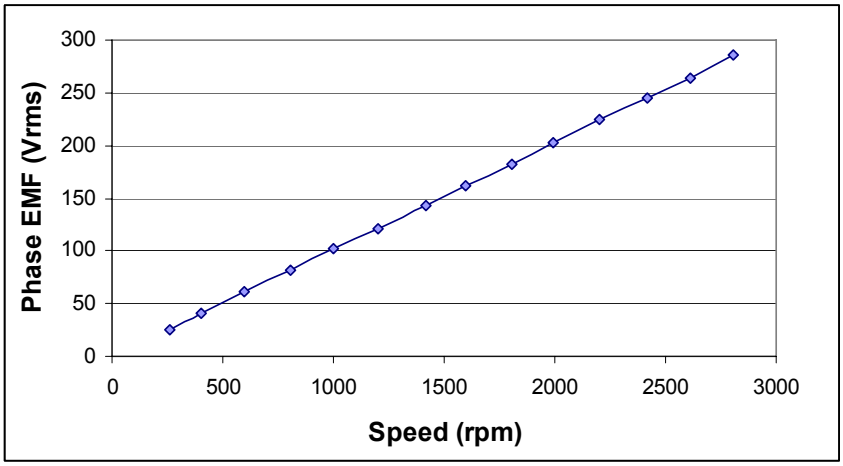

Fig. 7-6 Dependency of phase EMF on speed

The measurement results shown on Fig. 7-6 confirmed the assumption that EMF linearly rises with mechanical speed.

7.4.2. Harmonic Distortion of EMF Waveform

The waveform presented in Fig. 7-5 contains in fact raw data. It is necessary to apply Fourier analysis and discover the actual magnitude of the carrier waveform, and its higher harmonic counterparts. Tab. 7-3 below compares harmonic content of EMF waveform measured and obtained by FEA at 1300 rpm.

Tab. 7-3 Comparison in between predicted vs. measured harmonics of phase EMF

Harmonic Order	1st	3rd	5th	7th	9th	11th	13th	15th	17th	19th	21th
Peak Voltage - Measured (V)	188.03	24.7	2.57	1.22	3.89	0.21	0.68	0.59	0.14	0.14	0.04
Peak Voltage - Predicted (V)	189.29	17.34	2.86	0.25	0.86	0.13	0.21	0.51	0.2	0.18	0.48
Absolute Error (ΔV)	1.26	7.36	0.29	0.97	3.03	0.08	0.47	0.08	0.06	0.04	0.44

The first harmonic shows close match with absolute error of only $1.26V$. Critical for quality of torque production is the fifth harmonic reaching $2.57V$, which was accurately predicted.

7.4.3. Magnet Flux Linkage

Considering Equ. 4.25, the FEA predicted flux linkage constant to be $\psi_{PM,FEA} = 0.1535Wb$. The measurement results as presented in Tab. 7-3 show very close match in terms of EMF carrier magnitude, giving thus $\psi_{PM,m} = 0.1537Wb$.

7.5. No-Load Losses of MG2

The main purpose of no-load losses test is to identify and separate their contributors in terms of iron losses due to permanent magnets and mechanical losses, specifically windage and bearing losses. A way of performing testing focused on split of no-load losses is to measure combined no-load losses with a set of rotor plates having permanent magnets magnetized. In the next step, a test with dummy rotor plates separates iron losses from mechanical losses. However, the bearing losses may appear during testing with dummy rotor plates lower than in reality since axial forces due to magnetic field in the machine do not load bearings. A similar situation occurs if bearings would be simply spinned on the test bed in order to isolate windage loss from bearing loss. Then the set of bearings would not be loaded by radial forces due to gravity acting on the set of rotor plates.

Unfortunately, a set of dummy plates has not been manufactured in order to progress further with split of no-load losses. Thus, the no-load losses as a whole sum of iron and mechanical losses were estimated, as shows Fig. 7-7 below.

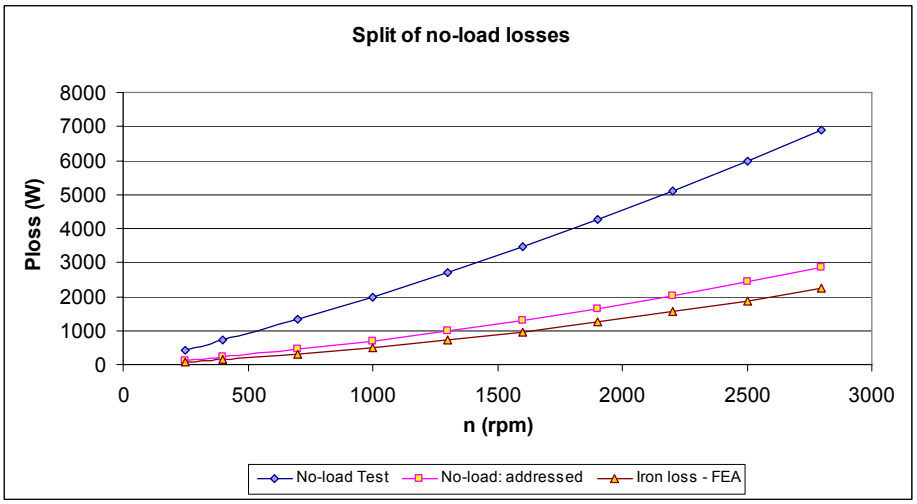

Fig. 7-7 No-load losses of MG2

Besides a sum of no-load losses, Fig. 7-7 illustrates also a proportion of no-load losses, which were addressed in modeling phase, and prediction of iron losses in particular. A detailed prediction of no-load losses contributors both in terms of torque and power vs. speed is presented in Tab. 7-4 below.

Tab. 7-4 Split of no load losses in terms of torque and power

n (rpm)	250	400	700	1000	1300	1600	1900	2200	2500	2800
wm (rad/s)	26.180	41.888	73.304	104.720	136.136	167.552	198.968	230.383	261.799	293.215
P No load Test (W)	410.493	707.338	1332.592	1999.930	2709.352	3460.858	4254.448	5090.122	5967.880	6887.722
T No load Test (Nm)	15.680	16.886	18.179	19.098	19.902	20.655	21.383	22.094	22.796	23.490
P Iron-FEA (W)	88.630	155.632	312.208	498.880	715.648	962.512	1239.472	1546.528	1883.680	2250.928
T Iron-FEA (Nm)	3.385	3.715	4.259	4.764	5.257	5.745	6.230	6.713	7.195	7.677
P Main Bearing (W)	9.310	21.636	46.358	71.174	96.084	121.089	146.188	171.382	196.669	222.051
T Main Bearing (Nm)	0.356	0.517	0.632	0.680	0.706	0.723	0.735	0.744	0.751	0.757
P Support Bearing (W)	26.116	42.432	75.101	107.819	140.585	173.399	206.262	239.174	272.134	305.143
T Support Bearing (Nm)	0.998	1.013	1.025	1.030	1.033	1.035	1.037	1.038	1.039	1.041
P Windage (W)	0.715	1.830	5.605	11.438	19.330	29.281	41.290	55.359	71.486	89.672
T Windage (Nm)	0.027	0.044	0.076	0.109	0.142	0.175	0.208	0.240	0.273	0.306
Addressed losses (W)	124.771	221.530	439.271	689.310	971.647	1286.281	1633.213	2012.442	2423.969	2867.794
Addressed losses (Nm)	4.766	5.289	5.992	6.582	7.137	7.677	8.208	8.735	9.259	9.781
Unaddressed losses (W)	285.722	485.808	893.321	1310.620	1737.705	2174.577	2621.235	3077.680	3543.911	4019.928
Unaddressed losses (Nm)	10.914	11.598	12.187	12.515	12.765	12.979	13.174	13.359	13.537	13.710
(No-load test) - (Iron loss,FEA) (W)	321.863	551.706	1020.384	1501.050	1993.704	2498.346	3014.976	3543.594	4084.200	4636.794
(No-load test) - (Iron loss,FEA) (Nm)	12.294	13.171	13.920	14.334	14.645	14.911	15.153	15.381	15.600	15.814

Tab. 7-4 also quantifies amount of losses which current modeling techniques were not able to identify (Unaddressed losses). The unaddressed losses project as almost constant drag torque reaching approximately 15Nm across wide speed range.

There are several factors introducing potentially error into prediction of no-load losses. In a particular case of iron losses (*P Iron-FEA* in Tab. 7-4), a common engineering practice multiplies specific iron losses as a data provided by steel supplier by a factor of $1.5 \div 2$ in order to accommodate impact of manufacturing on properties of steel. This includes mechanical stress during manufacturing of stator cores, in particular shear stress during slot punching, increased eddy currents at the edges, where slotting occurred or impact of elevated pressures during pressing of desired shape of the stator core. Moreover, the stator core is welded in radial direction in multiple cases on its back side in order to increase its mechanical stability. The specific iron losses were kept intentionally at values as provided by the steel supplier. Remedy out of the no-load measurement leads to a follow up project, which would focus on impact of manufacturing processes on specific iron losses. Besides this, it is desirable to quantify specific steel losses at elevated remagnetizing frequencies in order to capture impact of higher harmonic of magnetic field close to the maximum speed of the machine.

Furthermore, impact of distorted-sinusoidal voltage supply to the machine, leading to high-frequency current ripple should be assessed.

Another area for improvement of modeling techniques is in performing CFD analysis focusing on prediction of windage losses. Furthermore, CFD analysis would help to estimate heat transfer coefficient across the airgap and thus, allow extending the thermal model by rotor plates. A model for stream lines in the airgap and air velocity in there would support analytical modeling required for the extension of the thermal model.

In addition, accuracy of the bearing loss model may be further improved by mechanical analysis addressing distribution of axial forces per main and support bearing of the machine. Especially the support bearing, which is deep groove ball bearing is not designed for handling significant axial loads according to general mechanical design recommendations. This may lead to excessive losses in that bearing, impacting its lifetime.

7.6. Torque Production Test

The main objective of this test is to validate torque production of MG2 at nominal current and base speed. Furthermore, this test allows determining proportion of reluctance and magnet torque knowing the flux linkage constant and i_q current. Therefore, the magnet torque is subtracted from the total torque production.

The actual test is based on variation of current angle β, thus proportion between i_d and i_q current whilst keeping the total current constant. The actual measurement was performed in generating operational mode. The proportion of d-axis current increases with the current angle since the machine is operated under MTPA current control strategy. This projects into required input voltage, which decreases with the current angle. Profiles of torque production and voltage profile is depicted on Fig. 7-8.

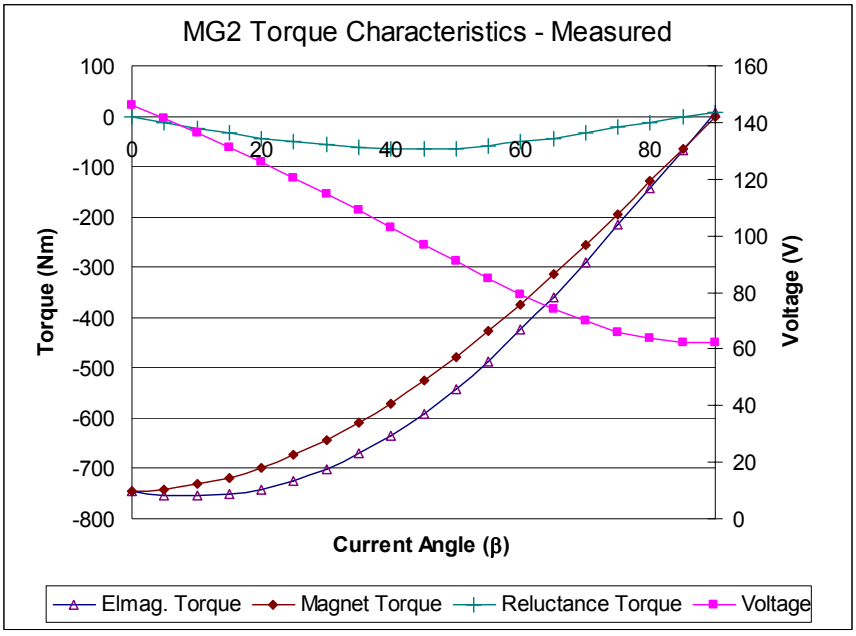

Fig. 7-8 Reluctance torque test at nominal current and base speed. The magnet torque is proportion of the total torque production due to permanent magnet flux, unlike electromagnetic torque includes both magnet and reluctance torque

In terms of actual torque production, the analytical model predicts peak torque of 773Nm at nominal current. The measurement has shown peak production of 744Nm for the same current applied to the machine. The discrepancy goes on account of 15Nm of unidentified no-load losses, which are not part of the analytical model. Moreover, the analytical model does not compensate for current ripple due to operation of PWM inverter, causing increase of RMS current without adequate rise in torque production. The inverter switching frequency was limited at 6.25kHz, though the design of the drive was aiming initially for 10kHz. Estimation of losses due to non-sinusoidal supply of the machine is considered as a part of follow-up 2nd generation work as well.

The torque production test allows indirect estimation of saliency and L_q under load conditions. Considering constant L_d across variable current angle due to operation in MTPA under negative i_d, L_q for given i_q may be calculated using Equ. 4.24. FEA predicted at 1pu i_d current that $L_{q,FEA} = 246\,\mu H$ unlike indirect estimation from test results shows $L_{q,m} = 227\,\mu H$.

Analogically the model predicts saliency $L_d - L_q$ for 1pu i_d current at $-86\,\mu H$ unlike test results estimated the same parameter at $-67\,\mu H$.

7.7. Measurement of Efficiency

Probably the most critical measurement from hybrid drive stand point of view is focused on validation of efficiency models. The actual efficiency measurement was in fact part of heat runs, when once temperature of the winding settled down for a particular torque load and speed, efficiency was measured across that given speed. The measurement was performed for generating mode of operation. Actual post-processing of testing was directly performed throughout digital power analyzer. Results of efficiency measurement summarize Tab. 7-5 below.

Tab. 7-5 Comparison of predicted and measured MG2 efficiency

Speed (rpm)	***700***		*Winding temperature (degC)*			*110.7*	
Input Torque (Nm)	-215.379	-355.222	-498.087	-631.2	-767.583	-967.743	
η,predicted (%)	95.35	95.76	95.44	94.92	94.32	93.33	
η,measured (%)	91.14	92.88	92.82	92.32	91.62	90.42	
Error (%)	-4.62	-3.10	-2.82	-2.82	-2.95	-3.22	
Speed (rpm)	***1300***		*Winding temperature (degC)*			*115.4*	
Input Torque (Nm)	-86.998	-309.802	-458.077	-605.176	-751.294	-1008.257	-1106.099
η,predicted (%)	84.96	94.81	95.59	95.73	95.62	95.19	94.96
η,measured (%)	83.85	93.92	94.62	94.37	94.14	92.91	89.42
Error (%)	-1.32	-0.95	-1.03	-1.44	-1.57	-2.45	-6.20
Speed (rpm)	***2000***		*Winding temperature (degC)*			*93.4*	
Input Torque (Nm)	-220.001	-317.988	-415.196	-511.968	-607.871	-703.01	-892.22
η,predicted (%)	91.93	93.97	94.99	95.57	95.85	96.03	96.13
η,measured (%)	90.63	92.84	93.92	94.46	94.66	94.73	94.67
Error (%)	-1.43	-1.22	-1.14	-1.18	-1.26	-1.37	-1.54
Speed (rpm)	***2800***		*Winding temperature (degC)*			*113.75*	
Input Torque (Nm)	-81.437	-150.874	-287.954	-355.781	-422.999	-490.429	-625.58
η,predicted (%)	79.73	85.31	91.87	93.15	94.08	94.58	95.31
η,measured (%)	69.11	83.60	90.12	91.40	92.45	92.80	93.19
Error (%)	-15.36	-2.05	-1.94	-1.91	-1.76	-1.92	-2.28

The input torque was varied across four fixed reference speed at 700, 1300, 2000 and 2800rpms allowing consistent map up of efficiency across wide speed range. The maximum available torque was limited by capabilities of power electronics, as it was described in introduction to this chapter.

The summary of this measurement flags up a load points with significant error in between test result versus analytical prediction. The measurement case of 2800rpms, -81.437Nm suffered by lack of the split of no-load losses. Since the no-load losses hit their peak at maximum speed, the error in their estimation projected at low input torque case even in a greater manner.

7.8. Heat Runs on MG2

The main objective of this test is to discover steady-state temperature rise of the winding for nominal torque within speed range up to 1300rpms and at nominal power above the base speed. The test results are compared to the prediction using the transient 3D thermal model so that the thermal model considers as an input parameter the exactly same coolant temperature as occurred during the actual testing. The layout of the cooling loop as it stands in the moment does not allow transient testing, since the coolant temperature is not stabilized throughout a test. Thus, only steady-state temperature readings are relevant.

Tab. 7-6 below summarizes load points under testing, including measured and predicted temperature rise of the winding.

Tab. 7-6 Predicted and measured temperature rise at selected loadpoints of MG2

Speed (rpm)	***700***	***1300***	***2000***	***2800***
Load Torque (Nm)	-772.016	-772.629	-524.508	-359.580
Coolant Inlet Temp. (degC)	49.1	50.3	52.0	62.3
R at Coolant temp. (mΩ)	10.648	10.694	10.760	11.159
Temp. rise,measured (degC)	61.628	65.075	41.434	51.450
Temp. rise,predicted (degC)	57.570	67.431	47.416	50.831
Error (%)	6.585	3.620	14.437	1.203

Error in temperature prediction oscillates from 1.2% up to 14.4% in various load points. Further improvement of the thermal model relies, besides increased fidelity of loss model, also on further CFD work estimating temperature conditions in surrounding components of the hybrid powertrain. Specifically, temperature distribution in the housing, the clutch in between MG1 and MG2 alongside with the transmission clutch, need to be understood. These components may impact actual temperature of the machine throughout heat conduction.

8. Future Improvements

Since the main objective first design iteration of MG2 was mainly a proof concept study, it is necessary to revisit achievements and lessons learned out of the prototype of the machine. This chapter will try finding answers on which expectations the first prototype iteration met, and will aim to identify areas for improvement, thus driving requirements for the next generation of design.

8.1. Objectives for Next Design Iteration

By reviewing design requirements shown in Tab. 2-2 with values of parameters predicted in analytical design stage in Tab. 4-11 and test results presented in Chapter 7., one may drawn out following summary. The main achievements are:

- Successful proof of concept of MG2 topology
- Meeting packaging limitation, except of short deviation in terms of actual axial length of the machine
- Feasibility for traction drive due to ability to operate in field weakening
- Fulfilling specification by means of torque and power requirements, with slight discrepancy on no-load losses side reducing overall torque output
- Meeting demanded EMF, which has been lowered by additional manufacturing impacts

MG2 as a prototype build met expectations in terms of performance, with exception of slight discrepancies in prediction of no-load losses. Unfortunately, these drops in performance were caused by design adjustments initiated by manufacturing side, and happened after design freeze for the prototype. Though these factors reduced overall torque throughput, they were identified and described. Thus, proper counter-action might be taken in next design iteration in order to fully meet specification from performance stand point of view.

Some of the drawbacks of the prototype machine started popping-up and appearing clearer as the machine design, manufacturing of its components and assembly was progressing ahead. Most of them are related to actual manufacturing and assembly process, as might be understood from the following summary:

- “Open circuit” character of the rotor core, causing attraction of ferromagnetic objects to the back side of rotor plates
- Thus physical clearance behind each rotor plate is required
- High inertia of the rotor set, partially caused by sensing and outer retaining rings
- Manufacturing of rotor cores, limiting design freedom on the rotor side

- Leakage flux throughout rotor bridges
- Thus relatively lower permanent magnet utilization factor
- Three-phase short circuit current exceeds the peak converter current, thus power electronics would not sustain short circuit event (however, this requirement had risen up once the MG2 design was already frozen).
- Bespoke machining tasks on rotor outer retaining rings, complicating serial production
- Required quantity of rare and expensive construction materials for machine construction, in particular magnet material and stainless steel

As outcome of above-mentioned drawbacks for the first MG prototype iteration, following redesign direction were proposed:

- Easier system integration in terms eliminating safety clearance behind the rotor plate, and reduction of three-phase short circuit current below peak current
- Design for Manufacturing/Assembly reducing bespoke machining tasks and thus, overall time and cost required by manufacturing process
- Reduction of cost, especially throughout lower consumption of expensive rough materials
- Maintaining or enhancing of performance in terms of torque density

Such a definition of redesign objectives requires reinitiating of concept generation phase in terms of seeking for modification of the current design of MG2.

8.2. Proposals for 2nd generation of MG2

Many ideas for design improvements came across during development of MG2 prototype and particularly, during manufacturing and assembly process of the machine. Those ideas crystallized into three different concepts, which are introduced as redesign proposals.

8.2.1. MG2 with casted Aluminum Backplate

As the iterations in between electromagnetic and mechanical design were progressing, it became more apparent that the amount of leakage flux through rotor bridges significantly lowered utilization of permanent magnet material, and thus increased cost of the machine as well. Also, the rotor inertia was considered as a disadvantage for traction motor/generator application. The idea of aluminum backplate aims to reduce both of these negative factors by effectively eliminating the back-side bridge of the rotor plate. The laminated rotor structure would be manufactured free of this bridge, having a locking feature stamped out in the middle of the iron pole between magnet slots. This ensures mechanical coupling in between the laminated rotor core and aluminum backplate. The backplate would be casted in a way so that magnet slots are preserved by inserting dummy magnets since temperature of aluminum in liquid state would exceed Curie temperature of NdFeB material. Fig. 8-1 below introduces actual concept of MG2 with aluminum backplate in circumferential cross-section view.

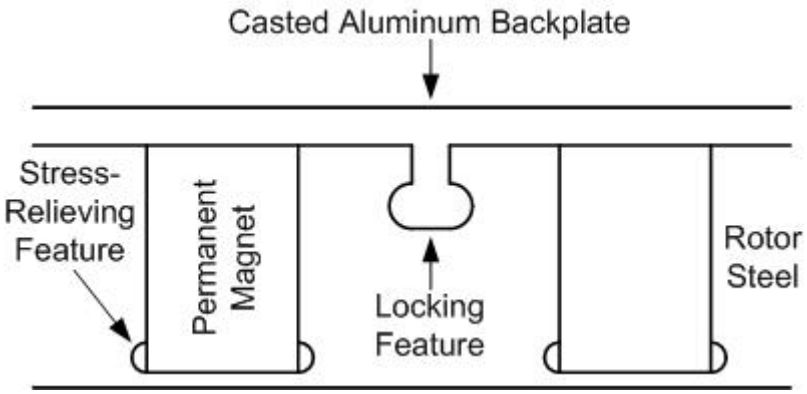

Fig. 8-1 Cross-section through a rotor plate with casted aluminum backplate

A design spreadsheet was derived from the original one for first prototype iteration of MG2. The spreadsheet calculation were calibrated by simplified 2D FEA study aiming mainly to verify the amount of leakage flux through the front rotor bridge, respectively through the aluminum backplate. Fig. 8-2 illustrates contour plot of magnetic vector potential.

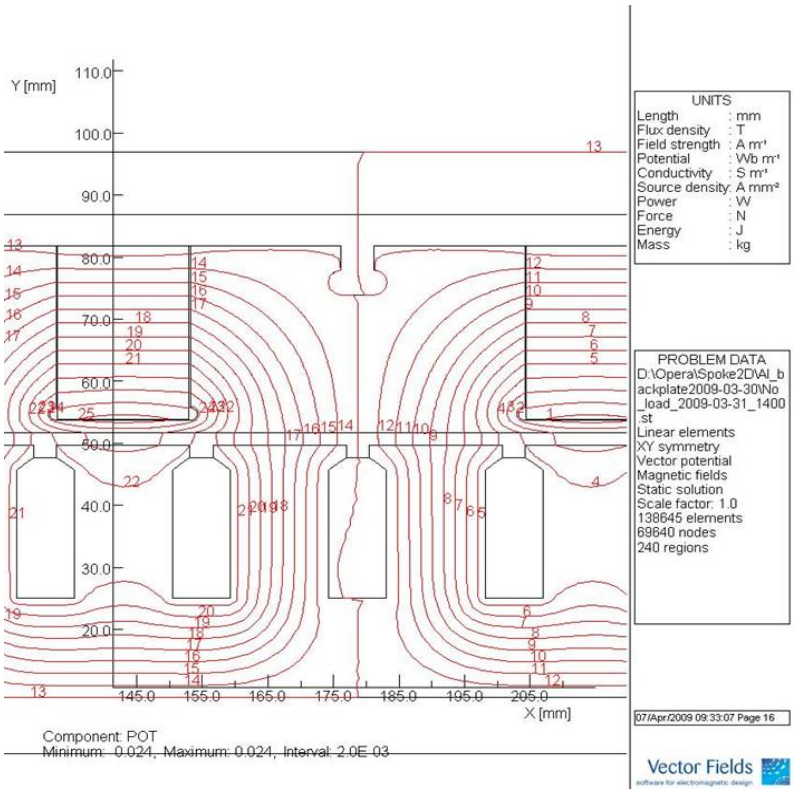

Fig. 8-2 Cross-section through a rotor plate with casted aluminum backplate

The amount of leakage flux dropped down by 45%, which resulted in further analysis focused on structural stability of the concept.

Unfortunately, the concept of casted aluminum backplate does not provide sufficient structural strength to the rotor sub-assembly. Results of FEA have shown, that the laminated structure of the rotor core separates from the inner carrier ring at their joint. This leads toward bending of the aluminum backplate at the area of the joint as shows Fig. 8-3 below.

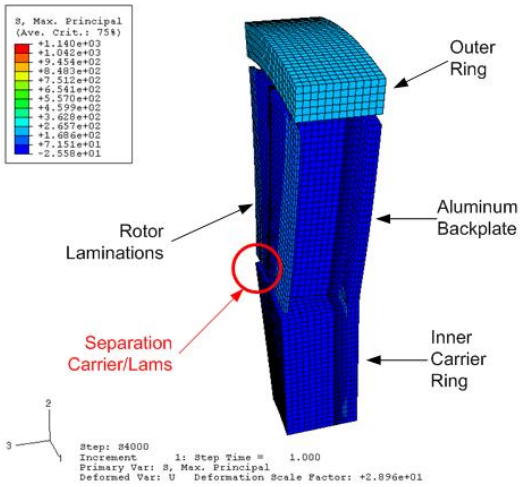

Fig. 8-3 Separation of rotor laminations from the inner ring due to centrifugal forces at overspeed conditions of 4000rpm. This analysis was performed by external resources

Another issue related to this concept is in slotting and winding up of the rotor core. The strip of electric steel would be asymmetrically pre-loaded during the winding process since a bridge is present only at one side of the lamination strip. Thus, there is a risk of tearing the lamination strip apart during process of winding it up on the mandrel.

Considering issues with structural stability of the rotor plate and unanswered questions related to manufacturing of the laminated rotor structure, the idea of MG2 with casted aluminum backplate did not qualify further as next a generation design proposal.

8.2.2. Inner Rotor MG2

Magnetic field of MG2 rotor plate may divert principally into both axial directions. Since the stator core is only in 2mm distance from the rotor once the machine is assembled, only marginal stray flux closes through the air behind the rotor plate. Once a ferromagnetic object is attached in sufficiently close distance to the rotor core, magnetic field divers there because of low reluctance fluxpath. This is the main idea behind inner-rotor MG2 topology, made of two separate stator cores with sunflower winding and one rotor plate in the exactly same electromagnetic configuration, as for the double rotor MG2, located in between them. Fig. 8-4 illustrates cross sectional view through the middle of the rotor plate and similar view through entire machine.

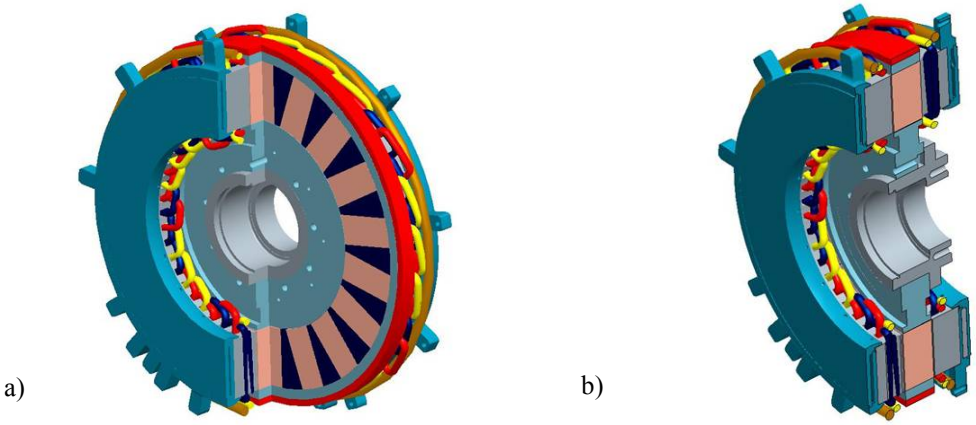

Fig. 8-4 Cross sectional view through inner-rotor MG 2 topology

An advantage of such arrangement is in considerable reduction of leakage flux, simply because of presence of only two bridges holding magnets instead of four bridges in a case of double-rotor topology. Therefore, MG2 inner rotor topology benefits from 19% saving of magnet mass required for 100/200kW power rating. A distribution of magnetic fields in no-load condition depicts Fig. 8-5 below.

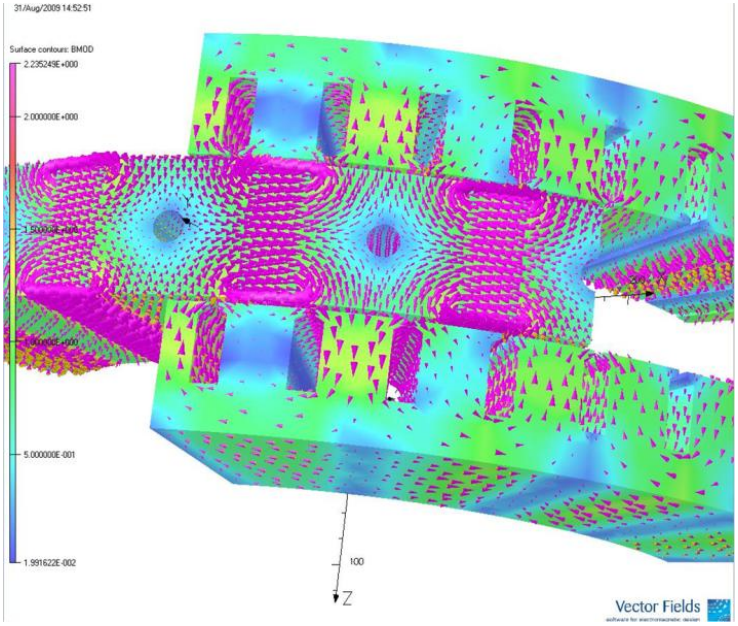

Fig. 8-5 Distribution of vectors of magnetic flux density in no-load state

Further benefits of this topology arise from winding layout, specifically sunflower, double-layer winding providing inherently higher inductances due to increased mutual coupling in between phases. On the other side, sunflower winding introduces complications in terms of winding manufacturing process.

From mechanical design stand point of view, also rotor inertia tends to be lower due to above mentioned savings on rotor bridges and thus, permanent magnet material. Moreover, the rotor is not faced, if well-centered, to unbalanced axial forces.

However, this topology makes the cooling arrangement more complicated due to the need for two separate cooling jackets, one for each stator core.

8.2.3. Tapered-Magnet MG2

The concept of tapered-magnet MG2 aims to radically alter the manufacturing approach, and thus design, of the machine. Instead of having the rotor core made of continuously-wound strip of slotted laminations, the rotor iron pole located in between magnets is composed out of electrical steel patches of constant cross-section cascaded from inner up to outer diameter of the rotor. Therefore, the rotor bridges are in principle eliminated. Magnets are of a tapered shape, fitting into slots created by stack up of lamination patches. A small lip, instead of a whole bridge, locates magnet axially in the rotor structure. The rotor composition out of permanent magnets and columns of steel patches is mechanically strengthened by a backplate machined out of aluminum with tapers locking columns of steel patches in their position. The entire rotor structure is secured against centrifugal forces by the outer stainless steel retaining ring.

The layout of tapered-magnet MG2 in terms cross-sectional view throughout the machine and through a rotor structure, is depicted on Fig. 8-6.

a) b)

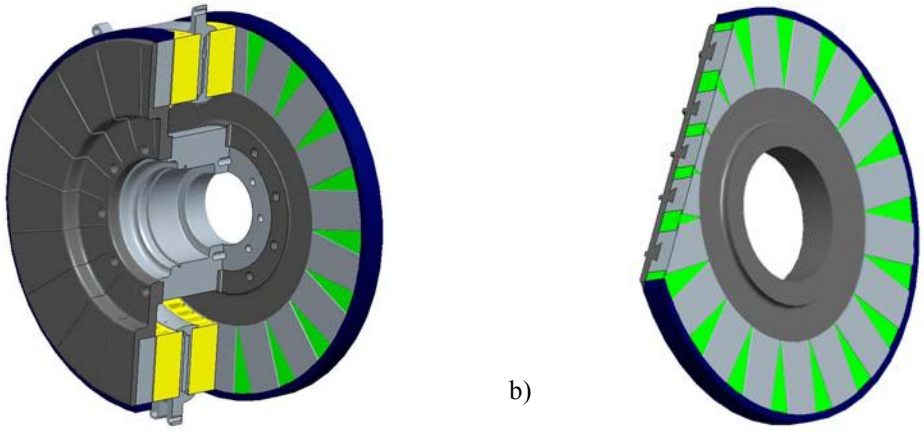

Fig. 8-6 Cross sectional views of Tapered-Magnet MG2 with emphasis on the rotor structure

Finite-element analysis was performed in order to calibrate the electromagnetic design. The equivalent reluctance circuit is on the rotor side divided into radial segments in order to capture tapered shape of permanent magnets, having variable Ampere-turns based on diameter. Although this topology leads in principle toward reduction of the leakage flux within the rotor, the overall magnet mass increased by 10% for 100/200kW rating of the machine due to the tapered shape of the magnet. This resulted into poor utilization of magnet Ampere-turns at inner- and outer- diameter. Following Fig. 8-7 illustrates distribution of magnetic flux lines within tapered-magnet MG2 in no-load operational condition at the mean diameter of the machine.

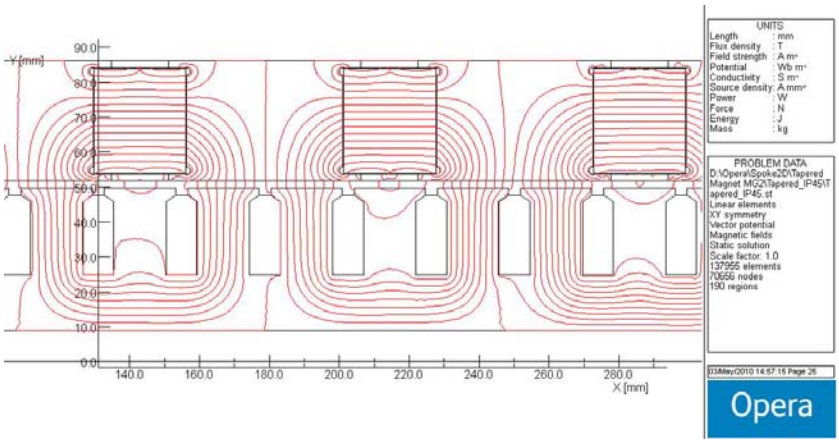

Fig. 8-7 Distribution of magnetic field in Tapered-Magnet MG2

The stator design in fact corresponds to the first generation of MG2.

Furthermore, the concept of tapered-magnet MG2 would allow in terms of machine topology single rotor, twin stator layout, similar to inner-rotor MG2, concerning its magnetic field distribution.

8.3. Benchmarking of Options for MG2 Redesign

Since proposal of MG2 with casted backplate was scrapped for principal issues related to its mechanical design, Inner Rotor MG2 and Tapered-magnet MG2 were nominated for actual benchmarking with first design iteration of MG2. Actual comparison is carried out based on cost and performance basis.

8.3.1. Comparison on Cost Basis

Assessment of cost for considered concepts of MG2 focuses only on material cost, since overhead, profit margin and non-refundable engineering cost would be approximately the same for all topologies. Hence, the cost comparison considers principally material cost and initial estimate on man-hours required for manufacturing of parts and machine assembly. Actual cost is divided into four classes – permanent magnets, rotor subassembly (excluding magnets), stator subassembly and miscallaneous&hardware. First generation of MG2 is considered as a benchmark at level of 100% for each of those categories. The actual cost comparison illustrates in terms of bar chart Fig. 8-8.

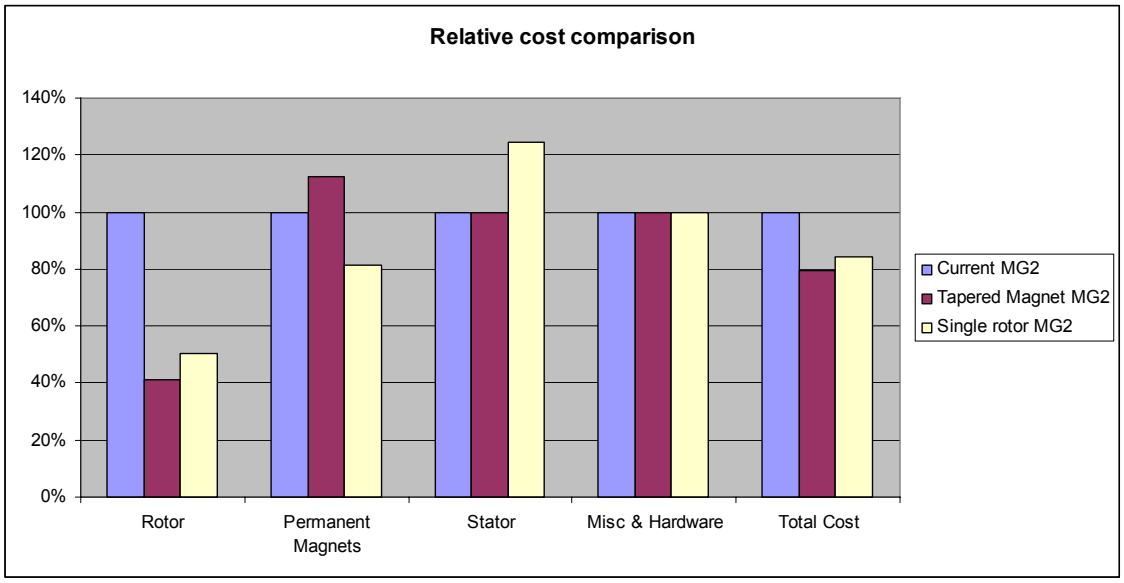

Fig. 8-8 Relative cost comparison between MG2 topologies

Both redesign proposals benefit from the simplified rotor construction. However, the tapered-magnet MG2 suffers from additional magnet mass, unlike single rotor topology from requirement for two separate cooling jackets and higher copper mass due to the sunflower stator winding with greater consumption of a wire for endwindigs.

As a outcome of cost comparison, and with consideration of accuracy of this costing exercise, potential savings due to introduction of redesigns, may reach up to 20% against a benchmark given by MG2 1st generation.

8.3.2. Comparison on Design and Performance Basis

Both redesign proposals, which qualified for the final comparison, were sized to meet the specification of 1st generation of MG2 in terms of performance.

Concerning MG2 envelope, the inner rotor topology suffers from more complicated sunflower winding arrangement. It requires extra 20mm in terms of diameter, whilst actual corepack outer diameter remains the same. However, the inner rotor topology benefits from reduced axial length on the rotor side.

It is expected to save up to 20% of MG2 weight mainly due to the rotor redesign, which furthermore results in drop of rotor inertia, as shows Tab. 8-1.

Tab. 8-1 Comparison in between MG2 topologies concerning design and performance

	Current MG2	Inner Rotor MG2	Tapered Mag. MG2
Change in OD (mm)	Datum	+20	0
Change in Axial Length (mm)	Datum	-16.4	+16.6
Mass (kg)	228	192	194
Rotor Inertia (kg.m2)	5.25	3.54	3.43
13,SC (p.u.)	2.86	1.67	2.09

The last selected criterion is three-phase short circuit current $I_{3,SC}$, which must fit below 2 per-unit current limit, or in other words, the maximum converter current. The inner rotor topology meets the target by reaching $I_{3,SC} = 1.67\,pu$ due to relatively higher d-axis inductance.

Decision, whether any of proposed concepts should be selected for the follow up generation of MG2, is mainly driven by customer needs and the business strategy of the corporation.

9. Conclusion

The Spoke Axial Flux Motor-Generator represents a novel electrical machine designed for a specific application of a traction drive as a component of hybrid electric powertrain. The actual design combines several features, which led toward intellectual protection of this machine.

The MG2 design followed the "Multiphysics" approach combining electromagnetic, thermal, mechanical, and controls design in a closed iterative loop. This ensured balance in between electromagnetic performance, cooling, static and dynamic structural stability and controllability of the machine. Analytical calculations were extensively supported by FEA and CFD in order to obtain a higher degree of confidence in actual design. Since modeling of the motor-generator included also three-phase inverter supplying the machine, overall functionality, efficiency and performance of the electric drive as a subsystem of hybrid electric vehicle, it was well understood prior the testing of the unit. Hence, the system analysis group was able to work on further optimization of the hybrid powertrain with a sufficient level of fidelity even prior actual assembly of the hybrid drive in a test cell.

The actual topology adopted from the electromagnetic stand point of view flux-focusing technique is able to achieve high magnetic loading in the airgap. Meanwhile, the magnet arrangement features inverse-saliency as a preferred option for traction motor drives with Synchronous Permanent Magnet Machines. Once the machine enters field weakening in constant output power mode, the negative d-axis current, required for suppressing of the base harmonic of EMF, helps to produce extra reluctance torque enhancing performance of the machine.

The thermal design in fact enabled operation of the machine under specified electromagnetic loading. Adopted water/glycol cooling through aluminum heat sink sandwiched in between stator cores allowed the machine to operate with relatively low thermal gradient from winding side to the coolant circulating in the cooling jacket. The analytical tool developed for thermal design and analysis predicted temperature of the winding even in transient mode at various load points, coolant flow rate and inlet temperature.

The control design dealt with assessment of different control strategies feasible for the discussed machine topology. In particular, the optimization potential in terms of drive efficiency is assessed. Understanding of efficiency is a critical element in the design of a hybrid drive, thus a set of simulation tools have been developed for that reason.

The manufacturing and assembly of MG2 introduced revolutionary design of axial-flux permanent magnet machines by adopting strip-wound structure embedding permanent magnets in the rotor core. This concept has proven itself to be functional though it was faced with many difficulties to during the development phase of the machine. However, the manufacturing and assembly process in the first design iteration of the machine is not straightforward enough for lean manufacturing approach. The

rotor design might be optimized further due to knowledge gained from the first prototype built. Therefore, a set of follow-up design concepts has been proposed.

Several prototypes of Spoke-MG2 have been built in order to pass through extensive testing. It has been shown that the machine met performance target as predicted in the design stage, especially in terms of actual parameters in dq0 reference frame, torque production, efficiency and winding temperature rise at various load conditions. Only considerable discrepancy is in prediction of no-load losses, mainly due to difficulties in understanding of bearing loading and properties of electrical steel, which was applied in unusual conditions.

This thesis summarizes the thought process leading toward selection of a concept, design and analysis, followed by manufacturing and testing of a unique Axial-Flux Synchronous Permanent Magnet Machine. This design is remarkable because it has pushed forward boundaries in terms of actual machine topology and its construction, it has achieved torque density, targeted actual power rating and provided a downsized envelope. Moreover, integrated design and analysis package was developed, which may be applied for its generic nature to another machine design projects as well.

The design of Spoke-Axial Flux Machine is a part of hybrid powertrain initiative as one of the major research and development programs within Cummins Inc., and Cummins Generator Technologies as a producer of electrical machines with hundred-year tradition.

Literature

[1] Available at: http://www.fueleconomy.gov/feg/climate.shtml

[2] Clean Cities Annual Metrics Report 2007. Available at http://www.nrel.gov/docs/fy07osti/41753.pdf

[3] COOK, A. The Road to Electrification for Specialty Vehicles, Proceedings of 2008 IEEE International Conference on Vehicular Electronics and Safety, Columbus, OH, Sept. 2008

[4] NELSON, C. Exhaust Energy Recovery: 2008 Semi-Mega Merit Review, U.S. Department of Energy, 2008. Available at: www1.eere.energy.gov/vehiclesandfuels/pdfs/merit_review_2008/high-eff_clean_combustion/merit08_nelson.pdf

[5] MTHOMBENI, L. at all. Lamination Core Loss Measurements in Machines Operating with PWM or Non-sinusoidal Excitation. IEEE IEMDC proceedings, June 2003, ISBN 0-7803-7817-2

[6] BAYERER, R. Higher Junction Temp in power modules – a demand from hybrid cars, a potential for the next step increase of power density for various variable speed drives. Proceedings of PCIM EUROPE ‘08, June 2008, ISBN 978-3-89838-605-0

[7] MANABU, Y. at all. New chip design technology for next generation module. Proceedings of PCIM EUROPE ‘08, June 2008, ISBN 978-3-89838-605-0

[8] ROUSSEL. P. at all. SiC Power Devices Market and Forecast. Proceedings of PCIM EUROPE ‘08, June 2008, ISBN 978-3-89838-605-0

[9] RUPP, R. Application Opportunities of SiC devices. Proceedings of PCIM EUROPE ‘08, June 2008, ISBN 978-3-89838-605-0

[10] YANG, L. The marvelous development of the rare earth magnet industry, UK Magnetic Society, Magnews Winter 2008

[11] KAWANO, M. at all. Electrical Steel for High-functional Automotive Electrical Components Corresponding to Energy Saving. Kawasaki Steel Giho, vol. 34, 2002

[12] YABUMOTO, M. at all. Electrical Steel Sheet for Traction Motors of Hybrid/Electric Vehicles. Nippon Steel Technical Report No. 87, July 2003

[13] MUNEHIRO, K. Development of Traction Drive Motors for the Toyota Hybrid System. Transactions of the institute of electrical engineers of Japan, vol. 126, no. 4., 2006, ISSN 0913-6339

[14] HEIKKILA, T. Permanent Magnet Synchronous Motor for Industrial Inverter Applications-Analysis and Design. Thesis for the degree of Doctor of Science, Lappeenranta Univ. of Technology, 2002

[15] UQM – Vehicle Propulsion Systems Datasheets, April 2008 Available at: http://www.uqm.com/propulsion_specs.php

[16] RODEWALD W at all. Top Nd-Fe-B Magnets: >56 MGOe, Energy Density, 9.8 kOe Coercitivity. Intermag 2002, Amsterdam, April 2002

[17] OLSZEWSKI, M. Evaluation of 2005 Honda Accord Hybrid Electric Drive System. Prepared by the OAK RIDGE NATIONAL LABORATORY for the U.S. Dept. of Energy Available at: www.osti.gov/bridge/servlets/purl/921774-SGWLl5/

[18] MILLER T. J. E. *Brushless Permanent-Magnet and Reluctance Motor Drives*. Oxford: Clanderon Press 1989. 202 pages. ISBN 0-19-85-9369-4.

[19] GM-Allison Hybrid EP50 System, April 2009, Available at: http://www.allisontransmission.com /servlet/DownloadFile?Dir=publications/pubs&FileToGet=SA3577EN.pdf

[20] BROWN. N. L. STEAM-A Smart Electrical Machine for Integrated Engine Application. *Electromagnetics in Power System Applications*. UK Magnetic Society, Wantage, Ox., June 2008.

[21] Remy Hybrid Technology and You, April 2008, Available at: http://www.remyinc.com/hybrid/hybrid.htm

[22] KAORU, A. Development of Integrated Motor Assist Hybrid System: Development of the 'Insight', a Personal Hybrid Coupe, SAE Gov./Industry meeting 2000, Washington D.C. ISSN 0148-7191

[23] BAUER, M. ELFA-Innovative Series Hybrid Drives for Single Unit and Articulated City Buses. Available at: www.siemens.com/elfa.

[24] ODVÁŘKA, E. at all. Electric Motor-Generator for a Hybrid Electric Vehicle. *Engineering Mechanics*. 2009, vol. 16, no. 2, 1-9. ISSN 1802-1484.

[25] STAUNTON, R. H. at all. PM Motor Parametric Design Analyses for a Hybrid Electric Vehicle Traction Drive Application. Prepared by the OAK RIDGE NATIONAL LABORATORY for the U.S. Dept. of Energy Available at: www.ornl.gov/~webworks/cppr/y2001/rpt/121559.pdf

[26] MILLER, T. J. E. *Electronic Control of Switched Reluctance Machines*. Oxford: Newnes. 288 pages. ISBN 978-0750650731

[27] QIANFAN, Z. Hybrid Switched Reluctance Motor Applied in Electric Vehicle, Proceedings of IEEE VPPC '07 conference, Sept. 2007,

[28] KRISHNAN, R. Theory and Operation of a Four-Quadrant Switched Reluctance Motor Drive With a Single Controllable Switch – The Lowest Cost Four-Quadrant Brushless Motor Drive. IEEE Transactions on Industry Applications, Vol. 41, No. 4, Jul./Aug. 2005

[29] BUMBY, J. at all. Electromagnetic Design of Axial-Flux Permanent Magnet Machines. IEE proceedings on Electric Power Applications, vol. 151, Issue 2, pages 151-160, Mar. 2004

[30] GIERAS, J. F. *Axial Flux Permanent Magnet Brushless Machines*. Dordrecht: Kluwer Academic Publishers, 2004, 340 pages, ISBN 1-4020-2661-7.

[31] HUANG, S., AYDIN, M., Lipo, T. Comparison of (Non-Slotted and Slotted) Surface Mounted PM Motors and Axial Flux Motors for Submarine Ship Drive, Available at: www.ece.wisc.edu/~lipo/2000pub/00-33.pdf

[32] YANG, Y. P. Optimal design and control of Axial-Flux Brushless DC Wheel Motor for Electrical Vehicles. Proceedings of MED'02, Lisbon, July 2002

[33] GONZALES-LOPEZ, D. A. Design and Test of an Axial Flux Permanent-Magnet Machine With Field Control Capability. IEEE Transactions on Magnetics, 2008, Vol. 44, no 9,

[34] AYDIN, M. at all. A New Axial Flux Surface Mounted Permanent Magnet Machine Capable of Field Control. Proceedings of Industry application Conference 2002, ISBN 0-7803-7420-7

[35] SOONG, W. L. Field-Weakening Performance of Interior Permanent Magnet Motors. Industry Application Conference 2000, vol. 1, ISBN 0-7803-6401-5

[36] ROJAS, A. at all. Axial Flux PM Machine Design with Optimum Magnet Shape for Constant Power Region Capability. Proceedings of ICEM '08, Sept. 2008, ISBN 978-1-4244-1736-0

[37] VIDO, L. at all. Compared Performances of Homopolar and Bipolar Hybrid Excitation Synchronous Machines. IEEE IAS annual meeting Hong- Kong, Oct. 2005

[38] BROWN, N. L. New Brushless Synchronous Alternator. IEE Proceedings Electrical Power Applications, Vol 150, No. 6, Nov. 2003

[39] MORIMOTO, S. at all. Loss Minimization Control of Permanent Magnet Synchronous Motor Drives. IEEE transact. on industrial electronics, vol. 41, no. 5, Oct. 2004

[40] MADEMLIS, C. Optimal Efficiency Control Strategy for Interior Permanent Magnet Synchronous Motor Drives. IEEE transactions on energy conversion, vol. 19, Dec. 2004, ISSN 0885-8969

[41] BOSE, B. K. *Modern Power Electronics and AC Drives*. Upper Saddle River: Patience Hall PTR, 2002. 711 pages. ISBN 0-13-016743-6.

[42] SUH, Y. at all. Unity Power Factor Control of a Three-pole PWM AC/DC Converter under single-phase Input. Available at: www.ece.wisc.edu/~lipo/2001pubs/2001_03.pdf

[43] WALLMARK, O. Control of Permanent-Magnet Synchronous Machines in Automotive Applications. Thesis for the Degree of Doctor of Philosophy, Chalmers Univ. of Technology, 2006

[44] SUE, S.-M. at all. Voltage-Constraint-Tracking Based Field-Weakening Control of IPM Synchronous Motor Drives. IEE transactions on industrial Electronics, vol. 55, no.1, Jan. 2008

[45] LUKIC, S. M., EMADO, A. Modeling of electric machines for automotive applications using efficiency maps. IEEE Electrical Insulation Conference Proceedings, pp. 543-550, Sept. 2003

[46] BELICOVA, E., HRABOVCOVA V. Analysis of an Axial Flux Permanent Magnet Machine (AFPM) based on Coupling of two Separated Simulation Models (Electrical and Thermal Ones). *Journal of Electrical Engineering*. 2007, vol. 58, no. 1, 3-9. ISSN 1335-3632

[47] HENDERSHOT, J. R., MILLER, T. J. E. *Design of Brushless Permanent-Magnet Motors*. Oxford University Press, 1995. ISBN 0198593899.

[48] OLSZEWSKI, M. Freedomcar Advanced Traction Drive Motor Development, Phase I. Sep. 2006, Submitted by Oak Ridge National Laboratory for US Department of Energy.

[49] HUANG, S., AYDIN M, LIPO, T. A. TORUS Concept Machines: Pre-Prototyping Design Assessment for Two Major Topologies. *IEEE Industry Applications Society Annual Meeting*. Sep.30-Oct.4, 2001, Chicago, 1619-1625.

[50] CAMPBELL, P. Performance of a Permanent Magnet Axial-Field DC Machine. *IEE Proceedings – Electrical Power Applications*. 1979, vol. 151, no. 2, 139-144.

[51] KAZMIERKOWSKI, M. P., TUNIA, H. *Automatic Control of Converter-Fed Drives*. Elsevier, Amsterdam, 1994. ISBN 0-444-41713-3.

[52] SALON, S. J. *Finite Element Analysis of Electrical Machines*. Kluwer Academic Publisher, Den Haag, 1995.

[53] LIENHARD, J. H. *A Heat Transfer Textbook, 3rd edition*. Phlogiston Press, Cambridge, MA, 2008, 749 pages. ISBN-13 978-0971383531

[54] BOGLIETTI, A. et al. Evolution and Modern Approaches for Thermal Analysis of Electrical Machines. *IEEE Transactions on Industrial Electronics*. March 2009, vol. 56, no. 8

[55] SAHIN, F. *Design and development of a high speed axial flux permanent magnet machine*. Technische Universiteit Eindhoven, 2001, 241 pages. ISBN 90-386-1380-1

[56] HAVA, A. M., KERKMAN, R.J., LIPO, T. A. A High Performance Generalized Discontinuous PWM Algorithm. *IEEE Transactions on Industrial Applications*. 1998, vol. 34, no. 5, 1059-1071.

[57] WALLMARK, O. *On Control of Permanent Magnet Synchronous Motors in Hybrid Electric Vehicle Application. Thesis for the Degree of Licentiate in Engineering*. Chalmers University of Technology Goteborg, Sweden, 2004. 127 pages. ISSN 1651-4998.

[58] BIANCHI, N., BOLOGNIANI, S. Magnetic Models of Saturated Interior Permanent Magnet Motors Based on Finite Element Analysis. *Industry Applications Conference*. Oct 1998, vol. 1.

List of Symbols and Abbreviations

Symbols

A – linear current density

$\boldsymbol{A}$ – magnetic vector potential

A_{th} – heat dissipation area

B_g – airgap flux density

$B_{g,pk}$ – peak airgap flux density

B_σ – magnetic flux density in a bridge

B_r – remanent flux density

B_{MOD} – magnitude of flux density

B_S – flux density in stator yoke

B_T – flux density in stator tooth

B_n – normal component of flux density

B_t – tangential component of flux density

B_x – x-component of flux density

B_y – y-component of flux density

B_z – z-component of flux density

C – capacitance

C_m – magnitude of *m-th* harmonic

C_{th} – thermal capacity

D – duty cycle

D_m – mean diameter of the stator

E – induced voltage

$\boldsymbol{E}$ – electric field

E_{peak} – peak value of induced voltage

E_{max} – transistor peak switching energy

F – force

F_{PM} – magneto motive force of a permanent magnet

F_r – radial force

F_z – axial force

H_c – coercitive force

H_t – intensity of magnetic field

I_{3SC} – three-phase short circuit current

I_d – d-axis current

I_{d0} – d-axis current – the torque production and field weakening component

I_{dc} – d-axis current – the remagnetizing component

I_q – q-axis current

I_{q0} – q-axis current – the torque production component

I_{qc} – q-axis current – the remagnetizing component

I – RMS current

I_{av} – average current

I_{nom} – nominal RMS current

J – current density

L – inductance

L_d – d-axis inductance

L_q – q-axis inductance

$L_{q,FEA}$ – predicted q-axis inductance by FEA

$L_{q,m}$ – measured q-axis inductance

M – momentum

M_i – modulation index

$N_{ph,s}$ – number of stator winding turns in series

Nu – Nusselt number

P_{Cu} – copper loss

P_{Fe} – iron loss

P_{Hs} – power loss in the heat sink

P_{MB} – power loss in the main bearing

P_{PM} – power loss in permanent magnets

P_{RR} – power loss in the retaining ring

P_{UC} – uncontrollable power loss

P_{loss} – power loss

$P_{loss,EM}$ – power loss of electric machine

$P_{loss,h}$ – power loss per stator half segment

P_{nom} – nominal power

P_w – windage power loss

Pr – Prandtl number

Q_p – number of slots per pole

R_a – winding resistance

$R_{a,m}$ – measured winding resistance

$R_{a,p}$ – predicted winding resistance

$R_{a,p,corr}$ – predicted winding resistance after correction

R_c – core loss resistor

Re – Reynolds number

R_{ed} – eddy current loss resistor

R_h – hysteresis loss resistor

R_t – stator tooth reluctance

R_{th} – thermal resistance

R_σ – bridge reluctance

S_c – heat rejection surface

S_{rp} – surface area of a rotor plate

$S_{r,\vartheta}$ – incremental area on a surface of a rotor plate

T – period of a signal

T_{Al} – surface temperature of the cooling jacket

T_{av} – average coolant temperature

T_{cog} – cogging torque

$\vec{T}_{dq0}^{-1}$ - inverse- Park transformation matrix

T_{em} – electromagnetic torque

$T_{e,r}$ – torque ripple

T_{in} – coolant inlet temperature

T_{out} – coolant outlet temperature

T_w – winding temperature

$T_{w,max}$ – maximum winding temperature

V_d – d-axis voltage

V_{DC} – DC bus voltage

V_{nom} – nominal RMS voltage

V_{pk} – peak voltage

$V_{pk,max}$ – maximum available voltage

V_q – q-axis voltage

V_t – transistor threshold voltage

W_m – magnetic energy

W_{off} – dissipated energy during turning-off process

W_{on} – dissipated energy during turning-on process

W_{sw} – switching energy

X_d – d-axis reactance

X_q – q-axis voltage

b_{th} – axial thickness of a bridge

c_0 – DC component of a harmonic signal

c_m – coefficienct of *m-th* harmonic

c_{th} – specific thermal capacity

f_r - remagnetizing frequency

$f_{r,base}$- base remagnetizing frequency

f_s – stator frequency

f_{sw} – switching frequency

g' – physical airgap corrected by Carter's coefficient

g'' – effective airgap

g_a – airgap clearance in axial direction

g_d'' – effective airgap in d-axis

g_q'' – effective airgap in q-axis

g_z – airgap thickness in axial direction

g_{th} – thermal conductivity

h – heat transfer coefficient

i_d – instantaneous d-axis current

i^*_d – instantaneous reference d-axis current

$i^*_{d,MTPA}$ – instantaneous reference d-axis current for MTPA control strategy

i_{pk} – peak value of current

i_q – instantaneous q-axis current

i^*_q – instantaneous reference q-axis current

$i^*_{q,MTPA}$ – instantaneous reference q-axis current for MTPA control strategy

k – thermal overload factor

k_1 – constant of first harmonic to flat top value of armature flux density

k_{1ad} – ratio between first harmonic to flat top value of armature flux in d-axis

k_{1aq} – ratio between first harmonic to flat top value of armature flux in q-axis

k_d – distribution factor

k_a, k_b, k_c – three phase (abc) variables

$k_{\alpha d}$ – pole arc to pole pitch ratio

$\vec{k}_{abc}$ - vector of variables in abc system

$\vec{k}_{dq0}$ - vector of variables in dq0 system

k_e – coefficient for eddy current loss

k_h – coefficient for hysteresis loss

k_p – pitch factor

k_s – spread factor

k_w – winding factor

l – oriented curve

l_a – axial thickness

l_g – mean circumferential length of the airgap

l_{ga} –axial thickness of the airgap

l_{ft} – length of a fluxline in a stator tooth

l_r - radial thickness

l_t – tangential thickness

m_{Fe} – mass of electrical steel

n_b – base speed

n_{pp} – number of winding parallel paths

p_p – number of polepairs

q – coolant volumetric flow rate

q_m – coolant mass flow rate

q_s – number of slots per pole per phase

r – radius

s – analyzed harmonic signal

s_{sp} – slot span

t_{on} – on-time

t_w – tooth width

y – coil pitch

α – thermal diffusivity

β - current angle

λ – thermal conductivity

μ – dynamic viscosity

μ_0 – permeability of vacuum

μ_{PM} – permeability of permanent magnet materia

μ_r – relative permeability

ρ – mass density

Φ_g – airgap flux

Φ_σ – stray flux throughout a bridge

ϑ_r - rotor angular position

τ – time constant

τ_p – pole span

φ – phase of the *m-th* harmonic component

ω_e – electrical angular speed

$\omega_{m,base}$ – base mechanical angular speed

ψ – flux linkage

ψ_d – d-axis flux linkage

ψ_{PM} – magnet flux linkage

$\psi_{PM,FEA}$ – predicted magnet flux linkage by FEA

$\psi_{PM,m}$ – measured magnet flux linkage

ψ_q – q-axis flux linkage

ΔP_{ed} – eddy current iron loss

ΔP_{iron} – iron loss

ΔP_h – hysteresis iron loss

Abbreviations

AC – alternating current

AFPM – Axial Flux Permanent Magnet

ATF – Automatic Transmission Fluid

BMS – Battery Management System

BP – Base Point

EMF – Electromotive Force

CoFe – Cobalt Iron

CFD – Computation Fluid Dynamics

DC – Direct Current

DFMEA – Design Failure Mode Effect Analysis

DOE – Design of Experiment

DSP – Digital Signal Processor

DVA – Dimensional Variation Analysis

EGR – Exhaust Gas Recirculation

FEA – Finite Element Analysis

ICE – Internal Combustion Engine

ID – Inner Diameter

IGBT – Insulated Gate Bipolar Transistor

I/O – Input/Output

ISG – Integrated Starter Generator

HEV – Hybrid Electric Vehicle

LSHT – Low Speed – High Torque

ME – Maximum Efficiency

MG1 – Motor Generator 1

MG2 – Motor Generator 2

MMF – Magneto-motive Force

MTPA – Maximum Torque-per-Ampere

MPG – Miles- per- Gallon

NdFeB – Neodymium Iron Boron

OD – Outer Diameter

OEM – Original Equipment Manufacturer

PE – Power Electronics

PM – Permanent Magnet

PWM – Pulse Width Modulation

SAE – Society of Automotive Engineers

SiC – Silicon Carbide

SOC – State of Charge

SRM - Switched Reluctance Motor

TA – Torque Assist

TEL – Transient Emission Load

THD – total harmonic distortion

$THD_{,mod}$ – modified total harmonic distortion

TRV – Torque-per-Rotor Volume

VPI – Vacuum Press Impregnation

VSIG – Variable Speed Integrated Generator

WHR – Waste Heat Recovery

p.u. – per unit

List of Appendixes

Appendix A – Layout of MTPA Controller

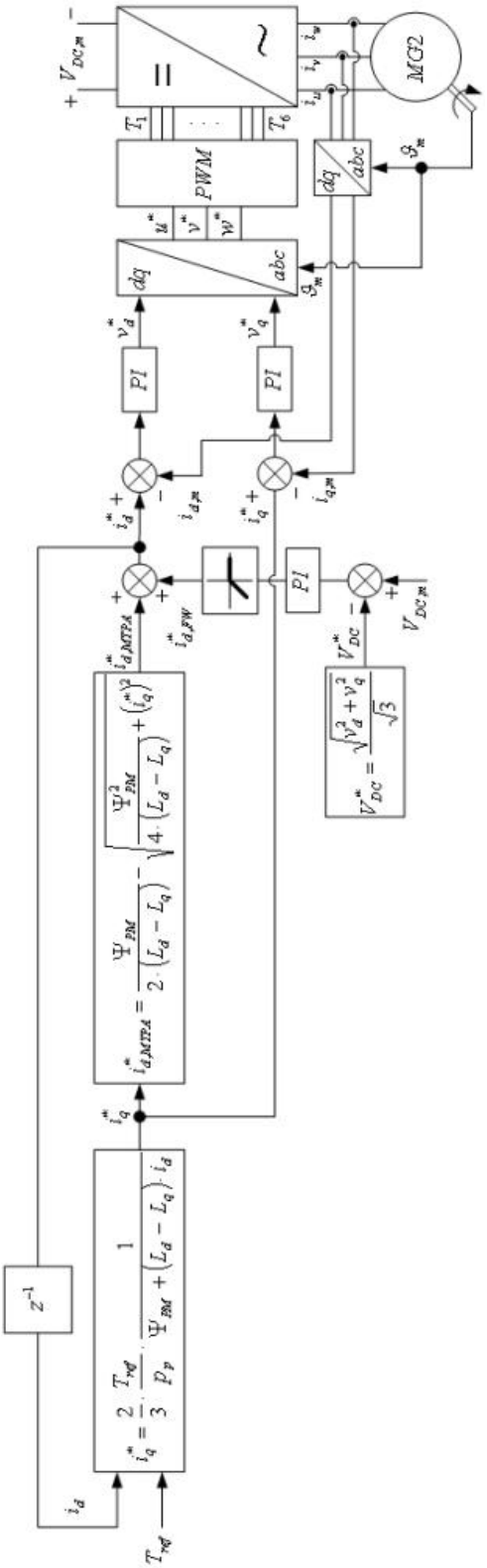

Appendix B - Critical Parameter Tree Impacting Efficiency